# UNDERSTANDING THE BALLISTIC-DIFFUSIVE THERMAL TRANSPORT TRENDS IN CRYSTALLINE SEMICONDUCTORS WITH MOLECULAR DYNAMICS

by

Onurcan Kaya

B.S., Mechanical Engineering, Istanbul Technical University, 2018

Submitted to the Institute for Graduate Studies in
Science and Engineering in partial fulfillment of
the requirements for the degree of
Master of Science

Graduate Program in Mechanical Engineering
Boğaziçi University

2021

# ACKNOWLEDGEMENTS

I would like to express my deepest graditude to Dr. Nazli Donmezer for her profound belief in my work, her guidance and patience, she is the greatest advisor and mentor a student can have. I would also like to express my deepeset appreciation to my committee, for reviewing my work, giving helpful advice, and sharing their constructive criticism.

I grateful to my dear friends Duygu, Ceren, Gülce, İlke, and Enver for their immense support. I would also like to thank my colleagues Taher, Emine, Pegah, Burak, Canberk and Haluk for their insightful suggestions and their support.

I cannot begin to express my thanks to my mom, dad and sister for their endless love and support. Their faith in me and encouragement is unforgettable. Finally, I thank to Bogazici University Research Funding (BAP) Organization, İTÜ National Computing Center (UHeM) and The Scientific and Technological Research Council of Turkey (TÜBİTAK) for their support of our work with grant number 14330, 4006962019, and 119F049. Their funds made this thesis possible.

# ABSTRACT


## UNDERSTANDING THE BALLISTIC-DIFFUSIVE THERMAL TRANSPORT TRENDS IN CRYSTALLINE SEMICONDUCTORS WITH MOLECULAR DYNAMICS

Due to the growing demand of the market, semiconductor device size decreases and power density increases continuously. In today's semiconductor devices, extremely small architecture and localized heating disrupt energy carrier's movements and thermal transport. Consequently, device temperature becomes higher which leads to degraded device performance and lifetime. Hence, thermal transport deviates from the continuum behavior and the thermal conductivity of materials is reduced. A rigorous understanding of size effects is a necessity to build an effective thermal management strategy. Current experimental and theoretical characterization methods need a significant amount of time and effort. Thus, there is a need for simple relations to characterize the size effects and relate them to the existing phonon data. To do that, the trends in ballistic – diffusive thermal transport regime and its effect on thermal transport properties of thin films, interfaces, and localized heating regions are investigated using molecular dynamics simulations. The relations between material and phonon properties and trends in ballistic - diffusive thermal transport regime in semiconductor materials are discovered for three cases. Obtained relations provide a simple alternative to characterize the size effect in thermal transport in semiconductor devices.

# ÖZET

## MOLEKÜLER DİNAMİK İLE KRİSTAL YARIİLETKENLERDE BALLİSTİK - DİFÜZİF ISI TRANSFERİ EĞİLİMLERİNİN ANLAŞILMASI

Pazarın artan talepleriyle nedeniyle yarı iletken aygıtların boyutu küçülmekte ve güç yoğunluğu artmaktadır. Günümüzün yarıiletken aygıtlarında, son derece küçük yapılar ve localize ısınma, enerji taşıyıcılarının hareketlerini ve ısı iletimini bozar. Sonuç olarak, aygıt sıcaklığı yükselir ve bu da aygıtın performansının düşmesine ve kullanım ömrünün azalmasına neden olur. Bu nedenle, ısı transferi sürekli davranıştan sapar ve malzemelerin ısıl iletkenliği azalır. Etkili bir ısıl yönetim stratejisi oluşturmak için balistik – difüzif ısı iletim rejiminin titiz bir biçimde anlaşılması zorunluluktur. Mevcut deneysel ve teorik karakterizasyon yöntemleri önemli miktarda zaman ve çaba gerektirir. Bu nedenle, boyut etkilerini karakterize etmek ve bunları mevcut fonon bilgileriyle ilişkilendiren basit bağıntılara ihtiyaç vardır. Bunu yapmak için, balistik – difüzif ısı iletimi ve onun ince filmlerin, arayüzlerin ve localize ısınma bölgelerinin ısıl özelliklerine olan etkilerindeki eğilimler moleküler dinamik simülasyonları kullanılarak incelenmiştir. Malzeme ve fonon özellikleri ile balistik – difüzif ısı taşınım rejimindeki eğilimler arasındaki bağlantılar da incelenmiştir. Elde edilen ilişkiler, boyut etkilerinin yarıiletken yapılardaki ısıl transerine boyut etkisinin karakterize edilmesi için basit bir alternatif sağlar.

# TABLE OF CONTENTS

ACKNOWLEDGEMENTS . . . . . iii
ABSTRACT . . . . . iv
ÖZET . . . . . v
LIST OF FIGURES . . . . . viii
LIST OF TABLES . . . . . xii
LIST OF SYMBOLS . . . . . xiii
LIST OF ACRONYMS/ABBREVIATIONS . . . . . xiv
1. INTRODUCTION . . . . . 1
1.1. Thermal Transport in Semiconductor Devices . . . . . 1
1.1.1. Phonon Transport . . . . . 1
1.2. Ballistic-Diffusive Thermal Transport . . . . . 4
1.2.1. Thin Films . . . . . 5
1.2.2. Interfaces at 2D Materials . . . . . 6
1.2.3. Localized heating . . . . . 8
1.3. Thermal Characterization of the Ballistic-Diffusive Effects . . . . . 10
1.3.1. Thin Films . . . . . 10
1.3.2. Interfaces with 2D Materials . . . . . 13
1.3.3. Localized Heating . . . . . 15
1.4. Motivation . . . . . 16
1.5. Outline of the Thesis . . . . . 17
2. MOLECULAR DYNAMICS . . . . . 19
2.1. Non – Equilibrium Molecular Dynamics . . . . . 22
2.2. Approach to Equilibrium Molecular Dynamics . . . . . 24
2.3. Phonon Density of States and Phonon Dispersion Calculations via Molecular Dynamics . . . . . 25
3. THIN FILMS . . . . . 28
3.1. Method . . . . . 29
3.2. Results and Discussion . . . . . 32
3.3. Conclusion . . . . . 41

4. INTERFACES WTH 2D MATERIALS . . . . . 43
4.1. Method . . . . . 45
4.2. Results and Discussion . . . . . 48
4.2.1. Thermal Boundary Conductance . . . . . 49
4.2.2. Thermal Conductivity of the Heterostructures . . . . . 56
4.3. Conclusion . . . . . 60
5. LOCALIZED HEATING . . . . . 62
5.1. Method . . . . . 63
5.2. Results and Discussion . . . . . 65
5.3. Conclusion . . . . . 72
6. CONCLUSIONS AND IMPLICATIONS FOR FUTURE RESEARCH . . . . 75
REFERENCES . . . . . 78
APPENDIX A: COPYRIGHT PERMISSIONS . . . . . 97

# LIST OF FIGURES

Figure 1.1. Phonon dispersion relation of the diatomic chain. Patterns of acoustic and transverse optical waves are also presented. . . . . 2

Figure 1.2. Phonon dispersion relation of GaN thin film. . . . . 2

Figure 1.3. First Brillouin zone of HCP structure. . . . . 3

Figure 1.4. Analytical prediction of the Fourier (diffusive) and ballistic components thermal resistivity away from a half-cylinder. . . . . 4

Figure 1.5. Schematic diagram of phonon transport and scattering mechanisms in the thin film. Thermal transport is confined in z-directions. Periodic boundary condition denotes infinitely long thin in x- and y-directions. . . . . 5

Figure 1.6. Thermal conductivity accumulation spectra with respect to phonon MFP for GaN-based on ab-initio calculations at different temperatures. . . . . 6

Figure 1.7. Thermal boundary resistance with respect to contact size. . . . . 7

Figure 1.8. Temperature distribution of the device channel without (a) and with a Cu-filled (b) micro-trench at a power density of 11.57 and 12.61 W/mm. Thermal breakdown in HEMT without a trench (c) and no breakdown with a trench at an applied voltage bias of 200 V. 9

Figure 1.9. Atomistic Green's function model. . . . . 12

Figure 2.1. Temperature distribution obtained from a NEMD simulation. . . . 22

Figure 2.2. NEMD simulations for TBC of Si/BAs heterostructure. . . . . 24

Figure 3.1. Thermal conductivity accumulation spectra for $GaN$. . . . . 28

Figure 3.2. Crystal structure of $GaN$ (a) and $AlN$ (b). . . . . 29

Figure 3.3. NEMD simulation box: the red zone is the heat source, and the blue zone is the heat sink. . . . . 30

Figure 3.4. Accumulation spectra of wurtzite $GaN$ at 300K, 500K, and 800K obtained via ab-initio calculations. Thermal conductivity accumulation for a 240 nm-thick $GaN$ film is marked. . . . . 34

Figure 3.5. Schematics for improved TC-AS model. . . . . 36

Figure 3.6. Accumulation spectra for$GaN$and $AlN$ thin films with respect to the Kn number. . . . . 37

Figure 3.7. Phonon dispersion relations of $AlN$ (a) and $GaN$(b). Red lines show the LA phonon modes of both materials. . . . . 39

Figure 3.8. Comparison of $k_{tf-AS}$ and $k_{tf-MD}$ for $GaN$ thin films at 300 K (a), 500 K (b), and 800 K (c). . . . . 40

Figure 3.9. Comparison of $k_{tf-AS}$ and $k_{tf-MD}$ for $AlN$ thin films at 300 K (a), 500 K (b), and 800 K (c). . . . . 41

Figure 4.1. Thermal transport schematic for in-plane and out-of (cross)-plane heat conduction in graphene/substrate heterostructure. Heat transfer via convection and radiation is also shown. . . . . 43

Figure 4.2. Simulation box used for AEMD simulations. . . . . 46

Figure 4.3. Simulation box used for NEMD simulations. . . . . 47

Figure 4.4. Phonon dispersion of acoustic phonon modes of $h-BN$, $MoS_2$, $WS_2$, and $WSe_2$. ZA phonon modes are painted red. . . . . 50

Figure 4.5. DOS of all (a) and ZA phonon modes (0-7 THz) (b) of materials used in the study. . . . . 51

Figure 4.6. Phonon dispersion of acoustic phonon modes of $h-BN$, $h-BN/GaN$, and $h-BN/SiO_2$ of ZA phonon modes are painted red. . . . . 53

Figure 4.7. $TBC(MW/m^2K)$ of 1-4 layers $2D/GaN$ heterostructures. . . . . 54

Figure 4.8. $G$ $(MW/m^2K)$ of 1-4 layers $2D/GaN$ heterostructures. . . . . 55

Figure 4.9. Comparison between Equation (4.3), MD results, and literature. . 56

Figure 4.10. LA phonon modes of $MoS_2$,GaN, and $MoS_2/GaN$ heterostructure. 59

Figure 5.1. Simulation box for NEMD simulations. . . . . 63

Figure 5.2. Temperature distribution along the 2000 nm-thick $GaN$ subjected to 100 nm-thick (a) and 1000 nm-thick (b) localized heating region with the power of 50 mW. Red areas marked in plots represent the localized heating. . . . . 66

Figure 5.3. Temperature distribution along the 2000 nm-thick $GaN$ subjected to 100 nm-thick (a) and 1000 nm-thick (b) localized heating region with the power of 50 mW. Red areas marked in plots represent the localized heating. . . . . 67

Figure 5.4. Temperature distribution along the $GaN$ thin film (with same $L/g$ ratio) subjected to 50 nm thick and 100 nm thick localized heating with the power of 50 mW. . . . . 68

Figure 5.5. Local thermal conductivity along the 200 nm-thick GaN subjected to 50 nm-thick localized heating with 50 mW power. . . . . 69

Figure 5.6. Peak temperature of structures according to different $L/g$ values when subjected to 50 nm and 100 nm thick localized heating with the power of 50 mW (a) and 100 mW (b). . . . . 70

Figure 5.7. Temperature distribution along 200 nm thick thin film with 50 nm thick localized heating obtained from MD simulations, DM model with thermal conductivity calculated by improved TC-AS and extended TC-AS model. . . . . 72

# LIST OF TABLES

Table 3.1. Comparison of the calculated bulk wurtzite $GaN$ and $AlN$ thermal conductivities with data available from literature at 300 K. . . . . 33

Table 3.2. Comparison of $GaN$ thermal conductivities (W/m.K) obtained from TC-AS and NEMD simulations for selected thin film thicknesses. . 35

Table 3.3. Comparison of $AlN$ thermal conductivities (W/m.K) obtained from TC-AS and NEMD simulations for selected thin film thicknesses. . 35

Table 3.4. Standard atomic weight of atoms formed the materials and molecular mass of $AlN$ and $GaN$. . . . . 38

Table 3.5. Obtained parameters for Equation (3.2) . . . . . 40

Table 4.1. Lattice parameters (a=b) of crystalline 2D materials and $GaN$. . . 46

Table 4.2. TBC ($G$) values and average time delay ($\tau_n$) at the 2D/3D material interfaces. . . . . 49

Table 4.3. Phonon DOS mismatch in the range of $0 - 5$ THz and $G$ values of interfaces. . . . . 52

Table 4.4. Parameters obtained for Equation (4.3). . . . . 56

Table 4.5. Individual in-plane thermal conductivity (W/m.K) of 1 (1L), 2 (2L), and 3 (3L) layered 2D materials (isolated and in heterostructure) and their substrates. . . . . 58

# LIST OF SYMBOLS

| | |
|---|---|
| $c$ | Specific heat |
| $C$ | Spring constant |
| $H$ | Height of unit cell |
| $k$ | Thermal conductivity |
| $k_b$ | Boltzmann constant |
| $L$ | Characteristic Length |
| $m$ | Width of each slab in unit cell |
| $N$ | Number of unit cells in sample |
| $q$ | Wavevector |
| $T$ | Temperature in K |
| $W$ | Width of unit cell |
| | |
| $\Gamma_s$ | Substrate scattering rate |
| $\Lambda$ | Mean Free Path |
| $\tau$ | Relaxation time |
| $\Psi$ | Wave function |
| $\omega$ | Frequency |

# LIST OF ACRONYMS/ABBREVIATIONS

| | |
|---|---|
| 2D | Two dimensional |
| 3D | Three dimensional |
| AEMD | Approach to Equilibrium Molecular Dynamics |
| AlN | Aluminum Nitride |
| BB-FDTR | Broadband Frequency Domain Thermoreflectance |
| BTE | Boltzmann Transport Equation |
| DFT | Density Functional Theory |
| DOS | Density of States |
| FDTR | Frequency Domain Thermoreflectance |
| GaN | Gallium Nitride |
| h-BN | Hexagonal Boron Nitride |
| HCP | Hexagonal Closed Pack |
| HEMT | High ELectron Mobility Transistor |
| Kn | Knudsen Number |
| LED | Light Emitting Diode |
| MD | Molecular Dynamics |
| MFP | Mean Free Path |
| MOSFET | Metal Oxide Semiconductor Field Effect Transistor |
| $MoS_2$ | Molybdenum Disulphide |
| NEMD | Non Equilibrium Molecular Dynamics |
| $SiO_2$ | Silicon Dioxide |
| SW | Stillinger Weber |
| TDTR | Time Domain Thermoreflectance |
| TTI | Thermoreflectance Imaging |
| vDW | Van der Waals bonds |
| $WS_2$ | Tungsten Disulphide |
| $WSe_2$ | Tungsten Diselenide |

# 1. INTRODUCTION

## 1.1. Thermal Transport in Semiconductor Devices

The continuous efforts of scientists and engineers for developing new materials, tools, and processes allow us to build electronic devices (optical lasers, transistors, LEDs) with unique properties in short-length scales. The aggressive reduction in these devices, coupled with faster processing speeds, leads to a large amount of heat generation per unit volume in these devices. Further reduction in sizes and advancement depends on the efficient design of heat dissipation strategies. A rigorous understanding of heat conduction mechanisms at short lengths, complex structures, and interfaces is necessary to remove heat from these devices. An incomplete understanding of the physics of heat transport mechanisms inside the semiconductor devices and their constituent materials limits the performance, scope of implementation, and overall feasibility of these devices, primarily based on semiconductor micro/nanotechnologies [1].

### 1.1.1. Phonon Transport

Quantized lattice vibrations, called phonons, are responsible for heat transfer in insulators and semiconductors. Phonons are characterized by their directions, known as wavevector, and the amplitude of their frequency. The proportion of vibrational states per unit crystal volume occupied by phonons is known as **phonon density of states (PDOS)**. **Phonon dispersion relations** express the relation between phonon wavevectors and frequency as

$$\omega(k) = \sqrt{\left( C\frac{(M+m)}{Mm} \pm C\sqrt{\frac{(M+m)^2}{M^2m^2} - \frac{4}{Mm}\sin^2\frac{ka}{2}} \right)} \tag{1.1}$$

where $\mathbf{k}$, phonon wavevector, and phonon frequency, $\omega(\mathbf{k})$, in a chain contains two atoms with different masses [2, 3].

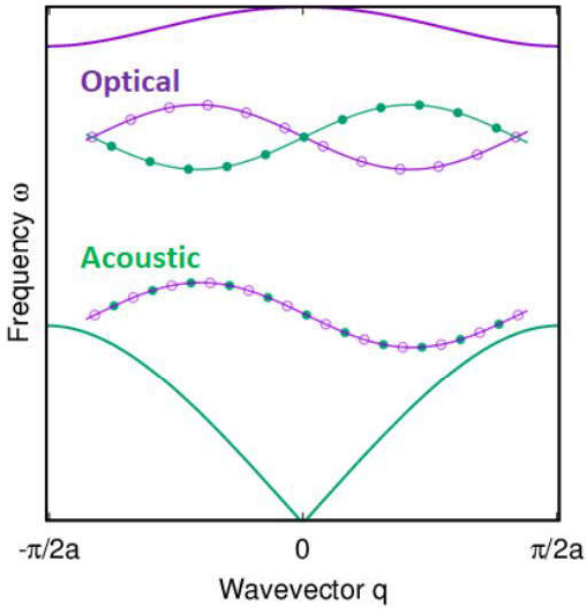



Figure 1.1. Phonon dispersion relation of the diatomic chain. Patterns of acoustic and transverse optical waves are also presented [4].

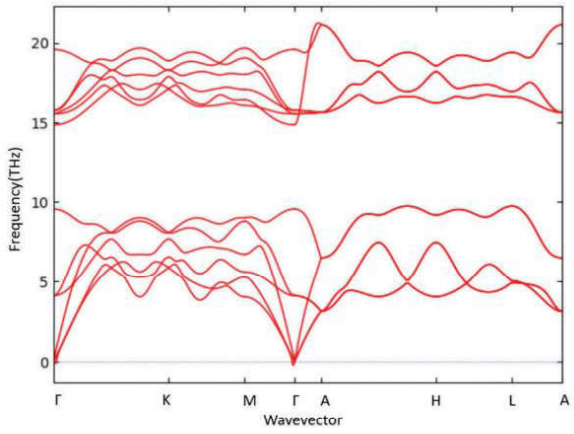



Figure 1.2. Phonon dispersion relation of GaN thin film [5].

Atomic vibrations are modeled as masses connected with spring to reach Equation (1.1). $C$ is the spring constant, $M$ and $m$ denote the masses of atoms in the diatomic chain. The eigenvalue problem showed in Equation (1.1) provides two types of solution: optical and acoustic solutions, which denotes the optical and acoustic phonon modes as shown in Figure 1.1. The $\pm$ term in Equation (1.1) cause the two types of solution.

Atoms in acoustic mode move in the same direction while particles move in oppositely in optical mode. More acoustic and optical branches are observed in three-dimensional materials, as shown in Figure 1.1. In Figure 1.2, some specific notations ($A$, $\Gamma$, $M$, and $K$) denote the crystallographic directions in primitive cells. Figure 1.3 describes these lattice directions of the first Brillouin zone of hexagonal close-pack (HCP).

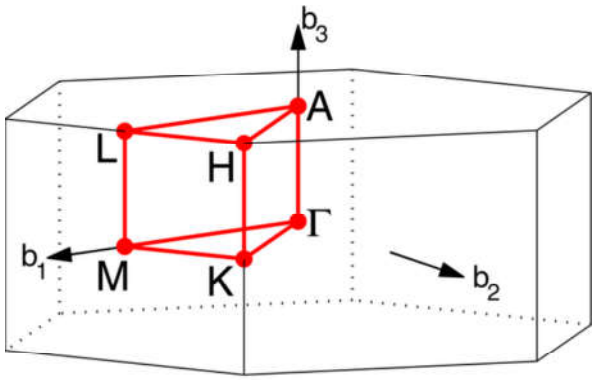



Figure 1.3. First Brillouin zone of HCP structure [1].

For more than 200 years,Fourier's Law of Conduction has been used to describe heat propagation in macroscale structures. This law accurately describes the heat transfer in bulk materials when the device size or characteristic length becomes comparable with the dominant heat carrier's average mean free path (MFP), the average distance that heat carriers travel between two successive collisions with other heat carriers, defects, or impurities. Since this law is based on the thermal equilibrium of heat carriers and an assumption of continuum behavior, inaccuracy of this law becomes larger when ballistic-diffusive effects have emerged. Ballistic-diffusive effects become dominant when the device size or characteristic length of the material becomes comparable with the MFP of the energy carrier, or the timescale of the interest is on the order of the thermal relaxation time of the energy carrier [6, 7].

Figure 1.4 shows the thermal resistivity change in different phonon transport regimes. At low inverse Kn numbers, the ratio of characteristic length of the geometry to MFP of energy carrier, heat is transport in the fully ballistic regime and obeys the predictions of Boltzmann Transport Equation (BTE). Here, thermal resistivity is

much higher, and a function of the size of structure since phonons may travel through the medium without any energy dissipation and deposit their energy nonlocally. With increasing inverse Kn number, ballistic effects diminish, and energy carriers transport heat in accordance with Fourier's law of conduction. In quasi-ballistic (i.e., ballistic-diffusive) regime, both ballistic and diffusive regimes are observed, and thermal properties, for example, thermal conductivity and resistivity, become a function of the size. Most semiconductor devices used are in this length scale. Therefore, a complete understanding of ballistic-diffusive effects on thermal transport is necessary to build an effective thermal management strategy for semiconductor devices [3, 6].

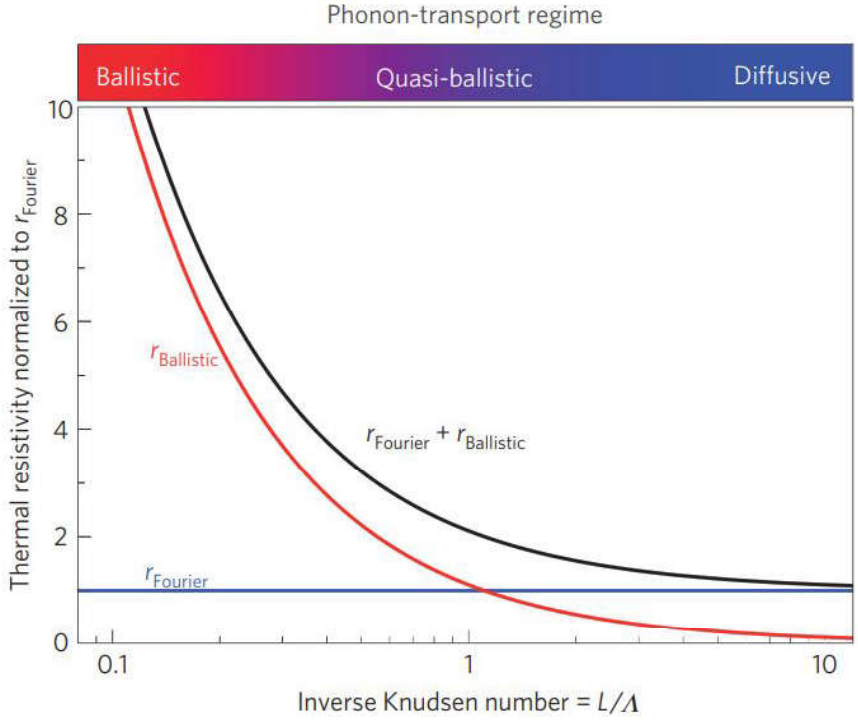



Figure 1.4. Analytical prediction of the Fourier (diffusive) and ballistic components thermal resistivity away from a half-cylinder. Reprinted by permission from Nature Materials [8]. License number: 5136500889973.

## 1.2. Ballistic-Diffusive Thermal Transport

This section will briefly introduce phonon transport at three structures where quasi-ballistic effects dominate: thin films, interfaces at 2D materials, and localized

heating regions.

### 1.2.1. Thin Films

A thin film is a layer of materials with thicknesses of nanometer to several micrometers. Thin films are widely used in many micro-and nanoscale applications, such as high electron mobility transistors (HEMTs), light-emitting diodes (LEDs), and optical lasers [3, 9]. In these structures, the film thickness becomes comparable to the phonon MFP, and the physical boundaries of the structures lead to additional scattering mechanisms which cause the change in thermal properties. Increased phonon-boundary movement restricts phonon movement, which leads to a significant reduction in the thermal transport through these structures [10].

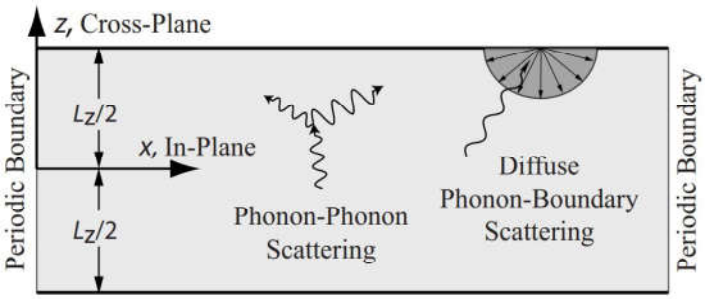



Figure 1.5. Schematic diagram of phonon transport and scattering mechanisms in the thin film. Thermal transport is confined in z-directions. Periodic boundary condition denotes infinitely long thin in x- and y-directions [11].

Figure 1.5 shows the different phonon scattering mechanisms in thin films. Besides the phonon-phonon scatterings, phonon-boundary scatterings happen more frequently. Therefore, nature of interaction of these scatterings is key to understand the size effects caused by these boundaries. Diffuse phonon-boundary scatterings indicate that the angle of the reflected wave is arbitrary, while specular scatterings refer to that angle of incident and reflected waves are the same. [7, 12].

Phonon MFP is an essential parameter to understand the boundary scattering effects. Recently, thermal conductivity accumulation spectra (shortly, accumulation

spectra) with respect to phonon MFP, as shown in Figure 1.6, is obtained the phonon MFP and thermal conductivity of materials which are essential parameters for thermal characterization of the semiconductor devices. Accumulation spectra have been built for various materials using theoretical and experimental studies to relate the phonon MFP and thermal conductivity of materials [5,13,14]. Yang and Dames [10] developed a function for accumulation spectra and built spectra for $Si$ by using this function. The broadband frequency-domain thermoreflectance method is used to build accumulation spectra for $Si$ and $SiO_2$ by Regner et al. [14] and four different materials by Freedman et al. [15]. Beechem et al. [16] and Sood et al. [17] built accumulation spectra for $GaN$ and $MoS_2$, respectively. Albar and Donmezer built accumulation spectra for GaN and AlN thin films [5, 18] using ab-initio based models. Molecular dynamics and lattice dynamics-based approach was used to calculate an accumulation function for $Si$ and $SiO_2$ by Larkin and McGaughey [19].

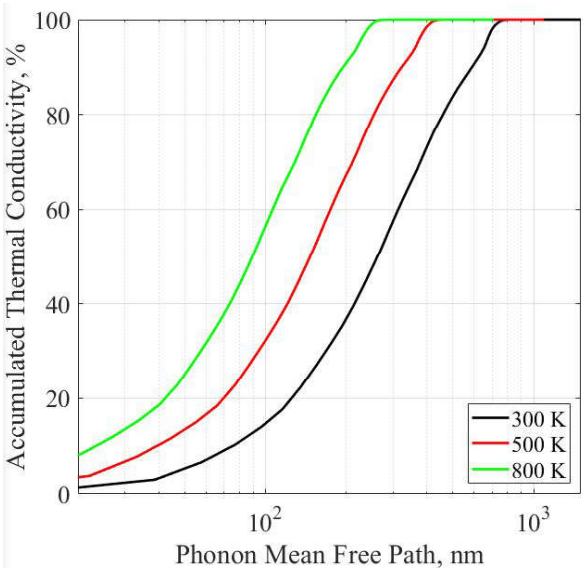



Figure 1.6. Thermal conductivity accumulation spectra with respect to phonon MFP for GaN-based on ab-initio calculations at different temperatures [5].

### 1.2.2. Interfaces at 2D Materials

Semiconductor devices contain several material layers and interfaces, and these interfaces become denser with shrinking device size and interrupt the regular crystal

lattices in which phonons propagate. An interface not only produces thermal resistance between layers but also changes the in-layer thermal transport.

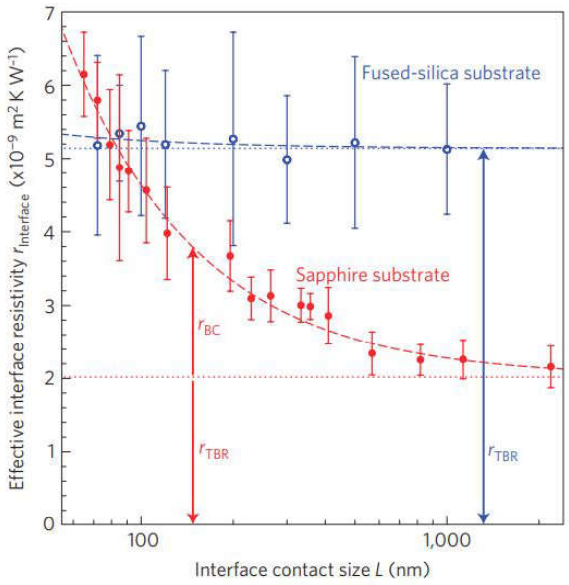



Figure 1.7. Thermal boundary resistance with respect to contact size. Reprinted by permission from Nature Materials [8]. License number: 5136550279497.

The presence of an interface affects both cross-plane and in-plane thermal conductance within the materials that constitute the interface. Since the density of interfaces in devices become higher in small structures, effect of interfaces become even more dominant when the device and contact size is smaller as shown in Figure 1.7. Therefore, in 2D devices, thermal transport is dominated by the interfaces. These interfaces change the material properties of regions near-interface and phonon transport are changed. Appropriate operating conditions and power dissipation from active regions in high-power electronic devices can be achieved with high thermal conductance in both in-plane and cross-plane directions. The efficacy of cross-plane thermal transport through an interface is characterized with thermal boundary conduction, $\mathbf{G}$, which relates the heat flux, $\mathbf{q}$,and temperature change, $\delta T$ through the interface between materials [20–22].

Since Kapitza did the first measurements of TBC of interfaces in 1941, the conductance across an atomically thin interface sometimes refers as Kapitza conductance.

Even though TBC mainly refers to broader interfaces, Kapitza conductance helped understand the TBC concept. Even at a perfect interface, thermal resistance between two dissimilar materials does not vanish. Thermal boundary conductance (TBC) is a critical thermal property that dictates heat dissipation or confinement through interfaces in various electronic and optoelectronic applications. However, in applications that require low conductance, such as thermal barrier coatings and thermoelectric materials, interfaces may play a role in low thermal conductance. Complete understanding of the role of interfaces in thermal transport in heterostructure devices is essential to fully realize the potential of these applications and device [23–25].

Due to its importance for thermal characterization, researchers have studied the relationship between interfacial properties and TBC of semiconductor devices and materials. Studies show that phonon dispersion and density of states (DOS) of materials that constitute the interface have a tremendous impact on the TBC of the devices. Moreover, since the quality of the interface and temperature can change the vibrational properties of phonons, these factors affect the TBC and heat conduction in semiconductor heterostructures and devices [21, 26–28]. Heat conduction at the interface also affects the thermal transport regions near interfaces and thermal transport properties at the regions near interfaces. Moreover, thermal resistance at even a perfect interface does not vanish.

### 1.2.3. Localized heating

The performance and functionality of the semiconductor devices, such as LEDs and HEMTs, depend on the control of charge flow within device layers. Flow charge in the device is controlled by applying a potential difference on the region where the charge moves. Depending on applied potential difference to the region, electrons may gain a high amount of kinetic energy, particularly in high-power electronic applications. Moving electrons with high kinetic energy may transfer their energy via scatterings with the defects, electrons, and phonons. This causes self-heating phenomena in solid-state devices. The kinetic energy transfer from electrons to phonons causes heat generation, i.e., Joule heating, within semiconductor devices [29–31].

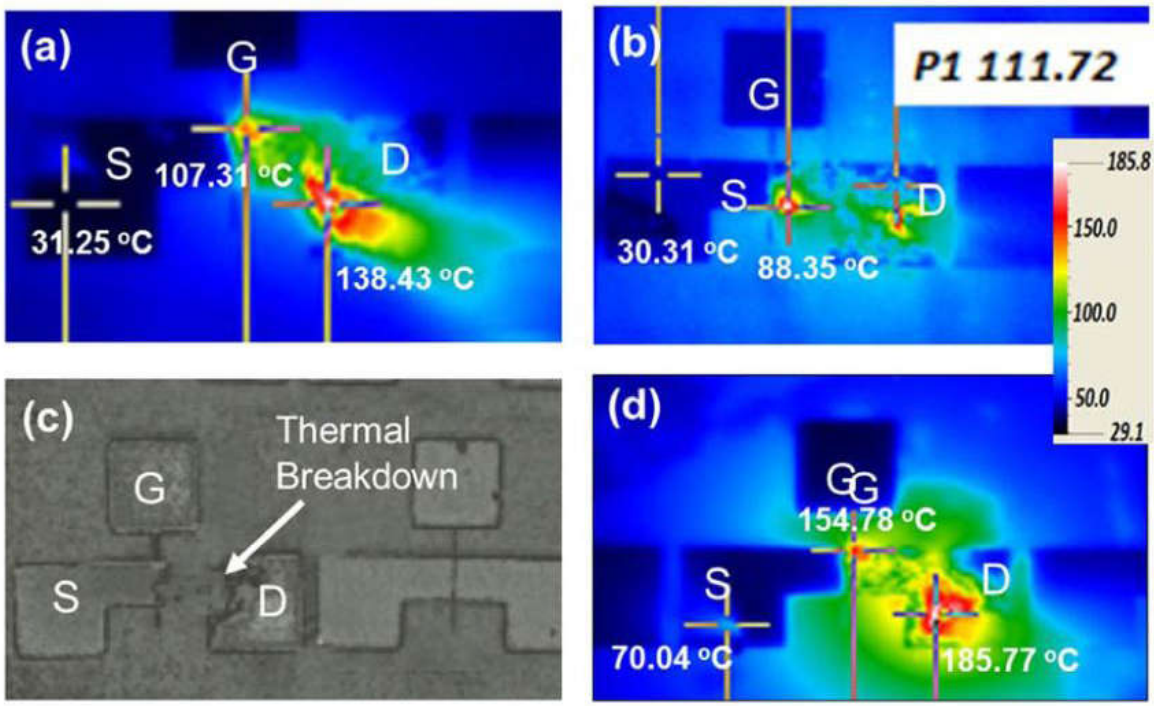



Figure 1.8. Temperature distribution of the device channel without (a) and with a Cu-filled (b) micro-trench at a power density of 11.57 and 12.61 W/mm. Thermal breakdown in HEMT without a trench (c) and no breakdown with a trench at an applied voltage bias of 200 V [32].

Temperature rise stemming from localized heating affects charge concentration, mobility, and electrical conductivity inherently. Therefore, increased operating temperature impairs control of device behavior, as shown in Figure 1.8 (a)-(c). Moreover, increasing the device density leads to overheating and causes reliability and performance issues in semiconductor devices, such as fin FET and MOSFET. Phonons propagating through a heating region in the size of MFP of heat carriers cannot scatter and exchange energy with high energy phonons generated in this region. Thus, heat cannot dissipate from this region and thermal conductivity reduces due to the thermal size effects. Hence, small heating areas in integrated electronics is a limiting factor to power dissipation in this scale and cause a temperature rise in local temperature in the components of nanoscale devices. Higher device temperature also changes in the material's electrical resistivity. Nanometer-sized hot spots of up to hundreds of Celsius

of temperature have a significant impact on device performance and reliability. Characterizing the local temperature variations in nanoscale devices and the temperature of hot spots is crucial for building thermal management strategies to dissipate heat effectively [33–35].

## 1.3. Thermal Characterization of the Ballistic-Diffusive Effects

The above section summarizes three examples where ballistic-diffusive effects were observed. Due to ballistic-diffusive effects, heat conduction and phonon transport in nanoscale materials and devices become different from bulk counterparts. Since these effects change the thermal behavior of these devices at these scales, thermal characterization is necessary. This section summarizes the methods used to characterize quasi-ballistic effects in thin films, at interfaces, and near localized heating regions.

### 1.3.1. Thin Films

Since the size of the material is on the same scale as phonon MFP, increased phonon-boundary scatterings and classical size effects become dominant. In this scale, the thermal conductivity of thin films becomes length-dependent. Since measuring and calculating thermal conductivity for each thin film, thin film thermal conductivity can be obtained via accumulation spectra built via experimental [14–16] or theoretical [5, 18, 36] methods. These methods are introduced in the next sections.

**Experimental**: Experimental thermal characterization methods used to obtain thin film thermal conductivity focus on either measuring the temperature distribution in the thin film or thermal properties linked to the thermal conductivity of materials. The Micro-Raman method applies a single laser beam to the sample and directly measures the temperature of the thin film. By using a thermal model and temperature rise, thin film thermal conductivity is estimated. Due to its simplicity, it is widely used in thin-film thermal conductivity calculations [29, 37]. On the other hand, thermoreflectance methods, such as time domain and frequency domain thermoreflectance (TDTR and FDTR), use two laser beams to calculate the thermal conductivity of a

thin film: a 'pump' beam to heat the sample and 'probe' beam to measure the change in surface reflectivity of the thin film sample. For small temperature changes, the change in surface reflectivity is proportional to surface temperature change by the thermoreflectance coefficient of the material. The sample is coated with a thin metal transducer film that absorbs light at pump wavelength with a large coefficient of thermoreflectance at probe wavelength [38, 39]. In FDTR, instead of monitoring the time delay between pump and probe beams, thermoreflectance is measured as a function. Its implementation is much easier than TDTR since it avoids the complexity of collecting time delay and using inexpensive laser sources. However, the FDTR method has a low signal-to-noise ratio at modulation frequencies higher than 20 MHz, and this causes low accuracy in measurement [40, 41]. Broadband FDTR (BB-FDTR) method is used to overcome this issue and extend the modulation frequency to 200 MHz. However, measurements are challenging at these high modulation frequencies due to small thermal penetration depth and self-heating effects [15]. The 3-$\omega$ method also measures the thermal conductivity by calculating another parameter related to thermal conductivity. Instead of surface thermoreflectance, 3-$\omega$ measures the harmonic temperature rises across a metal strip deposited on the thin film substrate. The third harmonic is used to measure the thin film thermal conductivity. Since it allows measuring thermal conductivity at a vast range of temperatures, it is a popular experimental thermal characterization method for thin films [42–45].

**Theoretical**: Despite their advantages, experimental methods are expensive, and their accuracy is restricted with setup and measurement difficulties. Moreover, statistical uncertainties can occur when the quantum effects are dominant. Theoretical thermal characterization at ballistic – diffusive regime is necessary since they help reduce the cost of the estimations and provide helpful insight into thin-film thermal conductivity. Atomistic Green's function (AGF), ab-initio calculations, and molecular dynamics (MD) are three common methods used to calculate the thermal conductivity in in-plane and cross-plane directions. While AGF and ab-initio calculations solve these equations in the frequency domain, MD makes its calculations in the time domain. These models use some functions to describe the interaction between atoms, i.e., interatomic potentials, derived from first-principles or experimental studies [46–49].

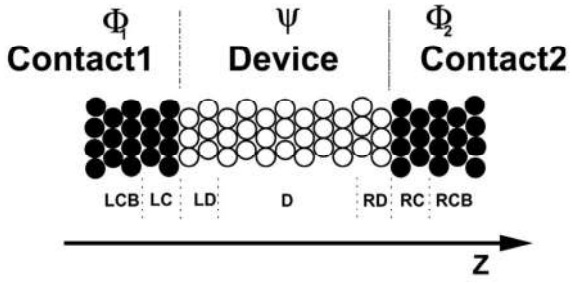



Figure 1.9. Atomistic Green's function model [49].

AGF technique studies the electron and phonon transport in thin film and is efficient at phonon-boundary scatterings. In this method, the thin film is behaved as a device between two contacts, as shown in Figure 1.9. The "Device" is represented by LD, D, and RD groups, and its geometry and boundaries with the contact are arbitrary. Here LC and RC atoms have bonds with the atoms in "Device" but, LCB and RCB atoms have no interactions with the "Device" atoms. Thermal conductivity calculations start with the construction of harmonic matrices for the device and contacts. Then, uncoupled Green's functions and transmission functions at any frequency are calculated. By using these results, heat fluxes and thermal properties are calculated. This method is limited to use at low temperatures since it uses the harmonic force constants. However, it can be extended to add the anharmonicity of phonons [49, 50]. Another useful method for computing thermal properties is ab-initio calculations. This model relies on substituting plane-wave solutions for the incident, reflected, and transmitted waves at an interface. While other methods oversimplify the electronic contribution to materials' thermal properties and electronic structure, ab-initio calculations consider electronic properties for phonon calculations [51–53]. Instead of calculating thin film at a specific thickness value, this model is mainly used to build thermal conductivity accumulation spectra with respect to the MFP of the energy carrier or its frequency [5, 18, 54]. Phononic contributions to thermal transport are calculated by using lattice dynamics or perturbation theory following DFT. Despite its high accuracy, implementing this method for an extensive system is almost impossible and not feasible in practice due to very high computational power requirements.

Aside from these methods, MD is a powerful tool to obtain the thermal properties of the thin film. MD solves the many-body problem by using numerical approaches to solve Newton's equations of motion for all atoms and molecules in the thin films. MD has the advantage of simulating real-size structures, even though it cannot calculate the quantum effects. While DFT is used to obtain the thermal properties of materials with a size up to several nanometers, MD simulations can use domains on micrometers [55–57]. Interatomic potentials built according to ab-initio calculations or experimental studies are used to describe the interactions between atoms. Boundary conditions are also used to create the domain used for calculations. Proper interatomic potentials, boundary conditions, and thermostats are required for accurate results. Moreover, computational power requirements are exponentially increased with the larger domain and more atoms, increasing the accuracy of the model. Despite its high computational power requirements and need for proper interatomic potentials, MD simulations are beneficial for phonon studies since they can take phonon anharmonicity and high order phonon interaction into account very accurately. In this thesis, the thermal conductivity of thin films is investigated using this model because of its success in modeling the phonon properties of materials.

### 1.3.2. Interfaces with 2D Materials

Both experimental and theoretical methods used to obtain the thermal properties of thin films and interfaces are the same in principle. However, there are some differences in applications. Since interfaces play a vital role in micro and nanoscale devices, an accurate approach to calculate these properties is essential. Most measurements and calculations in the thermal characterization of interfaces focus on the TBC.

**Experimental**: Raman spectroscopy is very popular in the thermal characterization of interfaces. TBC and in-plane thermal conductivity are measured by converting the Raman shifts into temperature and using a 1D heat approximation. TDTR method has been used to measure the thermal properties of interfaces due to their non-contact and non-destructive nature. By measuring the surface reflectivity via two lasers, temperature changes can be easily obtained. Thermoreflectance phase shift and

pump bean modulation frequencies are observed to understand the thermal response of the interface heated by the pump beam. Other thermoreflectance methods, FDTR and BB-FDTR, are also used in these calculations, as well. Despite their high accuracy, experimental methods cannot provide the thermal properties of materials in contact, and they can be used to lumped-value TBC. So, the effect of encapsulation or deposited materials for measurements cannot be identified. Since encapsulation or deposited material changes phonons' vibrational properties, TBC and thermal conductivity measurement may not be accurate, especially 2D/3D interfaces. Therefore, theoretical methods are also widely used for these calculations [24, 58–60].

**Theoretical**: The acoustic mismatch model (AMM) and diffusive mismatch model (DMM) are popular methods to calculate the TBC and other interfacial properties at low temperatures. In AMM calculations, interfaces are assumed to be specular; all phonons obey Snell's law, reflecting or transmitting. Meanwhile, directions and polarization of phonons become arbitrary after they hit the interface. The transmissivity of phonons is not related to the angle of incidence of phonons or their polarization. Although these models are consistent with the experiments at low temperatures, these models cannot model the phonon transport at high temperatures. However, MD models can provide more accurate results at a more extensive temperature range since it allows to explore the interface energy coupling and assess the surface roughness and morphology of materials formed the interface. MD calculates the TBC of interfaces between materials by calculating the temperature difference between both sides, and heat flux caused the heat transfer along with the material, similar to experimental studies. Some MD algorithms, such as NEMD and AEMD, can simulate exact experimental structures, which is the most significant advantage of MD in these calculations. Moreover, MD can provide useful insight into thermal transport and interfaces since it can capture phonon anharmonicity and high-order phonon-phonon scatterings, which frequently happen at the boundaries. DFPT simulations are used to calculate the TBC and vibrational properties of materials in contact. Here, bonds between atoms on the surfaces of materials are calculated in accordance with the classical harmonic spring model, which assumes that bonding between materials is a spring with a certain coupling constant. Then, DFPT calculates the energy transferred through the springs and

obtains the TBC. Despite the accuracy of the model, this model cannot represent the actual experiments, like MD simulations did [24, 27, 61, 62].

### 1.3.3. Localized Heating

Hot spot temperature caused by localized heating is essential for device designs since it is the peak temperature value in devices. Due to its importance, accurate estimation of hot spot temperature is a necessity. Various experimental and numerical methods are used for this, depending on the desired accuracy and resolution.

**Experimental:** For device characterization, optical methods have been widely used in semiconductor devices since they are non-contact methods and can obtain the temperature map of the device with high resolution. Each method has a unique implementation area and spatial resolution. For instance, researchers have been investigated the channel temperature of the transistor and junction temperature of the LED devices by using thermoreflectance imaging (TTI) and Raman thermometry with high resolution. While the micro-Raman method can provide micrometer-scale resolution ($\approx 1$ $\mu$m), TTI can provide sub-micro resolution on surfaces; however, it cannot achieve the same resolution in the inner layers of the structure. Hence, measuring the temperature of hotspots away from surfaces is complicated and less accurate due to lower resolution. Some thermal models are used to understand the behavior of such hot spots. Despite the common use of these methods, resolution of the methods and uncertainties caused by experimental setups may lead to erroneous results. Moreover, the accuracy of these methods is also dependent on the parameters and assumptions used in the thermal models, especially for the buried and small hot spots [34, 35, 63–65].

**Theoretical:** In device characterization, theoretical and numerical methods are used with or instead of experimental methods. Device size models, phonon BTE and finite elements are widely used with the experiments to obtain the temperature profile. The Boltzmann Transport Equation can be implemented to describe the size effects on

thermal transport, as shown in

$$\frac{\partial f}{\partial t} + \overrightarrow{v}.\nabla f = \left(\frac{\partial f}{\partial t}\right)_{scatterings} \tag{1.2}$$

where $f$ is the distribution function of phonons and $v$ is the group velocity based on the distribution function. The right-hand side term describes phonon distribution changes due to the collisions between phonons with other phonons, defects, boundaries, isotopes, electrons, and crystal defects [66–68]. Due to its complexity, the quation (1.2) is cannot be solved analytically, and thus, numerical approaches are needed to solve it. Therefore, numerical approaches are needed to solve this equation. One of the most popular approaches is the gray model. Gray model simply uses a phonon with a certain phonon MFP, group velocity, and relaxation time to represent all the phonon modes in the structure. Even though it is straightforward and has low computational requirements, its accuracy is low, especially for semiconductor materials with a large phonon MFP spectrum [7].

Due to the requirement for a large structure to simulate the hot spots, atomistic models like DFPT and MD are mainly used to provide the necessary parameters for numerical methods. Ab-initio calculations are often used to provide phonon MFP spectrum and group velocity, while MD simulations sometimes are used to provide insights to solutions of phonon BTE for phonon-boundary scatterings since it can accurately observe these scatterings [7, 10].

MD simulations have been implemented through this thesis for all these structures due to the advantages provided above. More details about the MD are given in the following section.

## 1.4. Motivation

As it explored in previous sections, thermal transport in semiconductor devices deviates from the continuum thermal transport behavior when the size of the structure

become comparable with phonon MFP or localized heating effects are emerged. This behavior may lead devices to heat unexpectedly which affect the overall performance and reliability. Therefore, many researchers focused on characterizing the thermal transport in this regime and show the impacts of it on the thermal behavior of devices. Experimental characterization methods can provide useful insight on thermal transport, the accuracy heavily depends on the approximations and fitting parameters used. Also, experimental approaches need a significant amount of time and effort, and their set ups and samples are costly. Theoretical characterization methods, such as solutions of phonon BTE, often requires simplifications to reduce complexity and computational cost. Other methods like ab-initio calculations cannot observe the effect of phonon-boundary and phonon-impurity scatterings, which are essential to have a rigorous understanding for ballistic-diffusive thermal transport. MD is a great tool to observe the quasi-ballistic effects on thermal transport. Yet it has computational cost for relatively large structures, currently there is a need for simple relations to explain the quasi-ballistic effects based on widely available phonon data in literature. The main motive of this thesis is to observe the trends in ballistic – diffusive thermal transport using MD simulations and relate them to the material and phonon properties to obtain such relations for thin films, interfaces, and localized heating. Obtained relations will help the researchers to characterize the importance and impact of size effects in a relatively simple manner from present data regarding phonons and material properties available in the literature.

## 1.5. Outline of the Thesis

The following sections of the thesis have the final aim to investigate the phonon transport at the ballistic-diffusive regime and provide insight on thermal characterization at this regime. To achieve that, molecular dynamics simulations are carried out via LAMMPS. In Chapter 2, an insight on methodology of this thesis is introduced. Introduction provided definitions of notations related to the study and ballistic-diffusive heat transport regime. Then, in Chapter 2, theoretical basis of MD simulation schemes used in this study and required equations are introduced.

Chapter 3 will provide findings on thermal transport through thin films and length-dependent thermal conductivity. A new mode based on accumulation spectra, TC-AS, is proposed to investigate the classical size effects on thermal transport in thin films and estimate the thin film thermal conductivity. Then, the accuracy of the model is investigated for GaN and AlN thin films by comparing the results with thermal conductivity calculations via NEMD simulations. Using these comparison, a fitting function is introduced to improve the accuracy of TC-AS model. This function relates the phonon scattering mechanisms and material properties to thermal conductivity of materials.

In Chapter 4, thermal transport at 2D/3D van der Waals heterostructures is investigated. To investigate the cross-plane and in-plane thermal conductance, the TBC and in-plane thermal conductivity of eight 2D/3D material pairs are calculated. Also, the effect of lattice mismatch, phonon DOS mismatch, and the number of 2D material layers on TBC and cross-plane thermal transport are evaluated. Moreover, a relation is proposed to relate the TBC trends to material properties. Then, the in-plane thermal conductivity of materials (isolated and in heterostructure) obtained by NEMD simulations is presented and trends in in-plane thermal conductivity change are investigated thoroughly.

Chapter 5 will provide findings of this work on thermal transport near localized heating areas and the effect of phonon localization. By applying localized heating regions with different thicknesses and heat fluxes, temperature distribution and local thermal conductivity change in bulk materials are investigated. After localization effect is observed in bulk materials, same localized heating regions are applied to thin films, then peak temperature and local thermal conductivity changes are also examined.

Finally, Chapter 6 will focus on the findings in this thesis. Deductions from Chapters 3, 4, and 5 will be discussed. Accordingly, future research areas are suggested.

# 2. MOLECULAR DYNAMICS

MD relates the microscopic behavior of atoms of the materials and their thermal properties using statistical mechanics approaches. At each instantaneous time, each atom's position, velocity, and momentum are calculated, and thermodynamical variables are calculated by averaging these values. Here, this method uses the ergodicity hypothesis of statistical mechanics. Ergodicity hypothesis states that the time average is equal to the ensemble average; therefore all thermodynamic variables of structure can be calculated by time-averaging the calculations at an instantaneous time [55, 69].

In MD simulations, calculations are started by introducing the interatomic potentials that can accurately describe interactions between atoms in the system under investigation. Then, each atom's initial positions and velocities are created, and neighbors of each atom are listed. Mostly, atoms are at their equilibrium positions, and their velocities are randomly assigned according to Gaussian distribution. Then, forces applied on each atom are calculated using interatomic potentials, and Newton's equations of motion are calculated numerically to determine the position and velocity of each atom in the next step. Finally, after a long enough simulation time, thermodynamical variables are calculated. In these simulations, heat sinks and sources create heat flux and realize the canonical ensemble [55, 70, 71]. Boundary conditions are used to define the domain. Periodic boundary condition (PBC) is applied to approximate the bulk structure. Introducing periodic boundary conditions to a system is equivalent to considering an infinite array of identical copies of the simulation domain. Periodic boundary condition also has the wraparound effect that an atom within a cutoff distance of a boundary interacts with atoms near the opposite boundary. However, fixed boundaries also can be applied to create finite size systems and introduce the physical boundaries of structure [69, 71, 72]. In MD simulations, the motion and position of atoms are calculated by using functions that describe the interactions between atoms called interatomic potentials. These potentials explain intramolecular potentials describing the effects of bonding interactions. For semiconductors, mostly Stilinger-Weber (SW) potentials and Tersoff potentials are used to incorporate two-body and

three-body terms and are designed to favor tetrahedral atomic structures.

NEMD simulation solves Newton's second law of motion to position and velocity of each atom numerically at each timestep [71, 73]. Numerical integration of Newton's law is calculated by implementing a velocity Verlet algorithm [69] with a timestep of 1 fs for equilibration runs, and 0.5 fs for simulation runs. Velocity Verlet algorithm helps us to calculate the position from

$$r(t + \Delta t) = r(t) + \frac{1}{2}a(t)\Delta t^2, \tag{2.1}$$

velocity of each atom at half time as

$$v(t + \frac{1}{2}\Delta t) = v(t) + \frac{1}{2}a(t)\Delta t, \tag{2.2}$$

and acceleration of each atom at each timestep by

$$a(t + \Delta t) = \frac{-V(r(t + \Delta t))}{m}. \tag{2.3}$$

Then, the velocity of each atom at each timestep is calculated by

$$v(t + \Delta t) = v(t + \frac{1}{2}\Delta t) + \frac{1}{2}a(t)\Delta t. \tag{2.4}$$

Positions and velocities of each particle in the simulation domain are determined during the MD simulations. Force applied on each atom will change when the position of atoms and their neighbors move. Since the movement of all these particles is coupled together, Newton's equation of motion should be solved numerically. The most common numerical integration algorithm is the velocity Verlet method [74]. It calculates the position and velocity through two-step evaluation as presented in Equation (2.1) – (2.4). Here, $r$ is the position, $v$ is the velocity, $a$ is the acceleration, and $V$ is the potential of each atom in the system. The timestep is an important factor for any integration algorithm since small timesteps cause much more computational power

requirements than necessary, and large timesteps cause energy overlaps between atoms and failure of the simulation. Therefore, for solids, time step between 0.1 fs – 1 fs is suggested [55, 69, 75].

For thermal characterization of structures and thermal conductivity calculations, the temperature of the system should be calculated. The temperature of the system or part of it in MD simulations is calculated by using the equipartition theorem as

$$T = \langle \sum_{i=1}^{N} m_i . v_i^2 \rangle / 3Nk_B \tag{2.5}$$

where, $N$ is the total number of atoms in the structure, $k_B$ is the Boltzmann's constant, $m_i$ and $v_i$ is the position and velocity of atom i, and the angular bracket denotes the ensemble average. For these calculations, heat baths are introduced to set the temperature at aimed value. In MD simulations, two types of heat baths are used: deterministic heat baths, like Nosé-Hoover thermostats, and stochastic heat baths, like Langevin thermostats. While Nosé-Hoover thermostat uses a function to rescale the velocity of atoms in thermostated region, Langevin thermostat applies an excitation which is in agreement with Brownian motion and a random force applied on atoms in heat baths [69, 76].

There are many types of MD simulations. Most comment MD approaches used for thermal calculations are the Green – Kubo method, which relies on the fluctuation – dissipation theorem, and non-equilibrium MD (NEMD) methods, which rely on Fourier's law of conduction [77, 78]. Moreover, new methods like approach-to-equilibrium MD are also used to calculate thermal properties like thermal conductivity and thermal boundary conductance [79, 80]. Besides thermal conductivity calculations, the fluctuation – dissipation theorem is also used to obtain the phonon properties, such as phonon dispersion and phonon density of states [27, 56]. In the following sections, MD methods used in this thesis are introduced. NEMD simulations are used to calculate the temperature distribution and thermal properties of nanoscale structures. AEMD method is applied to obtain the thermal boundary conductance at interfaces between

2D materials and their substrates. For phonon DOS and dispersion calculations, an approach based on the fluctuation-dissipation theorem is used.

## 2.1. Non – Equilibrium Molecular Dynamics

Two different methods in NEMD simulations can be used to calculate the thermal conductivity and thermal properties of the materials. One method is to apply temperature difference to create heat flux, and the other one is by using thermostats. The first method is similar to real experimental methods. In this method, the temperature of the two regions is kept constant by applying thermostats, mostly Langevin thermostats. Due to the temperature difference of these regions, heat flux is created. Temperature distribution along the direction of heat conduction is obtained by using the equipartition theorem [69].

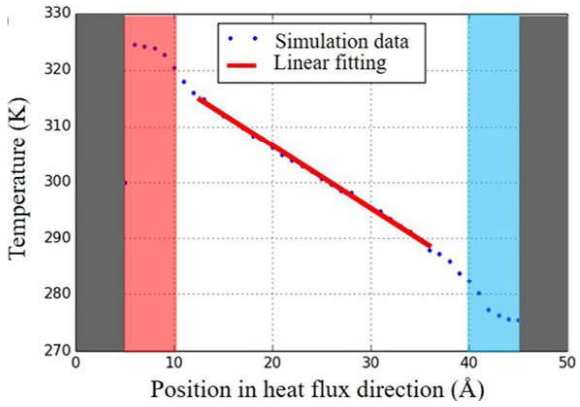



Figure 2.1. Temperature distribution obtained from a NEMD simulation [81].

To obtain thermal conductivity of material using NEMD, temperature distribution should be obtained. To do that, some divide the simulation box into small subdomains and calculate the temperature of these small regions. Even though long simulation times are required to obtain the converged temperature distribution and heat flux, it is desirable since it fits more to the actual physical picture and fluctuation-dissipation theorem and takes Brownian motion into account when Langevin thermostats are used. In the latter approach, fixed heat flux is applied to the thermostats by exchanging or scaling the velocity of particles at the thermostated regions. This model is relatively

faster since temperature converges faster than heat flux. However, this model is lacks of fundamental basis and not consistent with the physical picture of thermal transport by contrast with the first model [55, 76]. Both model are used in accordance to the physics of the study. Since the first model fits more to physical picture of thermal transport through thin films and interfaces, this model is selected for these simulations. The second model, rNEMD, is applied to model the effect of localized heating in semiconductor materials.

Regardless of the applied heat bath, obtaining the temperature gradient is the main goal here. For both thermal conductivity and thermal boundary conductance, the temperature distribution of the model is plotted as shown in Figure 2.1. In this model, two heat bath is applied at the end of the simulation box. Near thermostated regions, the temperature distribution is non-linear. For thermal calculations, these regions are neglected. In a linearly fitted area, the thermal conductivity of a material is obtained by diving the associated conjugate heat flux and temperature gradient using Fourier's law of heat conduction [77, 82] as

$$q_x = k_x \frac{\partial T}{\partial x}. \tag{2.6}$$

NEMD is a very successful tool to calculate the TBC of interfaces, especially semiconductor and insulator materials, since it can accurately capture the phonon scattering physics and phonon anharmonicity of materials. However, TBC calculations from NEMD require creating sandwich structures or applying heat sources away from the interface. In such structures, hot and cold thermostats are applied on opposing ends, and the TBC is calculated based on the temperature drop at the interface, as shown in Figure 2.2., using the equation of

$$\mathbf{G} = \frac{\mathbf{q}}{A.\Delta T} \tag{2.7}$$

where $\mathbf{q}$ is the heat flux through the interface, $A$ is the interfacial area, and $\Delta T$ is the

difference between two sides of the interface. However, such structures cannot always replicate the experimental setups without a superstate, affecting the interfacial heat flow. Therefore, the NEMD model is not chosen to calculate the TBC of interfaces between 2D and 3D materials [83, 84].

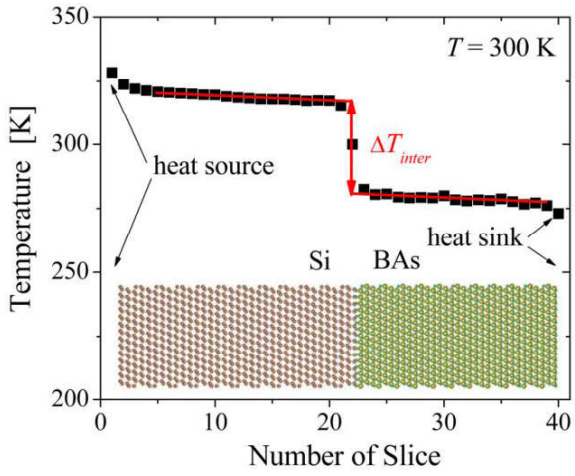



Figure 2.2. NEMD simulations for TBC of Si/BAs heterostructure [85].

## 2.2. Approach to Equilibrium Molecular Dynamics

While Green-Kubo formalism uses the dissipation-fluctuation theorem to calculate the phonon properties, the NEMD model establishes a steady-state heat current and linear temperature profile between a heat source and a heat sink. Recently, another approach using thermal response to temperature difference is proposed. In this model, after a temperature difference is applied, transient to equilibrium temperature is exponential, and the decay time is obtained. The decay time of the temperature difference can be used to calculate the thermal properties of materials. The most significant advantage of this method is that the convergence of temperature difference occurs faster compared to obtaining the stationary regime of the temperature profile, as in the NEMD method, and convergence of HCACF function, as in Green – Kubo method [86, 87]. This allows to investigate much larger structures. By using this method, Lampin et al. [86] modeled a silicon thin film containing 4.5 million atoms. Moreover, Barbarino et al. [88] calculated the thermal conductivity of pristine graphene

monolayers with the size of 100 µm.

The spatial and temporal temperature distribution evolution is calculated from the Fourier law and energy conservation can be obtain from the equation of

$$\frac{\partial T(t,z)}{\partial t} = \alpha \frac{\partial^2 T(t,z)}{\partial t^2} \tag{2.8}$$

where, $\alpha = k/C\rho$ is the thermal diffusivity $(m^2/s)$, $k$ is thermal conductivity $(W/m.K)$, C is the heat capacity $(J/K)$, and $\rho$ is the density $(1/m^3)$. For Equation (2.8), a solution can be obtained by using separation of variables in the form of T(t,z)= $\theta$(t).$\xi$(z). Time-dependent solution is $\theta(t)$=$\theta_0$.exp(-t/$\tau_n$), where $\theta_0$ is the initial temperature difference between hot and cold parts. $\tau_n$ denotes the time decay as

$$\tau_n = \frac{1}{4\phi^2 n^2}\frac{L}{\alpha} = \frac{1}{4\phi^2 n^2}\frac{L}{S}\frac{C_V}{k} \tag{2.9}$$

where $S$ denotes the transverse section with respect to the heat flow direction, while $L$ is the thickness of the domain under investigation [79].

## 2.3. Phonon Density of States and Phonon Dispersion Calculations via Molecular Dynamics

Phonon dispersion is a function that describes the relationship between frequencies and wavevectors. These curves describe the frequency, wavelength, and propagating direction of each phonon in the structure. A number of the phonon modes at any frequency is described as phonon DOS [89]. Both these functions are essential to understand phonon physics and transport. Therefore, an accurate and practical method for these calculations is a necessity for thermal calculations. In addition to the experimental methods like inelastic neutron scattering or electron energy loss spectroscopy, theoretical methods are implemented for these calculations [90]. A direct model based on ab-initio calculations evaluates the dynamical matrix of materials by imposing displacements of atoms [91, 92]. Another ab-initio based model, density

functional perturbation theory (DFPT), uses the linear response theory to obtain the dynamical matrix [93–95]. Despite their high accuracy, both these methods are computationally expensive and mostly prohibitive. Moreover, the direct method requires a large supercell that contains the longest-range interatomic interactions. Another approach is lattice dynamics which calculates the dynamical matrix by using the second derivative of the force fields and then obtains the phonon frequencies by evaluating the eigenvalues of the dynamical matrix. Even though it is an accurate and straightforward method to get the phonon dispersion and DOS, sometimes calculations may become too complicated to derive the Hessian. However, the major disadvantage of these methods is obtaining the dynamical matrix at only zero temperature. Therefore, the anharmonicity of phonons and temperature effect cannot be considered directly. They introduce a quasi-harmonic approach to investigate the temperature effect, which is complicated and sometimes unfeasible [56, 96]. However, MD-based approaches do not suffer from this problem. Therefore, MD is a valuable tool for these calculations.

MD simulations can calculate these functions in two ways: calculating the velocity-velocity autocorrelation function (VACF) and a direct method based on elastic Green's function and fluctuation-dissipation theorem. At each time step in MD simulations, the position and velocity of each atom are calculated. Using trajectory and velocity information obtained from these calculations are used to calculate VACF. Then, phonon DOS can be obtained from the Fourier transform of VACF [97–99] as

$$g(\omega) = \int e^{i\omega t} \frac{\langle v(t)v(0)\rangle}{\langle v(0)v(0)\rangle} dt. \tag{2.10}$$

Despite its straightforwardness to calculate the phonon DOS, phonon dispersion relations cannot be obtained easily. Moreover, considerably large simulation cells, long simulation time, and complicated mathematical operations are needed for accurate results [56].

Another method based on MD simulations constructs the dynamical matrix directly from MD simulations by using the fluctuation-dissipation theorem. For this FixPhonon Command of LAMMPS [100–102] is used. FixPhonon transforms the po-

sition of atoms in real space into reciprocal space to obtain the Green's functions coefficients. After a long enough simulation time, time and ensemble average Green's function coefficients are obtained. A binary log file is obtained from these simulations, consisting of the dynamical matrix [103–105]. After obtaining the dynamical matrix, an auxiliary code, called phana, reads the binary file produced by LAMMPS and calculates the phonon dispersion and DOS. Since q-points are measured directly, tricubic and trilinear interpolation methods can be used to get the q-points [106]. This method is much more straightforward and requires less computational power compared to the VACF method. Therefore, phonon DOS and dispersion calculations in this thesis are calculated through this approach [56, 105].

# 3. THIN FILMS

This chapter will perform thin film thermal conductivity calculations via molecular dynamics to find an accurate and simple method to predict the thin film thermal conductivity from accumulation spectra. Accumulation spectra can be obtained by using experimental and theoretical methods to obtain the thermal conductivities of the thin films. As shown in Figure 3.1, accumulation spectra plot the cumulative thermal conductivity of the phonons in the material with MFPs equal or smaller than a value. Experimental methods such as TDTR [15, 16], BB – TDTR [15, 107], and transient gradient [15] have been used to build accumulation spectra for crystalline semiconductor materials. In contrast, theoretical approaches [5, 14, 19] based on first-principle, empirical, MD methods have also been used for the same purpose. Although the most popular semiconductor is Si [10,108], other semiconductors such as $GaN$ and $AlN$ have also been investigated in these studies [5, 15, 16].

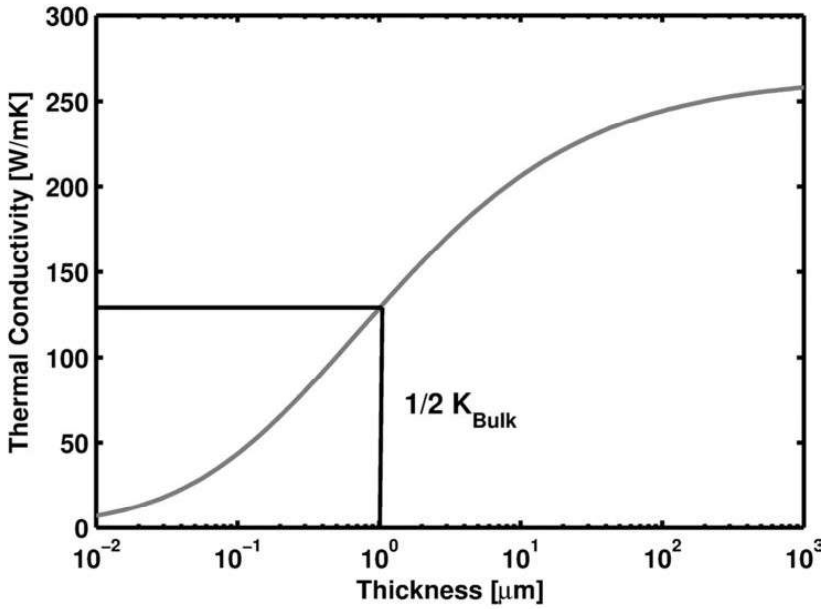



Figure 3.1. Thermal conductivity accumulation spectra for $GaN$. Reprinted from [16], with the permission of AIP Publishing.

There is only one accumulation spectrum for a given bulk material at a specified

temperature, as shown in Fig 3.1. Once obtained, it can be used to predict the thermal conductivity of a nanostructure with varying sizes without any new measurement or simulations requirements. In such studies, thermal conductivities of nanostructures are obtained through the accumulation spectra using certain assumptions, such as phonons with MFPs longer than the film thickness do not contribute to the thermal conductivity. To this date, researchers have not thoroughly studied and understood a proper technique to determine thin film thermal conductivities from thermal conductivity accumulation spectra, called TC-AS [5, 10]. This work aims to obtain such a technique and its applicability conditions with the aid of NEMD simulations. By investigating the thermal transport trends obtained from NEMD and TC-AS, a fitting function is proposed to make the accumulation spectra more accurate, and parameters for this function are defined for $GaN$ and $AlN$ thin films.

To summarize, experimental and theoretical investigation of the semiconductor thin film thermal conductivity characterization presents several difficulties: expensive, occasionally erroneous, computationally expensive, and time-consuming. Instead of directly measuring or calculating the thermal conductivity of thin films, accumulation spectra obtained for the bulk materials can be used with certain assumptions.

## 3.1. Method

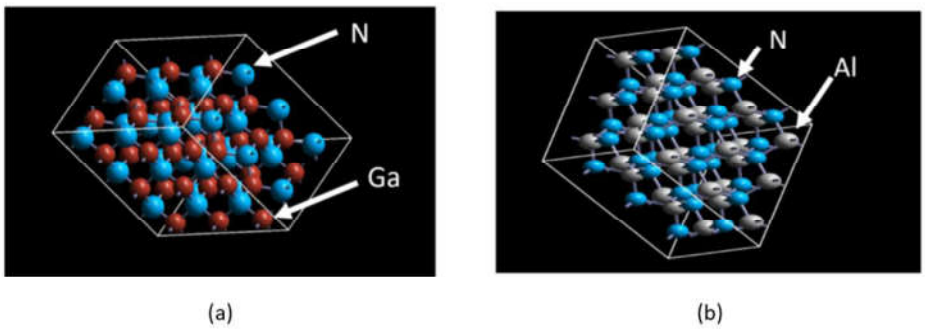



Figure 3.2. Crystal structure of $GaN$ (a) and $AlN$ (b).

Due to their wide use in electronic and optoelectronic applications, $GaN$ and $AlN$ thin films are selected for these simulations. The crystal structures of materials

are presented in Figure 3.2 (a) and (b). NEMD simulations are performed using the LAMMPS. Thermal conductivity calculations for both materials are performed at a temperature, $T$, 300 K, 500 K, and 800 K. Crystal structures of $GaN$ and $AlN$ used in these simulations are shown in Figure 3.2 (a) and (b), respectively. Lattice parameters are a=3.216 $\mathring{A}$ and c=5.240 $\mathring{A}$ for $GaN$, and $a$=3.129 $\mathring{A}$ and $c$=5.017 $\mathring{A}$ for $AlN$. The x, y, and z directions of the NEMD simulation box is aligned with [1100], [1120] and [0001] directions. The orthogonal unit cell has the dimensions of $2a\cos(\phi/6)$, $a$ and $c$ in the x, y, and z directions. Simulation boxes used for these simulations are created by replicating these lattices. An equilibration run before the thermal calculations for each simulation is performed to expand these crystal structures according to the film temperature.

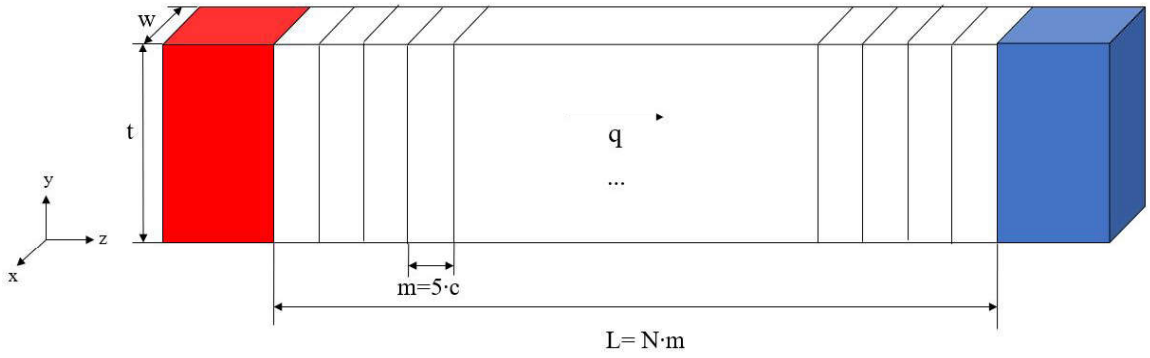



Figure 3.3. NEMD simulation box: the red zone is the heat source, and the blue zone is the heat sink.

Figure 3.3 shows that the simulation box is divided into $N$ number of slabs with the thickness of $m(= 5.c)$ used for both materials to calculate the temperature distribution z-direction and thermal conductivity of the thin film. Here, two constant temperature Langevin thermostats are applied to keep the temperature of hot and cold regions constant in Figure 3.3.

After calculating each atom's velocity, acceleration, and position in slabs, local temperature along z-direction is calculated. However, the obtained temperature distribution is non-linear at the regions near the thermostated regions. Since Fourier's law of conduction requires a linear temperature profile, thermal conductivity calculations

are performed by truncating the regions within a distance, $\sigma^*$, from the thermostats at the boundaries and fitting a linear temperature profile. $\sigma^*/L$, the thickness of truncating region, is taken as 0.10 - 0.20 [109]. The accuracy of NEMD simulations depends on chosen interatomic potentials, thermostats, and boundary conditions applied to the structure. Stillinger-Weber (SW) [110] potentials with parameters developed by Bere and Serra [111, 112] and Vashista et al. [113] are applied for $GaN$ and AlN, respectively. SW potential and these parameters are used in this study since they can successfully describe the interactions between atoms [27, 71, 114]. To model the thermal transport along with thin film successfully, thermostats are installed at the boundaries of the system to keep the temperature constant and create heat flux along with the film. The type and size of the thermostats affect the convergence speed, momentum, and energy conservation. The reflectivity of boundaries is also crucial since phonon-boundary scatterings dominate thermal transport. Improper installation of thermostats and interatomic potentials may cause erroneous results [82]. Therefore, two constant temperature Langevin thermostats are installed since Langevin thermostat is reported as more reliable for thin film thermal conductivity estimations [76]. Even though periodic boundary conditions are applied along x and y directions to represent an infinitely big thin film, simulation boxes' aspect ratio and skewness are kept constant to avoid a numerical error [115]. Since phonon-boundary scatterings are dominated by the surface roughness and the incident phonon frequency, a specularity parameter, $p$, is applied to the system to observe the effect of surface conditions on thermal transport. Here, $p$ is the portion of phonons being specularly reflected. $p = 0$ indicates the purely diffuse scatterings states that the angle of reflected phonon varies over a large range. $p = 1$ shows that the angle of the incident phonon wave is the same as the angle of the reflected wave [116, 117]. To see this effect, various p values are introduced to the fixed boundaries of the simulation box. For building the function, $p = 0.35$ is used since this value produces results more compatible with the experimental studies at low-length scales [16].

Unit cells used to build simulation boxes are formed at $T = 0$ K. Therefore, an equilibration run creates the thermally expanded lattice structures. At first, NPT ensemble is applied to simulation box for equilibration run with a timestep of, $\Delta t =$

1 fs. The total simulation time of equilibration run for each material is $t$ = 1.5 ns at 300 K and is $t$ = 2 ns at 500 K and 800 K. Thermally expanded lattice structure are used for thermal conductivity calculations later. Then, a simulation run for each thin film is performed for $t$=12 ns at 300 K and $t$=20 ns at $T$=500 K and 800 K for $GaN$. Total simulation time for $AlN$ thin films is $t$=15 ns at $T$= 300 K and $t$= 24 ns at $T$= 500 K and 800 K. The thermal conductivity of each film is calculated using the NVE ensemble. The temperature of each slab in the simulation box and temperature distribution along the thin film is obtained after this run. The amount of heat added to and removed from thermostats is also observed. By using these results, the thermal conductivity of $AlN$ and $GaN$ thin films is calculated. Results are presented in the next section.

## 3.2. Results and Discussion

Using the method described above, bulk and thin film thermal conductivities of $GaN$ and $AlN$ at 300 K, 500 K, and 800 K are calculated. Since simulation time may affect the results, simulation should be performed until results are converged. Converged bulk thermal conductivity of $GaN$ is calculated as $k_{bulk}$ = 226.95 ± 1.82 W/m.K, 138.59 ± 1.16 W/m.K, and 88.35 ± 0.79 W/m.K at $T$ = 300 K, 500 K, and 800 K, respectively. For AlN, bulk thermal conductivity at $T$ = 300 K, 500 K, and 800 K are $k_{bulk}$ = 233.54 ± 1.98 W/m.K, 130.36 ± 1.29 W/m.K, and 74.13 ± 0.65 W/m.K. These results are well-matched with reported thermal conductivity values of $AlN$ and $GaN$ results in the literature [5, 18, 118–122].

Moreover, the bulk thermal conductivity of $AlN$ and $GaN$ obtained from NEMD simulations at 300 K are compared with the previous experimental and theoretical studies shown in Table 3.1. Differences between results from this study and experimental studies available in literature may be due to microscopic defects such as impurities and dislocations in samples used in experimental methods, as well as specific measurement errors. On the other hand, bulk theoretical conductivity of $GaN$ obtained via Green – Kubo by Kawamura et al. [123] overestimates the thermal conductivity calculations made via NEMD simulations in this study. The discrepancy between these studies may

Table 3.1. Comparison of the calculated bulk wurtzite $GaN$ and $AlN$ thermal conductivities with data available from literature at 300 K.

| **Reference** | **Sample** | **Method** | **k [W/m.K]** |
|---|---|---|---|
| This study | Wurtzite $GaN$ | NEMD | 226.95 |
| This study | Wurtzite $AlN$ | NEMD | 233.54 |
| Xu et al. [122] | 500 $\mu m$ thick grown by physical vapor transport | $3\omega$ | 237 |
| Shulumba et al. [120] | Wurtzite $AlN$ | Born-Oppenheimer MD | 308.33 |
| Albar and Donmezer [5] | Wurtzite $GaN$ | Ab-initio | 225.94 |
| Kawamura et al. [123] | Wurtzite $GaN$ | Green Kubo | 310 – 380 |
| Slack et al. [121] | 2000 x 300 $\mu$m $GaN$ thin film grown on sapphire substrate by HVPE | | 227 |

be due to statistical errors, as previously discussed by Zhou et al. [71]. Ab-initio based calculations for $AlN$ [124] also overestimate the NEMD results. Shulumba et al. [120] used the phonon BTE and relaxation time approximation for thermal conductivity calculations. This difference may stem from the parameters used in these simulations.

Moreover, the bulk thermal conductivity of $AlN$ and $GaN$ obtained from NEMD simulations at 300 K are compared with the previous experimental and theoretical studies shown in Table 3.1. Differences between results from this study and experimental studies available in literature may be due to microscopic defects such as impurities and dislocations in samples used in experimental methods, as well as specific measurement errors. On the other hand, bulk theoretical conductivity of $GaN$ obtained via Green – Kubo by Kawamura et al. [123] overestimates the thermal conductivity calculations made via NEMD simulations in this study. The discrepancy between these studies may

be due to statistical errors, as previously discussed by Zhou et al. [71]. Ab-initio based calculations for *AlN* [120] also overestimate the NEMD results. This difference may stem from the parameters used in these simulations.

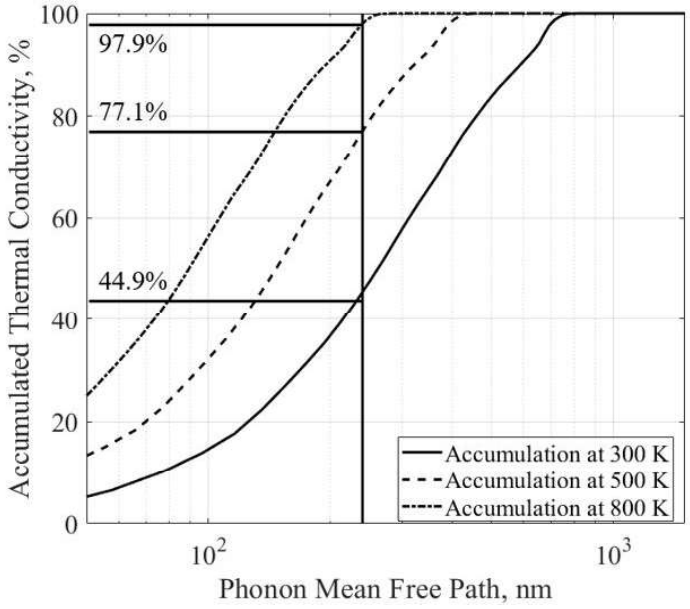



Figure 3.4. Accumulation spectra of wurtzite *GaN* [5] at 300K, 500K, and 800K obtained via ab-initio calculations. Thermal conductivity accumulation for a 240 nm-thick *GaN* film is marked.

Thermal conductivity estimations from accumulation spectra are shown in Figure 3.4 Assuming the material's bulk thermal conductivity is already known, the spectrum is cut at the phonon MFP value equal to film thickness. Then, the obtained percentage is multiplied with the bulk value to obtain the thin film thermal conductivity at that length scale. Figure 3.4 shows that 44.9%, 77.1%, and 97.9% of bulk thermal conductivity are accumulated in a 240 nm-thick thin film at 300 K, 500 K, and 800 K.

The thermal conductivity of GaN (Table 3.2) and AlN thin films (Table 3.3) at three temperatures obtained from TC-AS and NEMD are presented to evaluate the accuracy of the TC-AS model by comparing it with NEMD results. In Table 3.2 and 3.3, the percent difference ($= (k_{MD} - k_{AS}/k_{MD}x100$) of estimation of thin film thermal conductivity from ab-initio studies at all temperatures.

Table 3.2. Comparison of $GaN$ thermal conductivities (W/m.K) obtained from TC-AS and NEMD simulations for selected thin film thicknesses.

| | 300 K | | | | 500 K | | | | 800 K | | | |
|---|---|---|---|---|---|---|---|---|---|---|---|---|
| L(nm) | 50 | 240 | 350 | 450 | 50 | 240 | 350 | 450 | 50 | 240 | 350 | 450 |
| NEMD | 6.02 | 68.3 | 105 | 146 | 11.3 | 79.1 | 105 | 118 | 14.0 | 65.7 | 82.0 | 87.6 |
| TC-AS | 12 | 102 | 142 | 178 | 18.2 | 106 | 127 | 138 | 22.1 | 85.5 | 87.3 | 87.3 |
| Diff.,% | 96.1 | 59.3 | 44.5 | 22.6 | 83.2 | 34.5 | 22.3 | 16.7 | 49.3 | 18.7 | 8.9 | 0.3 |

Table 3.3. Comparison of $AlN$ thermal conductivities (W/m.K) obtained from TC-AS and NEMD simulations for selected thin film thicknesses.

| | 300 K | | | | 500 K | | | | 800 K | | | |
|---|---|---|---|---|---|---|---|---|---|---|---|---|
| L(nm) | 50 | 240 | 350 | 450 | 50 | 240 | 350 | 450 | 50 | 240 | 350 | 450 |
| NEMD | 28.8 | 86.2 | 99 | 123 | 32.4 | 69.2 | 84.9 | 95.9 | 30.8 | 56.9 | 67.4 | 73.9 |
| TC-AS | 54.2 | 127 | 137 | 147 | 58.1 | 91 | 102 | 110 | 45.1 | 66.7 | 72.3 | 74.3 |
| Diff.,% | 88.2 | 47.3 | 38.4 | 19.6 | 79.1 | 31.4 | 20.1 | 14.7 | 46.3 | 17.2 | 7.3 | 0.5 |

As shown in these tables, the difference between models decreases for both materials at longer length scales and higher temperatures. TC-AS spectra can detect the thermal conductivity of thin films larger than 650 nm $GaN$ and 550 nm for $AlN$ with reasonable accuracy at 300 K. At higher temperatures, and the TC-AS model can make reasonably accurate thermal conductivity predictions for the shorter thin films. To improve the accuracy of the TC-AS model, an improved scheme is proposed in this study, as shown in Figure 3.5. The scheme follows four steps: (a) simplifying accumulation spectra, (b) defining the fitting function parameters, (c) obtaining fitting parameters, and (d) validation.

**(a) Simplifying Accumulation Spectra**

Also, relations between maximum phonon MFP – temperature and bulk thermal conductivity – temperature are proposed. The Kn number and accumulated thermal conductivity are calculated using the maximum MFP data at a specific temperature.

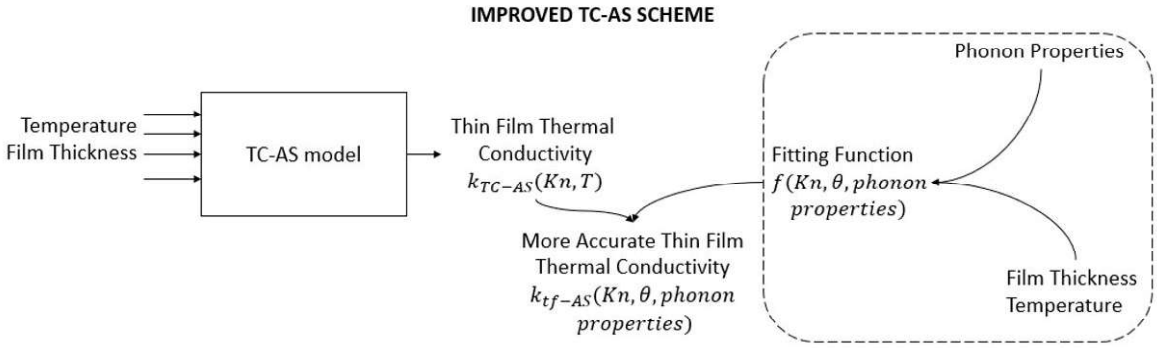



Figure 3.5. Schematics for improved TC-AS model.

To improve the TC-AS model, accumulation spectra are plotted using Kn number, the ratio of the maximum phonon MFP to the film thickness, as shown in Figure 3.6 for $GaN$ and $AlN$. To use these accumulation spectra plots with respect to Kn, bulk thermal conductivity and maximum phonon MFP, $\Lambda$, should at target temperature be known. To do that, relations regarding temperature dependency of bulk thermal conductivity and maximum phonon MFP are proposed for both $GaN$ and $AlN$ from Albar's results [124]. It is observed that bulk thermal conductivity for$GaN$and film temperature has a relation of $k\ \alpha\ T^{-1.15}$ and maximum phonon MFP-temperature relation is $\Lambda\ \alpha\ T^{-1.33}$. Similar relations are also obtained for thermal conductivity, $k\ \alpha\ T^{-1.18}$, and maximum phonon MFP, $\Lambda\ \alpha\ T^{-1.25}$, of AlN.

Figure 3.6 shows that the Kn number – accumulated thermal conductivity plots of $GaN$ and $AlN$ are valid for each temperature value. To use these accumulation spectra for thermal conductivity estimation (TC-AS model), the first $Kn$ number should be calculated using the maximum phonon MFP obtained from earlier relations and film thickness. Then, accumulated thermal conductivity is obtained from the plot. By multiplying it with bulk thermal conductivity of material at the temperature of thin film, thin film thermal conductivity, $k_{TC-AS}$, is calculated. However, this value was obtained from the ab-initio based model. The bulk thermal conductivity of $GaN$ and $AlN$ at 300 K used for these calculations is stated earlier. The maximum phonon MFP, $\lambda_{max}$ of $AlN$ and $GaN$ used in the calculations are 1505 nm and 1661 nm, respectively.

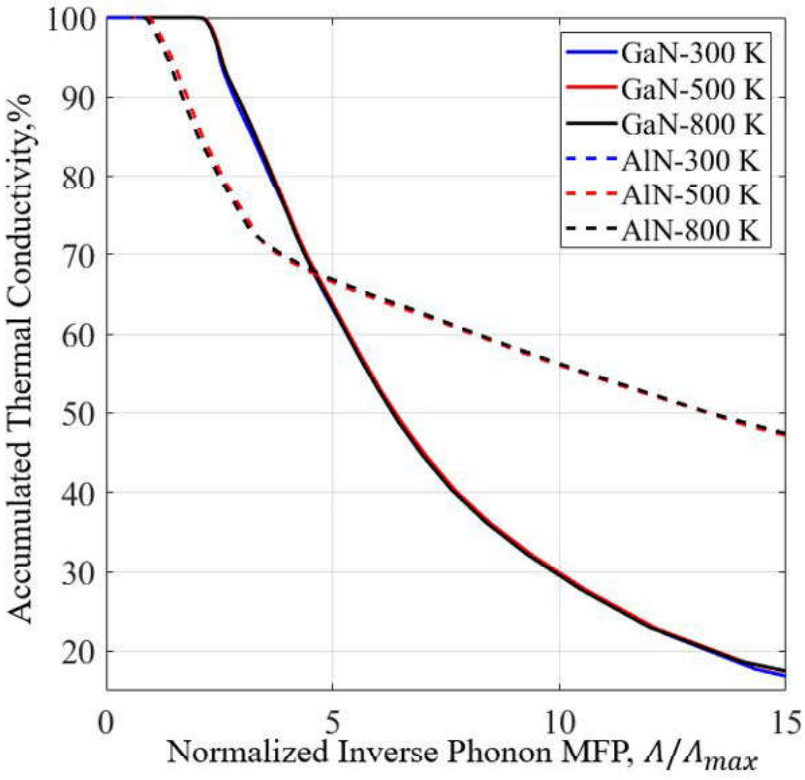



Figure 3.6. Accumulation spectra for$GaN$and $AlN$ thin films with respect to the Kn number.

As stated earlier, ab-initio based models cannot include phonon-boundary scatterings, which dominate thin film thermal transport at smaller scales and colder temperatures. Therefore, these accumulation spectra plots develop a fitting function that includes the phonon anharmonicity and phonon-boundary scatterings. The parameters used for this function are defined in the following section.

### (b) Defining the Fitting Function Parameters

After obtained the accumulated thermal conductivity, a fitting function, $f$, is introduced to improve the accuracy. By multiplying the thermal conductivity from TC-AS and the value from the function, more accurate thin film thermal conductivity, $k_{tf-AS}$, can be obtained. The improved scheme is also shown in Figure 3.5. As discussed earlier, estimations using the TC-AS model deviate more in colder and shorter thin

Table 3.4. Standard atomic weight of atoms formed the materials and molecular mass of $AlN$ and $GaN$ [126].

| Materials | Atom 1 | Atom 2 | m, mass ratio | Molecular mass |
|---|---|---|---|---|
| $AlN$ | 26.981 u (Al) | 14.007 u (N) | 1.926 | 40.988 u |
| $GaN$ | 69.723 u (Ga) | 14.007 u (N) | 4.977 | 83.73 u |

films. Therefore, the function, $f$, should include both the thickness and temperature of thin films. Moreover, phonon properties are also considered for the function. In the end, thermal conductivity obtained from the improved scheme is shown in equation as

$$k_{tf-AS} = f(Kn, \theta, Ph).k_{TC-AS}, \tag{3.1}$$

where $k_{TC-AS}$ is the thermal conductivity obtained from the TC-AS model and $k_{tf-AS}$ is the one from the improved scheme. $f(Kn, T, phonon\ properties)$ is the function that depends on the Kn number and the temperature of the film and some phonon properties. Since deviation between models depends on the temperature and phonon MFP, the fitting function should depend on $\theta$, the ratio of Debye temperature to thin film temperature, and the $Kn$ number. Thermal transport is also affected by phonon properties, which denotes as $Ph$. Here, the group velocity of LA phonon modes, frequency peak of LA modes and other acoustic modes, and total frequency spectrum of acoustic modes are used in attempts of finding such a function. The mass ratio of elements that constitute the material, m, is also considered in this function. Therefore, the fitting function becomes $f = f(Kn, \theta, Ph, m)$. These parameters are used in an algorithm to see a correlation between thermal conductivity accumulation and functions that considers these parameters.

To observe the properties of phonons, phonon dispersion relations of $GaN$ and $AlN$ are plotted as shown in Figure 3.7 (a) and (b), respectively. Red lines show the LA phonon modes, which carry the large portion of the heat carried inside the material. LA phonon modes of $AlN$ are observed at frequency values up to 15 THz, while no

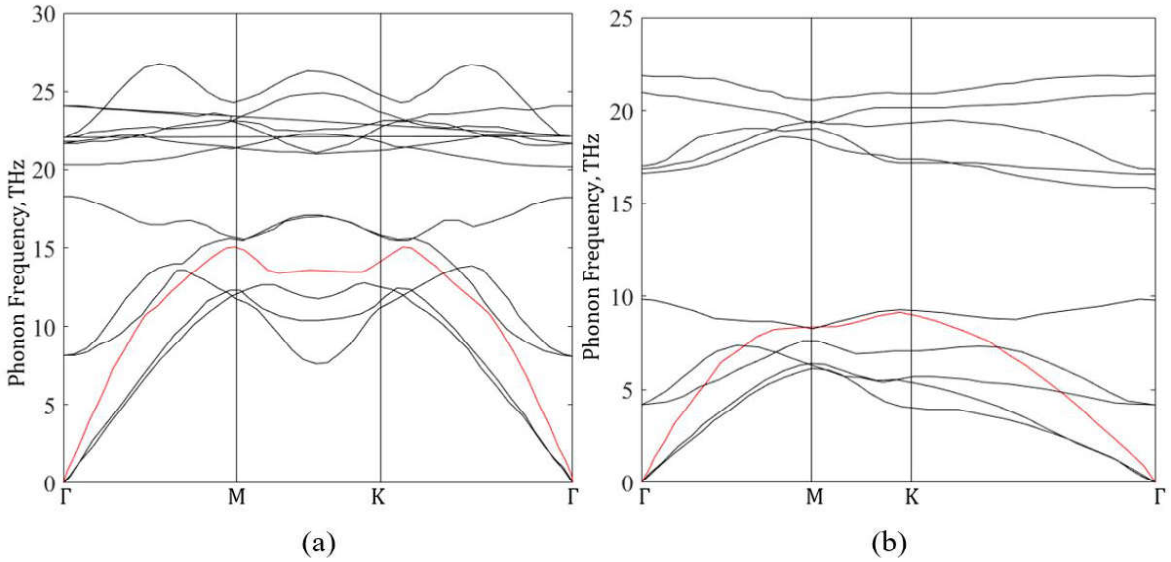



Figure 3.7. Phonon dispersion relations of $AlN$ (a) and $GaN$(b). Red lines show the LA phonon modes of both materials.

LA phonon modes occurred at higher than 8.5 THz. Similarly, the frequency spectrum of $AlN$ ranges between $0 - 28$ THz, while the frequency spectrum of $GaN$ is up to 22 THz. These values indicate different phonon behavior in these materials and are considered for fitting function. Smaller LA bandwidth indicates flatter dispersion and denser low-frequency phonon modes, which carry more energy and are more sensitive to phonon-boundary scatterings. Thus, the ratio of bandwidth LA phonon branches and full phonon spectrum, $BWR_{LA}$, is a good indicator to observe the amount of phonons affected by the phonon-boundary scatterings. Another parameter that affects the phonon scattering mechanisms is the mass ratio of atoms formed in the material.Using the standard atomic weight of materials as presented in Table 3.4, materials' mass ratio ($m = m_A/m_B$) are 1.926 and 4.977 of $AlN$ and $GaN$, respectively. The mass ratio is an essential parameter for phonon transport since a larger mass ratio causes the acoustic phonon modes to be bunched together, increasing their scatterings [125, 126].

### (c) Obtaining Fitting Parameters

Table 3.5. Obtained parameters for Equation 3.2

| Materials | p | q | r | t |
|---|---|---|---|---|
| $GaN$ | -1 | 1 | 1.72 | $\theta_D/T$ |
| $AlN$ | -1 | 1 | 3.54 | $\theta_D/T$ |

By considering the parameters mentioned above, a fitting function is created as

$$f(Kn, \theta, Ph) = exp(-Kn^p \theta^q m^r BWR_{LA}^t). \tag{3.2}$$

To create the function, a curve fitting algorithm is used to calculate the parameters: p, q, r, and t. Applying different values to these numbers and multiplying the function with accumulation spectra obtained via ab-initio calculations, an analytical expression is searched, as presented in Equation 3.2. After a careful investigation, parameters of Equation 3.2 are calculated as shown in Table 3.5. The table shows that the power of Kn and $\theta$ are the same for both materials, while parameters related to phonon properties differ. This shows that the term $Kn^-1.\theta$ can obtain universal accumulation spectra, while phonon properties should be investigated separately.

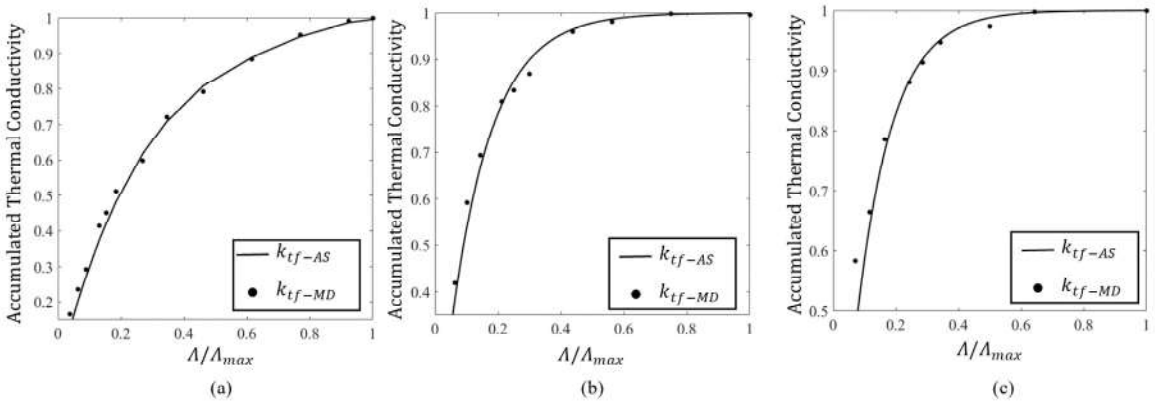



Figure 3.8. Comparison of $k_{tf-AS}$ and $k_{tf-MD}$ for $GaN$ thin films at 300 K (a), 500 K (b), and 800 K (c).

**(d)Validation**

To test the accuracy of fitting function, obtained f values from Equation 3.2 are

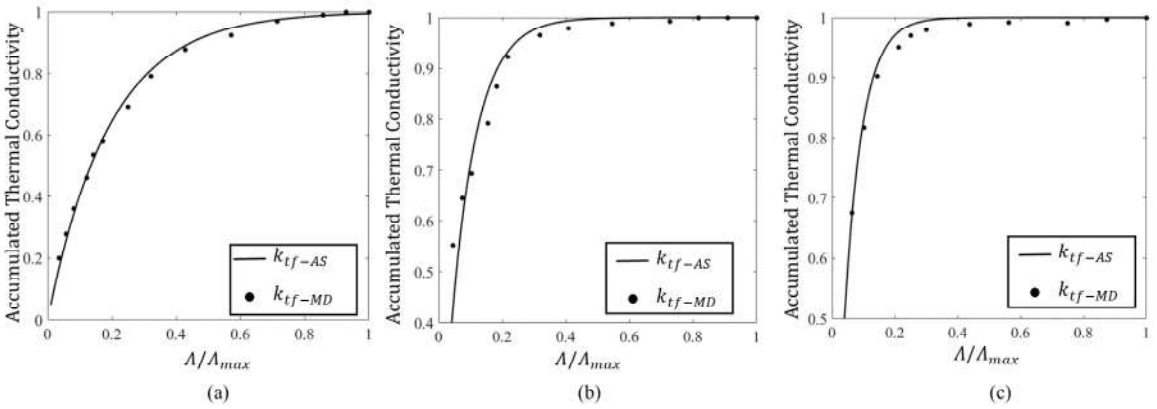



Figure 3.9. Comparison of $k_{tf-AS}$ and $k_{tf-MD}$ for $AlN$ thin films at 300 K (a), 500 K (b), and 800 K (c).

compared with the ones obtained from NEMD simulations, $k_{tf-MD}$. Figure 3.8 (a-c) and 3.9 (a-c) present a comparison between thermal conductivity predictions from MD results and improved TC-AS model at three temperature values for $GaN$ and AlN, respectively. The discrepancy between the $k_{tf-AS}$ and $k_{tf-MD}$ is smaller than 2.3% at each temperature and length scale. Similar to GaN, the discrepancy between $k_{tf-AS}$ and $k_{tf-MD}$ is negligible, 3.1%. These results show that the improved TC-AS model provides reliable results for $AlN$ and $GaN$ thin films.

## 3.3. Conclusion

In this chapter, thermal transport in thin films and their thermal conductivity calculations are investigated. Despite the ongoing experimental and computational efforts, thin film thermal conductivity characterization is still challenging. Dames and Yang [10] claimed the accumulation spectra could be a useful tool to determine the thin film thermal conductivity. Despite its simplicity, the accuracy of this and similar methods has not been studied in detail. This study investigates the accuracy of a thin film thermal conductivity characterization from accumulation spectra and proposes a more accurate alternative to the current techniques.

Results show that the current model can accurately predict the thermal conduc-

tivity of the thick and hot thin films but not short and cold thin films. The difference between the two methods stems from the contribution of phonons longer than the film thickness. Since ab-initio calculations use periodic boundary conditions at each direction, TC-AS model still contains these phonons, while NEMD uses real-size models and therefore phonons longer than film thicknesses cannot be observed; however, TC-AS still contains the effect of longer phonons. Since the phonon MFP spectrum is larger at low temperatures, the discrepancy between models becomes larger.

An improved TC-AS model is proposed to reduce the inaccuracy of TC-AS at low temperature and short length scales. For this improved scheme, accumulation spectra for $GaN$ and $AlN$ are rebuilt with respect to Kn number instead of phonon MFP. Since bulk thermal conductivity and maximum phonon MFP depend on temperature, new relations are proposed to determine these values. Then, a fitting function is proposed, and its parameters are specified. Since the accuracy of TC-AS strictly depends on thickness and temperature, these values are added. To non-dimensionalize these parameters, $Kn$ number and $\theta$, the ratio of Debye temperature to film temperature, are used. Moreover, the mass ratio of atoms is also considered for the function since it affects the acoustic phonon modes, which carry most of the heat. Also, the bandwidth of the LA phonon modes to all phonon spectrum is used in this function since this phonon mode is severely affected by the boundaries.

# 4. INTERFACES WTH 2D MATERIALS

Rapid and continuous shrinking of nanostructures has increased the density of interfaces in semiconductor devices. Interfaces may dominate the thermal transport in materials when the device size is comparable to phonon MFP. Ballistic-diffusive effects on thermal transport, such as interfacial scatterings and ballistic transport, are emerged when interfaces dominate the thermal transport through heterostructures and may change the thermal properties of materials. Changed thermal transport may create additional scattering mechanisms and change the thermal properties of materials. Even though this may lead to reliability and performance issues in devices, it may also control and manipulate the heat flow across the devices. Hence, a rigorous understanding of interfacial thermal transport is necessary for nanodevices [24, 26, 59].

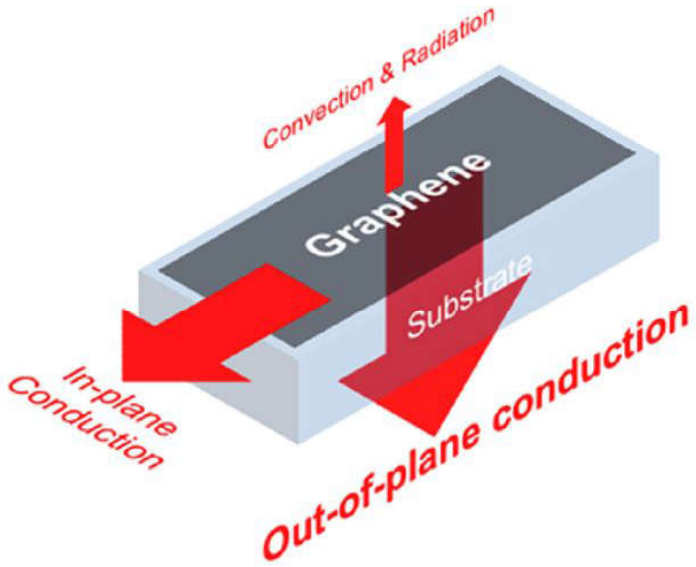



Figure 4.1. Thermal transport schematic for in-plane and out-of (cross)-plane heat conduction in graphene/substrate heterostructure. Heat transfer via convection and radiation is also shown [127]

.

To understand the effect of interfaces on thermal transport, 2D/3D heterostructures have been selected. After the emergence of graphene in 2004, two-dimensional

(2D) materials have drawn tremendous interest for various electronic applications [3, 21, 128]. Despite its thermal and optical properties, the nonexistent band gap of graphene limits its application for next-generation applications [127, 129]. Therefore, other 2D materials with large bandgap and similar properties to graphene-like hexagonal boron nitride ($h-BN$) and transition-metal dichalcogenides (TMDCs: $MoS_2$, $WSe_2$, $WS_2$, etc.) are becoming candidates for high-power applications. Its large bandgap's excellent mechanical and thermal properties make $h-BN$ a prominent material for microelectronic packaging [130], solar cells, and memory devices [21, 54]. On the other hand, some TMDC materials like $MoS_2$ and $WS_2$ are wide bandgap materials with suitable drain current saturation and good thermal conductivity. These materials have potential in field-effect transistors (FETs) [127, 128] and LEDs [131], meanwhile low thermal conductivity material $WSe_2$ is a good candidate for thermoelectric applications.

The schematic of a 2D/3D heterostructure and heat transport in these heterostructures is shown in Figure 4.1. Since they can build weak van-der-Waals (vdW) bonds, 2D materials can be directly grown on many other materials without the lattice match requirement [2, 21]. However, these weak vdW bonds cause poor thermal coupling between the interfaces and slow down the heat transport. The thermal boundary conductance (TBC) at 2D/3D material interfaces is much smaller than their covalently bonded counterparts. Moreover, shrinking size and increasing density of transistors and other circuit devices has increased power dissipation across the whole device. Increased power dissipation and its distribution may lead to the emergence of hot spots – regions with higher temperatures than the device's average temperature. Since high temperatures lead to reliability concerns and faster degradation of the devices, thermal management strategies and electronic packaging applications should be made by considering these regions [2]. Since heat dissipation from the localized heating regions in 2D devices depends on this TBC and individual in-plane thermal conductivity of material layers in the heterostructures, understanding and enhancing the thermal transport rates in 2D/3D heterostructures in devices is critically important for their efficient thermal management. Moreover, it is known that individual thermal conductivities are also affected by choice of materials in the heterostructure due to short-range atomic inter-

actions [54]. Better thermal management alternatives can be designed, and/or proper selection of the substrates will be possible only if the overall thermal performance of 2D/3D heterostructures is known [132, 133].

In this chapter, the TBC and in-plane thermal conductivity of 2D/3D heterostructures are investigated by using two MD approaches: AEMD and NEMD. Moreover, phonon properties of materials are also obtained by using MD based model. Four 2D materials ($h-BN$, $MoS_2$, $WS_2$, and $WSe_2$), which have unique properties and potential use in future applications, are used for simulations. As 3D materials, wurtzite $GaN$ and amorphous $SiO_2$ are selected since $GaN$ has excellent thermal properties and is widely used in electronic applications, and $SiO_2$ is used as substrate materials in many applications. Relations between phonon properties of materials and thermal transport in heterostructures are also investigated.

## 4.1. Method

In these simulations, TBC at interfaces of van der Waals heterostructures, $G$, and in-plane thermal conductivity of materials formed the interface are investigated using two different MD schemes. AEMD model is used to calculate the TBC of heterostructures between four 2D materials and two substrate materials. In-plane thermal conductivity of materials in heterostructures and isolated materials is obtained by using NEMD simulations. Phonon properties are calculated using the fluctuation-dissipation theorem and Green's functions as discussed in Ch. 1 earlier to understand the in-plane and cross-plane thermal transport in heterostructures.

To create the simulation boxes for crystalline materials used in these simulations, lattice parameters in Table 4.1 are used. The structure of amorphous $SiO_2$ is created by using the computational procedure suggested in [134]. AEMD simulation uses time decay, $\tau_n$, of temperature difference between two thermostats, $\Delta T$, for thermal calculations. Figure 4.2. shows the simulation domain used in AEMD simulations.

During the simulation, the temperature difference between thermostats along the

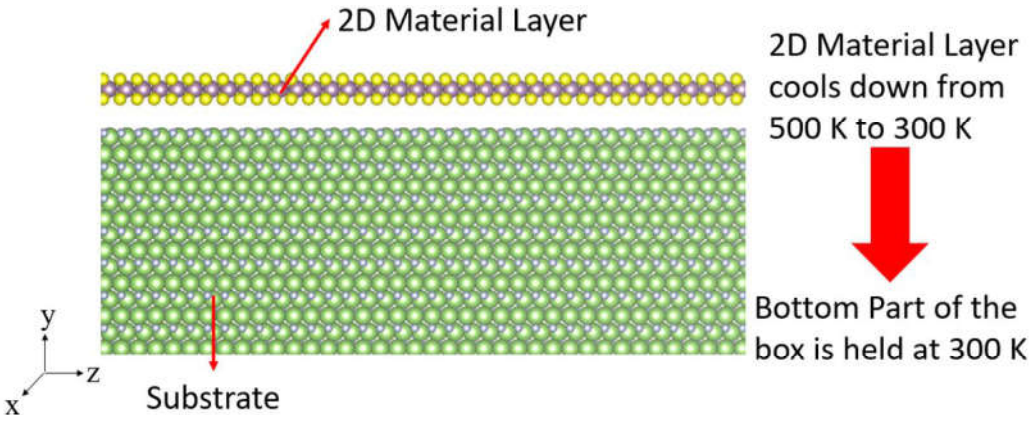



Figure 4.2. Simulation box used for AEMD simulations.

Table 4.1. Lattice parameters (a=b) of crystalline 2D materials and $GaN$.

| Materials | Lattice Parameters (a=b) |
|---|---|
| $GaN$ | 3.216 $\mathring{A}$ |
| $MoS_2$ | 3.190 $\mathring{A}$ |
| $WS_2$ | 3.191 $\mathring{A}$ |
| $WSe_2$ | 3.327 $\mathring{A}$ |
| $h-BN$ | 2.512 $\mathring{A}$ |

simulation time is observed. To model the interactions between atoms accurately, interatomic potentials SW [110] with parameters of Béré and Serra [111,112], Jiang et al. [135], and Mobaraki et al. [70], for $GaN$, $MoS2$, $WS_2/WSe_2$, respectively. Tersoff potentials [136–138] with parameters of Munetoh et al. [139] for $SiO_2$ and extended Tersoff potentials with parameters of Los et al. [140] are preferred for $h-BN$. Non-bonding interactions between 2D material layers and substrates are used 12-6 Lennard Jones (LJ) potential given as

$$V(r) = 4\chi\epsilon[(\sigma/r)^{12} - (\sigma/r)^{6}], \tag{4.1}$$

where $\chi$ is the interaction strength, $\epsilon$ is the energy parameter, $\sigma$ is the distance parameter, and $r$ is the interatomic distance. Parameters of LJ potentials are calculated

by applying the mixing rules to Universal Force Field (UFF) parameters [141]. Interaction strength, $\chi$, is chosen as 2. Two Langevin thermostats are applied, as shown in Figure 4.2. A temperature difference of 200 K between two materials by using these thermostats.

At first, an equilibration run at NVT ensemble with a timestep of, $\Delta$t, 0.5 fs for $t$ = 2 ns allows these structures to reach equilibrium and create thermally expanded lattices. Then, the NVE ensemble is applied to the top part of the simulation box with $\Delta$t = 0.25 fs, and simulations are performed until the temperature difference between thermostats converges to zero. NVT ensemble is applied to the bottom part of the box. Therefore, the temperature of the bottom part is kept constant at $T$=300 K. Temperature of the top part of the simulation box is $T$=500 K at the beginning of the simulation, and its temperature converges to the substrate temperature. Time step is reduced to capture the high-frequency phonons. Mixing rules cannot accurately take the polarization of two different atoms in contact; the interactions between materials in heterostructure can be stronger than predicted by the UFF model [27, 79, 142].

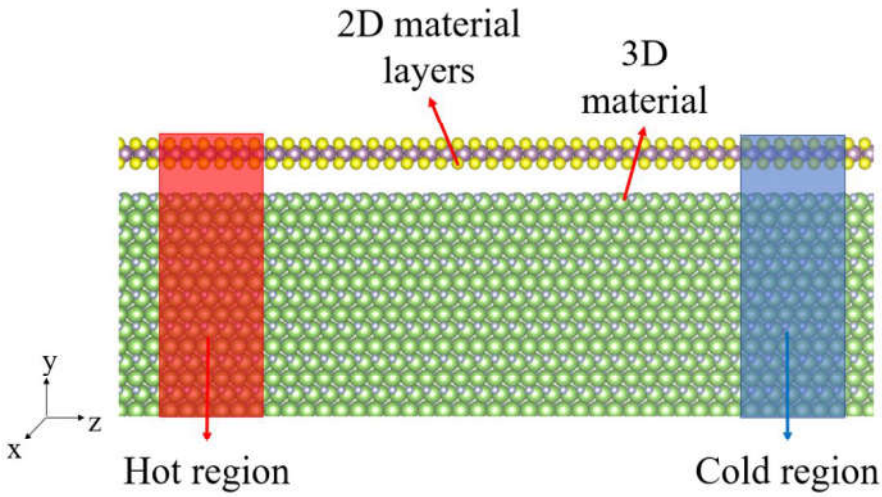



Figure 4.3. Simulation box used for NEMD simulations.

For in-plane thermal conductivity of materials in heterostructures, the used simulation box shown in Figure 4.3 is shown. Here, two thermostats are applied near boundaries to create heat flux. The periodic boundary condition is applied to all sim-

ulation box boundaries to eliminate the thermal size effects. The same interatomic potentials and parameters are used for the NEMD simulations. First, an equilibration run at the NVT ensemble is performed for each material and material pair. Specularity parameter, $p$, is not applied since all interfaces and boundaries are assumed to be perfect. After an equilibrated structure at $T$=300 K is obtained, the in-plane thermal conductivities of materials are calculated using $\Delta t$=0.25 fs. Heat fluxes and temperature distribution along the in-plane direction are used to obtain the thermal conductivity. The same computational procedure is applied to obtain the in-plane thermal conductivity of isolated materials by only using one material in the simulation box.

Finally to relate the phonon properties of materials to in-plane and cross-plane thermal transport in heterostructures, phonon frequencies, wavevectors, and phonon density of states (PDOS) are obtained from MD simulations and the FixPhonon command [56] of LAMMPS that constructs the dynamical matrix of materials by using the fluctuation-dissipation theorem and coefficient of elastic Green's equations. The dynamical matrix is saved in a binary file. Then, an auxiliary code, phana, reads the binary file and calculates the eigenvalues of the dynamical matrix to obtain the phonon dispersion and PDOS of materials. For these simulations, a simulation box contains 13x13x13 primitive cells of substrate materials and 13x13x1 primitive cells of 2D materials. A time step, *Deltat*, of 1 fs is used. The system is equilibrated for $t$ = 0.5 ns, and then simulations are performed for $t$ = 12 ns. Trilinear interpolation is used to create the wavevectors [56, 143].

## 4.2. Results and Discussion

In this part, TBC of heterostructures and in-plane thermal conductivity of materials in these structures are presented. Moreover, the effect of a couple of parameters (PDOS mismatch, lattice mismatch, number of layers) on cross thermal transport between materials and TBC is also investigated. To understand the effect of interfaces and altered phonon mechanisms, the in-plane thermal conductivity of isolated materials is also presented to use as a comparison with results in heterostructures.

Table 4.2. TBC ($G$) values and average time delay ($\tau_n$) at the 2D/3D material interfaces.

| | $GaN$ | | $SiO_2$ | |
|---|---|---|---|---|
| | $G(MW/m^2K)$ | $\tau_n(ps)$ | $G(MW/m^2K)$ | $\tau_n(ps)$ |
| $MoS_2$ | 7.4±0.21 | 732 | 26.8±0.31 | 341 |
| $WS_2$ | 9.3±0.28 | 541 | 31.8±0.35 | 332 |
| $WSe_2$ | 6.2±0.18 | 32 | 21.3±0.29 | 382 |
| $h-BN$ | 12.8±0.29 | 410 | 43.6±0.3 | 236 |

### 4.2.1. Thermal Boundary Conductance

Table 4.2 presents the TBC, $G$, and the temperature decay time, $\tau_n$, for eight different vans der Waals heterostructures formed by 2D materials ($h-BN$, $MoS_2$, $WS_2$, and $WSe_2$) and 3D substrates ($GaN$ and $SiO_2$). TBC values varies between 6.2 – 12.8 $MW/m^2K$ for $2D/GaN$ and 21.3 – 43.6 $MW/m^2K$ for $2D/SiO_2$ interfaces. TBC of $2D/SiO_2$ interfaces is higher than TBC of $2D/GaN$ interfaces. Among the 2D materials, $h-BN$ interfaces have the highest TBC, while $WSe_2$ interfaces have much lower TBC compared to the other heterostructures investigated here. In this chapter, the effect of lattice mismatch between adjacent materials and phonon properties of materials. Also, TBC of $2D/GaN$ heterostructures by the increasing number of 2D material layers is investigated to understand its effect on cross-plane thermal transport. The factors affecting the TBC are listed as:

**Lattice Mismatch:** Lattice mismatch causes lower adhesion energy between layers, leading to a poor thermal coupling between materials. Moreover, lattice mismatch causes higher atomic disorder at the interface. Higher atomic disorder and low adhesion energy reduce the phonon transmission between layers and slow down the cross-plane thermal transport at the interface. The lattice mismatch between materials is only computed for crystal materials. The lattice mismatch between $TMDC/GaN$ heterostructures are close to each other and ranges between 3.2 – 3.5%, while the highest mismatch among TMDC is observed in $WSe_2/GaN$ (3.5%), and the lowest mismatch

is observed in $WS_2/GaN$ (3.21%). The interface with the largest lattice mismatch, $WSe_2/GaN$, has less TBC than slightly less mismatched interfaces, while $WS_2/GaN$ has the lowest lattice mismatch and the highest TBC between $TMDC/GaN$ heterostructures. Although the lattice mismatch of $h-BN$ /GaN is slightly higher at 21%, the TBC of this structure is much higher than others. Hence, despite its importance for cross-plane thermal transport and TBC at the interface, lattice mismatch only provides information about the trend in TBC; however, it cannot describe the phonon transport at interfaces in detail.

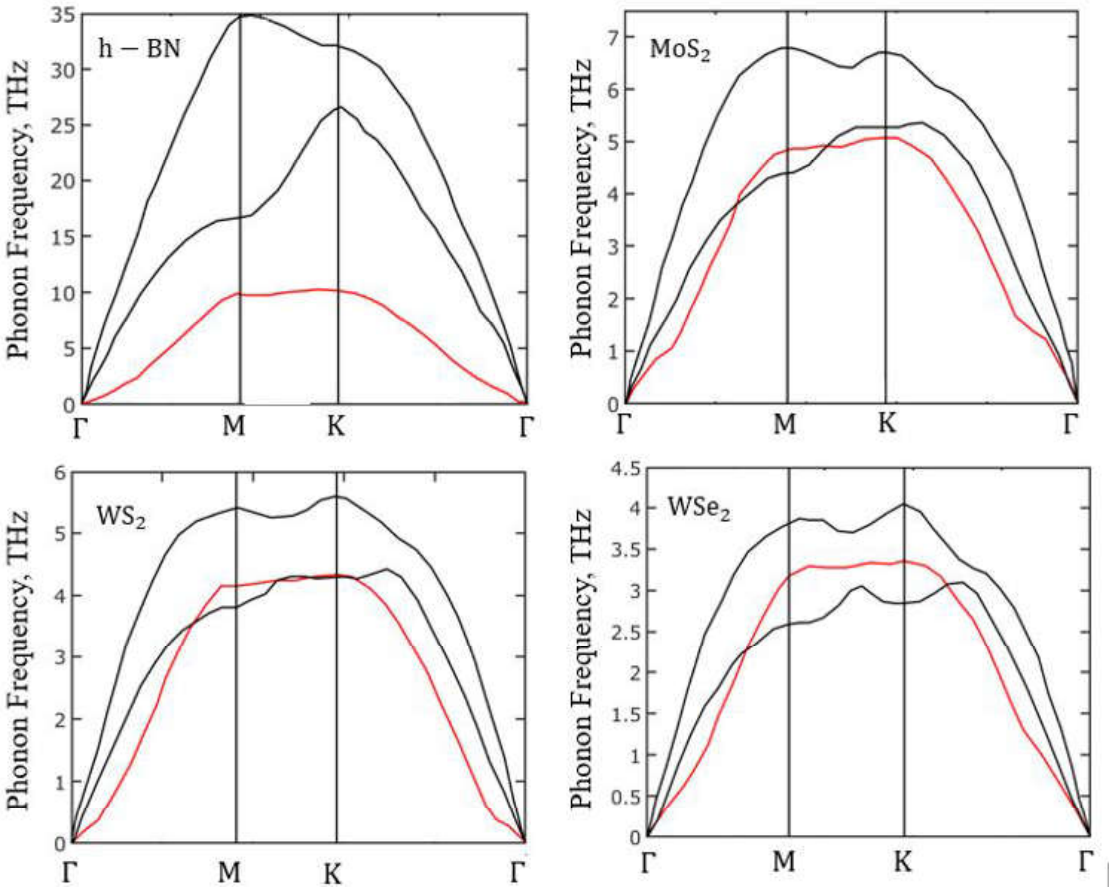



Figure 4.4. Phonon dispersion of acoustic phonon modes of $h-BN$, $MoS_2$, $WS_2$, and $WSe_2$. ZA phonon modes are painted red.

**Phonon Dispersion and Density of States (PDOS):** Phonon coupling and transmission rates at the interfaces strongly depend on the phonon density of states of materials forming the interface [21, 27]. Specifically, PDOS of low-frequency ZA phonons gives valuable information about TBC between 2D and 3D materials since they

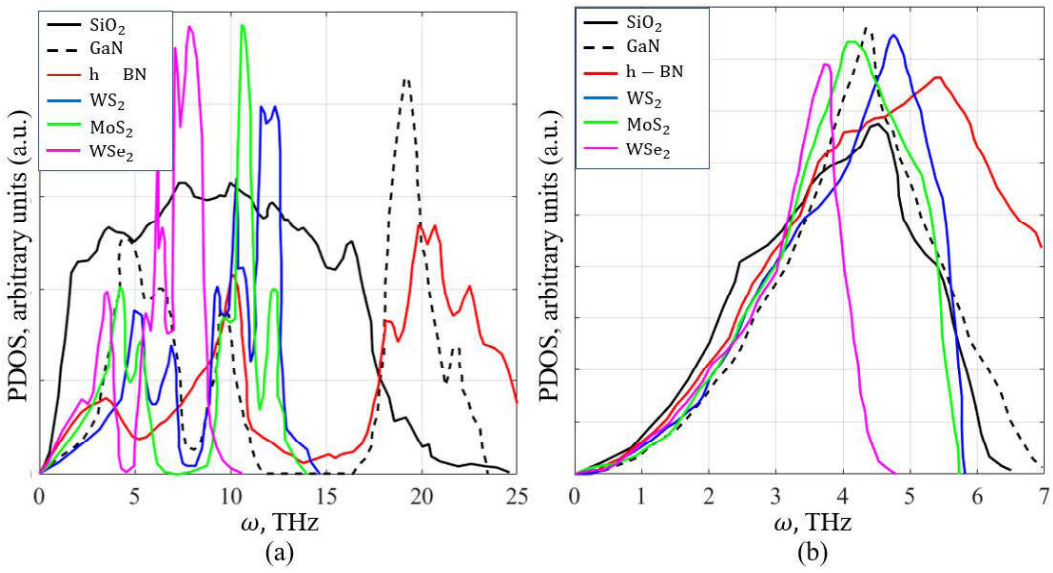



Figure 4.5. DOS of all (a) and ZA phonon modes (0-7 THz) (b) of materials used in the study.

are primarily responsible for cross-plane thermal transport [23,30]. Figure 4.4. (a)-(d) show the acoustic phonon dispersion of 2D materials used in this study. According to these figures, the frequency range of ZA modes varies between 0 – 4.63 THz, 0 – 5.41 THz, and 0 – 5.71 THz for monolayer $WSe_2$, $MoS_2$, and $WS_2$, respectively. In monolayer $h-BN$, ZA phonon mode frequencies vary between 0 – 10.4 THz. These studies are compatible with various theoretical and experimental studies in the literature [27, 54, 144, 145].

Hexagonal boron nitride has more phonon modes in the ZA phonon frequency range which means it has more phonons to carry the heat to other materials. Similarly, $SiO_2$ has more low-frequency phonon modes compared to the $GaN$. Due to its low-frequency peak in PDOS occurred around 2 THz, as shown in Figure 4.5 (a), amorphous $SiO_2$ has a much higher substrate scattering rate, $\Gamma_s$ $\alpha$ $DOS(\omega)/\omega^2$, and hereby more ZA phonon modes contribute to TBC of $2D/SiO_2$ interfaces [23] which are higher than those of $2D/GaN$ heterostructures. Moreover, in $2D/SiO_2$ heterostructures, flexural phonon modes are more matched to each other, which causes a significant increase in TBC at these interfaces. PDOS mismatch between layers is quantified at these

Table 4.3. Phonon DOS mismatch in the range of $0-5$ THz and $G$ values of interfaces.

| Interface | $\Delta DOS_{ZA}$ | $G(MW/m^2.K)$ |
|---|---|---|
| $WSe_2$–$GaN$ | 42.6% | 6.2 |
| $MoS_2$–$GaN$ | 29.8% | 7.4 |
| $WS_2$–$GaN$ | 26.4% | 9.3 |
| $h-BN$–$GaN$ | 22.8% | 12.8 |
| $WSe_2$–$SiO_2$ | 37.6% | 21.3 |
| $MoS_2$–$SiO_2$ | 23.9% | 26.8 |
| $WS_2$–$SiO_2$ | 20.1% | 31.8 |
| $h-BN$–$SiO_2$ | 18.9% | 43.6 |

frequency ranges as

$$\Delta DOS_{ZA} = \int_0^{5THz} \frac{\sqrt{(DOS_{ZA,2D}(\omega) - DOS_{ZA,3D(\omega)})^2}}{DOS_{ZA,3D}(\omega)}\, d\omega, \tag{4.2}$$

where $DOS_{2D}(\omega)$ and $DOS_{3D}(\omega)$ denote the phonon DOS of phonon modes of the 2D and substrate materials. The integral is taken between 0 to 5 THz to represent low-frequency phonons, 5 THz is chosen since no ZA phonons are observed in TMDC materials above this frequency. In Table 4.3, we present the PDOS mismatch calculated using Equation (4.2). Here a direct quantitative relation between PDOS mismatch of ZA phonons, $\Delta DOS_{ZA}$ and TBC, $G$, was observed since lower PDOS mismatch cause higher TBC in materials. Between TMDC materials ($MoS_2, WS_2, WSe_2$), the highest $G$ values are calculated for $WS_2/GaN$ interfaces with the lowest $\Delta DOS_{ZA}$. The largest $G$ is observed for $h-BN$ interfaces due to its smaller $\Delta DOS_{ZA}$ with $GaN$ and $SiO_2$.

As stated earlier, new ZA phonon modes are created in $2D/SiO_2$ heterostructures. Figure 4.6 shows that phonon dispersion relation in the heterostructure approaches to phonon dispersion of 3D substrate material. In $2D/SiO_2$ heterostructures, ZA phonon modes are observed at larger frequencies than the $2D/GaN$. Moreover, PDOS relations show that the low-frequency peak observed in isolated $SiO_2$ happens for its

heterostructures. The low-frequency peak at $h-BN/SiO_2$, which has the highest TBC, is observed at a lower frequency when compared to other structures. Similarly, $h-BN/GaN$ structure also has a low-frequency peak. However, this peak has a higher frequency and lower PDOS values than $2D/SiO_2$ heterostructures.

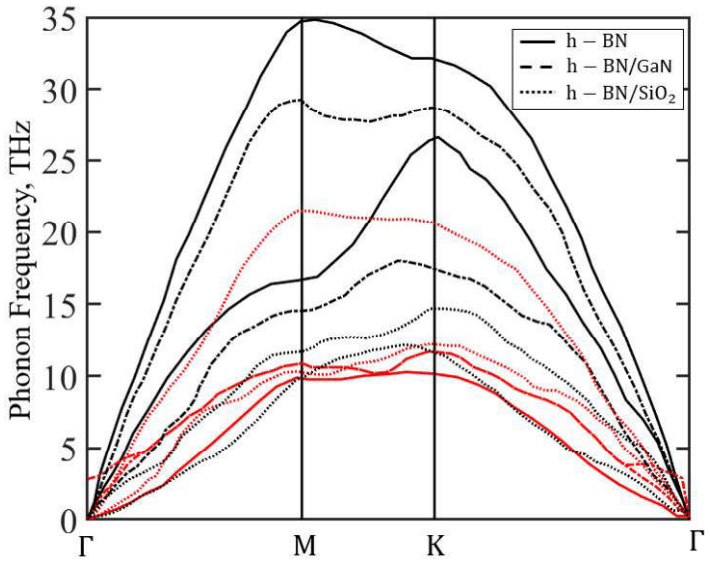



Figure 4.6. Phonon dispersion of acoustic phonon modes of $h-BN$, $h-BN/GaN$, and $h-BN/SiO_2$ of ZA phonon modes are painted red.

In summary, phonon-related properties are much inclusive to understand the TBC in detail. PDOS match, PDOS of ZA modes, low-frequency peak, change in PDOS, and phonon dispersions should be considered together to have a large TBC interface. $SiO_2$ has a much larger low-frequency peak at a lower frequency, and therefore, more phonon scatterings between materials occur. Moreover, it is more PDOS match with 2D materials, and new ZA phonon modes emerge in its heterostructures. Therefore, more heat can move into other materials in $2D/SiO_2$ structures. On the other hand, $h-BN$ has a larger PDOS and higher PDOS match with $GaN$ and $SiO_2$ than the other 2D materials.

**Number of Layers:** Besides the lattice mismatch and phonon properties, TBC at interfaces also depends on the number of the 2D material layer. Previous studies on $2D/SiO_2$ heterostructures showed a significant increase in TBC with the increasing

number of 2D material layers [27]. This effect has not been investigated for $2D/GaN$ heterostructures. Thus, in Figure 4.7, the TBC change in $2D/GaN$ heterostructures when the number of 2D material changes from 1 to 4 is presented. The increasing number of layers causes more adhesion energy at the interfaces between 2D/3D materials and additional flexural phonon branch formation. However, it may also cause more interlayer resistance between layers. TBC of $2D/GaN$ interfaces converges to a constant value after 4-layers, according to Figure 4.7.

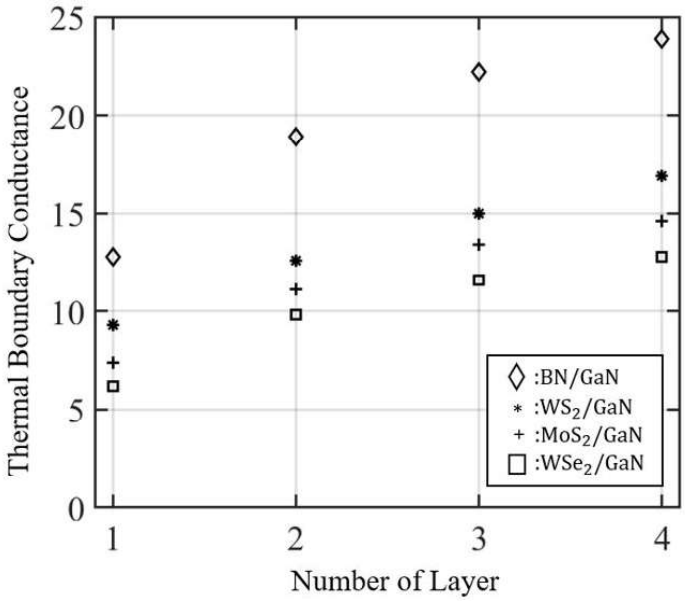



Figure 4.7. $TBC(MW/m^2K)$ of 1-4 layers $2D/GaN$ heterostructures.

After investigating the effect of different material properties linear relation is observed between TBC, $G$, and an interface variable, $I$ which given in

$$I = exp(-(M_{2D}P_{inter})^{1/2}(n\theta_{2D}BWR_{ZA})^{1/3}). \tag{4.3}$$

This interface variable depends on the Debye temperature ($\theta_D$) to the structure's temperature, $T$,ratio of materials, $\theta$ (=$\theta_D/T$), that formed the interfaces and PDOS match between materials in contact, $P_{inter}$, is considered. Moreover, since ZA phonons are responsible for cross-plane thermal transport, the mass ratio of atoms in 2D materials, $M_{2D}$, and the ratio of ZA phonon bandwidths of materials, $BWR_{ZA}$, number of 2D

material layers, $n$, is analyzed and the expression is given as

$$G = A * I + B. \tag{4.4}$$

With this expression, material properties and TBC values of 2D/3D interfaces investigated in this study are mapped, as shown in Figure 4.8. Even though TBC of $2D/SiO_2$ interfaces are significantly higher than $2D/GaN$, I values are similar to each other.

Figure 4.8 (a) and (b) shows that linear dependence between $I$ and TBC, $G$, values of each material. Hence, a fitting function is proposed for TBC estimation as shown in Equation (4.4). Here, A and B are constant parameters for each substrate material. These parameters are obtained by fitting the $G$ results of $GaN$ and $SiO_2$ interfaces. Fitted expression can predict the TBC of interfaces in an error margin of 6%.

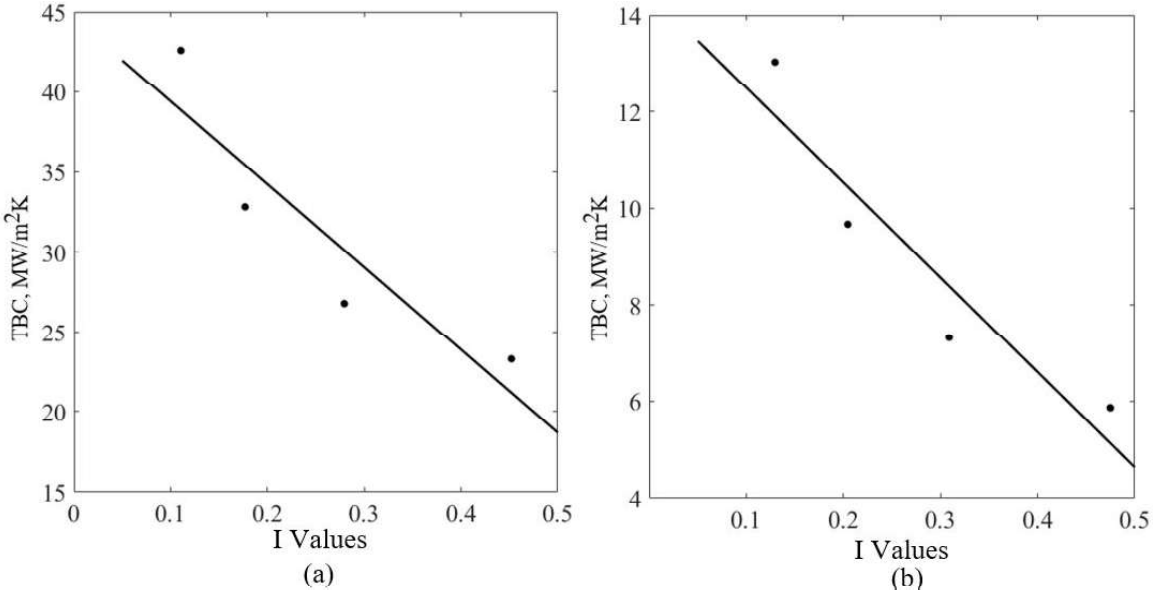



Figure 4.8. $G$ $(MW/m^2K)$ of 1-4 layers $2D/GaN$ heterostructures.

A and B parameters is obtained by fitting $I$ and $G$ values as shown in Figure 4.10 (a) and (b) for $2D/GaN$ and $2D/SiO_2$ interfaces, respectively. In Figure 4.9, a comparison between our model and literature is given. This figure shows that TBC estimations based on Equation (4.3) are well matched with the experimental [58] and

Table 4.4. Parameters obtained for Equation (4.3).

| | A | B |
|---|---|---|
| $2D - SiO_2$ | -22.59 | 15.21 |
| $2D - GaN$ | -63.17 | 47.294 |

theoretical studies [21,27] in the literature. These figures show the trends between $G$ of heterostructure and phonon properties of materials in contact at these interfaces. The obtained $A$ and $B$ parameters for these interfaces are given in Table 4.4. The differences between A and B parameters of materials are also depends on the $G$ of interfaces, thereby, they depends on the material properties investigated in this chapter. More investigation is necessary to form a relation.

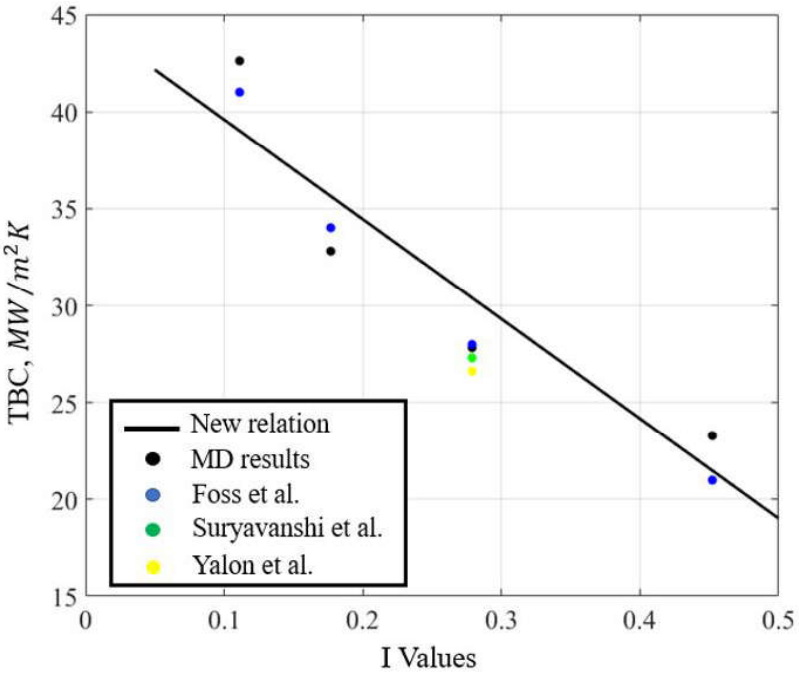



Figure 4.9. Comparison between Equation (4.3), MD results, and literature.

### 4.2.2. Thermal Conductivity of the Heterostructures

Although TBC is essential for the thermal performance of devices, the thermal conductivity of the individual materials in heterostructure is also significant to com-

ment on the heat spreading performance of the devices. In this section, the in-plane thermal conductivity of materials in heterostructures is investigated, and results are compared to the in-plane thermal conductivity of isolated materials to understand the effect of interfaces on in-plane thermal transport [146].

NEMD simulations predict the thermal conductivity of bulk, $k_{bulk}$ $GaN$ and $SiO_2$ as 226.95 W/m.K and 1.38 W/m.K, respectively. These values are consistent with the previous studies available in the literature [5, 15, 81]. Table 4.5 shows the thermal conductivity of 2D materials and substrate materials (isolated or in heterostructures). In-plane thermal conductivity changes of a substrate are only reported for a tiny region next to the interface since the bulk thermal conductivity of 3D materials does not change in heterostructures. Therefore, thermal conductivity is only described for the affected area. The thickness, $L_{aff}$, of this ranges from 40 nm to 75 nm, based on the materials. The affected area of $SiO_2$ in $h-BN/SiO_2$ heterostructure is the largest, while $WSe_2$ has the smallest impact among all 2D materials on the substrate. The size of the affected area is increased by the change in in-plane thermal conductivity and higher TBC.

According to Table 4.5, the thermal conductivity of 2D materials drops by increasing the number of layers where they are isolated or in heterostructures. In monolayers, phonons can travel longer distances and carry more energy since interlayer phonon – phonon interactions are absent in these structures. Table 4.5 also displays the individual thermal conductivities of layers in heterostructures. Since the thermal conductivity of amorphous $SiO_2$ is lower than $GaN$ and all 2D materials, it reduces the thermal conductivity of the 2D material used within the heterostructure. However, when $2D/GaN$ heterostructures display a different trend. Since $GaN$ has a higher thermal conductivity than the TMDC materials, it improves the thermal transport properties of the 2D materials placed on them and increases their thermal conductivities [54, 147].

Nevertheless, this effect also causes a reduction in the thermal conductivity of the $GaN$ layers near the interface. For the $h-BN$ /GaN interface opposite of this interaction occurs. Since the thermal conductivity of $h-BN$ is greater than $GaN$, it

Table 4.5. Individual in-plane thermal conductivity (W/m.K) of 1 (1L), 2 (2L), and 3 (3L) layered 2D materials (isolated and in heterostructure) and their substrates.

| | | Isolated | $2D/GaN$ | | $2D/SiO_2$ | |
|---|---|---|---|---|---|---|
| | | | 2D | $GaN$ | 2D | $SiO_2$ |
| $h-BN$ | 1L | 461 | 326 | 251 | 143 | 3.1 |
| | 2L | 443 | 318 | 244 | 136 | 3.06 |
| | 3L | 432 | 314 | 239 | 131 | 3.01 |
| $MoS_2$ | 1L | 24.3 | 28.7 | 101 | 8.9 | 1.97 |
| | 2L | 21.1 | 24.3 | 95.7 | 8.1 | 1.81 |
| | 3L | 19.5 | 23.2 | 92.8 | 7.1 | 1.72 |
| $WS_2$ | 1L | 51.5 | 59.7 | 134 | 16.8 | 2.01 |
| | 2L | 43.1 | 48.3 | 121 | 14.6 | 1.88 |
| | 3L | 36.2 | 41.2 | 115 | 9.1 | 1.76 |
| $WSe_2$ | 1L | 7.01 | 8.62 | 82.1 | 3.76 | 1.44 |
| | 2L | 6.22 | 6.92 | 74.2 | 3.38 | 1.42 |
| | 3L | 5.45 | 6.09 | 70.1 | 3.01 | 1.41 |

decreases when in close contact with $GaN$. For monolayer $h-BN/GaN$ structure, 30% reduction of $h-BN$ in-plane thermal conductivity reduction is observed. While this is happening, the in-plane thermal conductivity of the top layers of $GaN$ increases by almost 11

The change in thermal conductivity of these structures is caused by changing phonon mechanisms in heterostructures. The phonon dispersion relation shown in Figure 4.10 shows that ZA phonon modes and LA phonon modes of $GaN$ and $MoS_2$, which are responsible for most of the in-plane thermal conductivity, are changed. In 2D/3D heterostructures, phonon dispersion relations for all phonon modes become similar to phonon dispersion, as shown in Figure 4.10. Moreover, the PDOS of heterostructures differs from the PDOS of materials that constitutes the interface. Interfaces under investigation in this study are formed with weak vdW bonds between materials. These bonds cause two different phonon mechanisms to interact with each other and change.

Changed phonon transport mechanism causes different scattering rates, group velocity, and phonon MFP; consequently, it changes the in-plane thermal conductivity of materials in contact. Therefore, it can be concluded that in-plane thermal transport is also affected by the presence of the interface [22, 146–148].

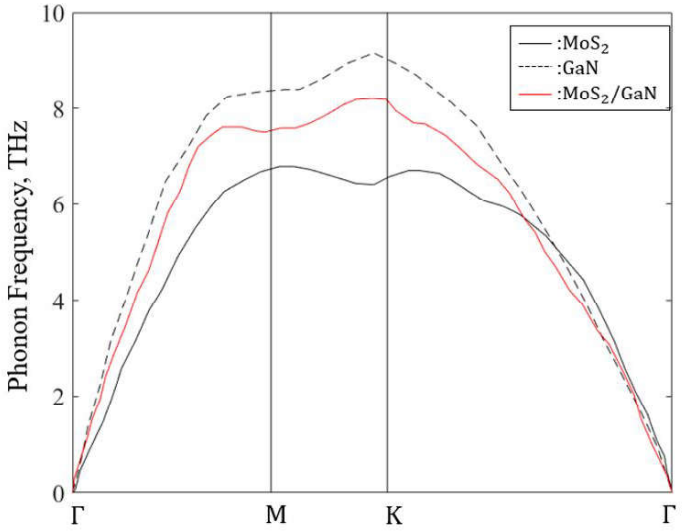



Figure 4.10. LA phonon modes of $MoS_2$,GaN, and $MoS_2/GaN$ heterostructure.

Phonon dispersion relations show that new ZA phonon modes emerge in $2D/SiO_2$ heterostructures. However, in the same heterostructures, LA and TA phonon modes of 2D materials are changed, and phonon dispersions become more similar to $SiO_2$. Similarly, PDOS of heterostructures is much similar to PDOS of $SiO_2$. Even though phonon transport mechanisms are changed, and phonons in heterostructure behave like phonons in $SiO2$, $h-BN$ lowers the low-frequency peak of $SiO_2$, which leads to lower scattering rates in $SiO2$ substrate and improves the heat conduction abilities of this material. In $h-BN/SiO_2$ heterostructures, LA phonon modes become shortened and similar to isolated $SiO_2$. Similarly, $h-BN/GaN$ dispersion and DOS become much familiar to $GaN$. These changes in phonon properties show that phonon scattering mechanisms in 2D/3D vdW heterostructures are dominated mainly by 3D materials [25,57,157] [24, 52, 146].

Based on these results, we can conclude that using a low thermal conductivity substrate material heavily limits the in-plane heat carrying capacity of the 2D mate-

rials. On the other hand, using a high thermal conductivity substrate like $GaN$ can increase the thermal conductivity of the 2D materials in the heterostructure with lower thermal conductivity, with the price of reduced thermal conductivity of its layers in the vicinity of the interface. These effects combined with the low TBC at the interface can decrease the thermal transport rate and cause temperature rises and thus should be well understood for proper thermal design of devices composed of these heterostructures. On the contrary, 2D materials increase the low thermal conductivity of the amorphous $SiO_2$ substrates and provide heterostructures with very high TBC values. Finally, with its already high thermal conductivity, $h-BN$ improves the thermal performance of both $SiO_2$ and $GaN$ and behaves as a heat spreader in heterostructures. Based on such properties, it can play a crucial role in electronic packaging.

## 4.3. Conclusion

This study calculated the TBC and individual in-plane thermal conductivities of materials in $2D/GaN$ and $2D/SiO_2$ heterostructures. The results show that its high-frequency peak at low-frequency phonon modes, amorphous $SiO_2$ has a higher substrate scattering rate which causes more ZA phonon modes and higher TBC values than $GaN$ interfaces. It has been known that the lattice mismatch between layers decreases the phonon transmission rate and decreases the TBC at interfaces. However, $h-BN/GaN$ and $h-BN/SiO_2$ interfaces have much higher TBC than other interfaces despite their high lattice mismatch. We showed that the ZA PDOS match is a more meaningful indicator for predicting the TBC trends since ZA phonon modes contribute to most TBC. Increased number of 2D material layers cause more intralayer adhesion energy and increase the energy transmission rate and TBC of the interface but decrease the in-plane thermal conductivity. After examining the effect of different material properties and TBC values, an analytical expression is proposed to predict the TBC and quantify the trend between TBC and material properties.

It is also shown that the individual thermal conductivities of 2D materials are also affected by the thermal conductivity of its substrate material. Low thermal conductivity substrates cause stronger phonon – phonon scattering and cause a significant

reduction in thermal conductivity of 2D materials. The amount of thermal conductivity reduction of the 2D material depends on the thermal conductivity difference of the materials in the heterostructure. Therefore, thermal management plans and electronic packaging with heterostructures should consider in-plane thermal conductivity and TBC at the interfaces. These results show the importance of material selection and proper modeling parameters for the proper design of thermal pathways in new generation 2D devices.

# 5. LOCALIZED HEATING

Continuous shrinking and increased power densities leads to emergence of localized heating areas in confined spaces in semiconductor devices. The effect of micro-and nanoscale localized heating areas can be devastating for the device. For instance, a confined localized heating region, as small as 50 nm, may lead to a hot spot formation where the temperature is significantly higher than the rest of the device. This temperature change in devices leads to thermal size effects and change in thermal properties, and consequently to even higher device temperatures [149]. Therefore, a complete understanding of thermal transport near localized heating is necessary for nanodevices.

The temperature profile of devices and localized heating areas are mainly obtained using numerical models based on finite element and/or finite volume analysis. Even though these models are fast and straightforward, they cannot take ballistic effects into account since they are based on diffusive models. Another common approach is using iterative solutions of phonon BTE. Even though phonon BTE can calculate the properties more accurately, they may oversimplify the electronic structure of materials [131]. Phonon BTE cannot be solved analytically, and its numerical solution requires a lot of computational power and time. Thus, some simplifications can reduce the time and computational power requirement. Therefore, a clear understanding of thermal transport near localized heating areas is essential to design better and more reliable devices [150, 151]. MD simulations in this chapter are used to observe the thermal transport trends near these areas. Even though MD simulations cannot observe the electrons, it is already shown that high-energy electrons transmit their energy to optical phonons, and then, these phonons decay into acoustic phonons. Therefore, the MD method is chosen since MD captures the phonon-phonon scatterings and phonon anharmonicity very well [152].

Thus, the temperature profile of bulk and thin films is modeled via MD and compared with the continuum model numerically solved by finite element analysis to understand the effect of heat generation on the thermal size effects [34]. To observe the

thermal size effects, localized heating with varying sizes and power are implemented in the domain. By comparing the results with earlier findings in Chapter 3, localization effect on phonon transport is investigated.

## 5.1. Method

MD simulations are used to capture the phonon scattering events and size effects on phonon transport. For these simulations, $GaN$ bulk and thin films are used. Due to its high thermal conductivity, $GaN$ is selected since it is widely used for electronic and optoelectronic applications subjected to high power densities and temperatures [15, 63]. Therefore, accurate modeling of $GaN$ structures that may be subjected to localized heating is vital for the device's reliability. Here, rNEMD simulations are used to obtain the temperature profile of the structure. The computation procedure of this method is similar to the NEMD method used in Chapter 3 and 4, and the only difference is that instead of specified temperature, specified heat fluxes are imposed on the system. rNEMD not only allows applying specified heat flux but also captures phonon anharmonicity and high order phonon scatterings observed near hot spots. Specular walls, $p = 1$, are applied to the fixed boundaries to reduce the effect of phonon-boundary scatterings to focus on phonon localization.

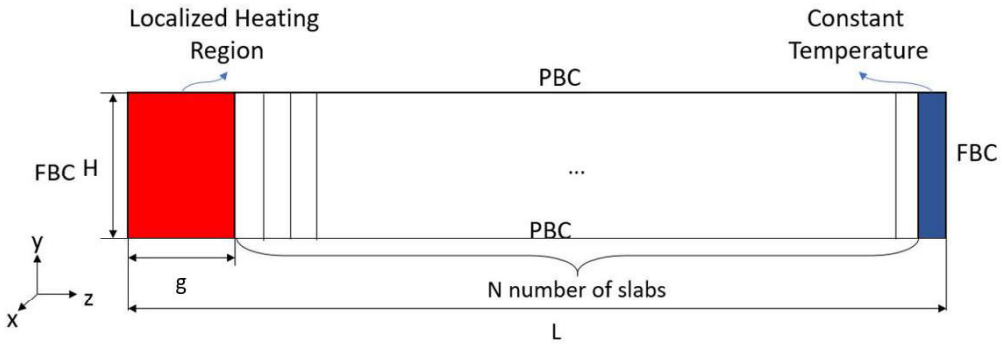



Figure 5.1. Simulation box for NEMD simulations.

In this study, both thin films and bulk materials are modeled. Albar and Donmezer [124] reported the maximum phonon MFP $\lambda_{max}$ of $GaN$ at 300 K is $\lambda_{max}$=1661 nm and this value is reduced by increasing temperature. Therefore, it is assumed that

structures with a thickness, $L$, larger than 1600 nm are bulk materials, and classical size effects are not observed. The schematic picture of the simulation box is shown in Figure 5.1. Here, films with thickness, $L$, ranges between 200 nm – 3000 nm are used in these simulations. The width of the domain, $W$, is kept constant at 200 nm. $H$, the height of the structure is selected as kept the aspect ratio ($A_r = L/H$) between $2 - 5$. The thickness of localized heating region, $l$, is ranges between 50 nm - 1000 nm to show the effect of size of the localized heating region. Periodic boundary condition (PBC) is applied to the walls in x- and y-directions, while fixed boundary condition (FBC) is applied to the walls in the z-direction. To observe the effect of the localized heating on the domain, different values of thickness of the domain and hot spot ratio, $L/g$, are applied. A localized heating area is applied as a slab since the NEMD scheme only allows investigating the heat conduction in one direction. The structure is divided into 10 nm-thick slabs to obtain a detailed temperature profile. The temperature of these slabs is calculated by using the Equipartition theorem, as given in Equation (2.5). The velocity Verlet algorithm is implemented for integration of Newton's Law of Motion.

As stated earlier in Chapter 2, the Langevin thermostat applies random forces and friction to the particles, simulating the phonon transport in solids more accurately. Therefore, a Langevin thermostat is applied to impose heating on the simulation domain. In simulations for the bulk and thin film domain, periodic boundary conditions are applied along the x- and y-directions. Fixed boundary conditions and specular walls are applied to the z-direction. Then, another thermostat is applied to the far-wall and is implemented as a constant temperature boundary condition. Same boundary conditions are applied for continuum approach-based simulations.

After the temperature profile of $GaN$ domains is obtained, the local thermal conductivity of the domain at near localized heating regions and far-away regions are also investigated to determine accurate parameters for the quasi-ballistic approach. The local thermal conductivity of regions is obtained by dividing the heat flux by the temperature difference between neighbor slabs. These local thermal conductivity values are also compared to the temperature – thermal conductivity relation and improved TC-AS model. The temperature – thermal conductivity relation only considers the

temperature effect on thermal conductivity, while improved TC-AS considers both the boundary size effects and temperature effects. The difference between the relation and MD simulation obtained shows the effect of phonon localization in bulk materials since the MD both consider the localization and temperature changes. The discrepancy between the MD model and improved TC-AS indicates the phonon localization in thin films since improved TC-AS cannot observe the effect of localized heating. The results obtained from all approaches are given next.

## 5.2. Results and Discussion

In this section, peak temperature, $T_{peak}$, and local thermal conductivity, $k_L$, of $GaN$ bulk and thin films are presented. By comparing these values, classical and thermal size effects are investigated and phonon localization effect on thermal transport is obtained.

Temperature distribution along the bulk and thin films are investigated here. Figure 5.2 shows the temperature distribution along with bulk $GaN$, with the thickness, $L$, of 2000 nm, subjected to localized heating with thickness, $l$, of 100 nm (a) and 1000 nm (b), marked as red in figures. These figure shows that thermal model based on diffusive thermal transport (DM) fails to estimate the peak temperature of semiconductor materials in these conditions. This discrepancy stems from the approaches used to calculate these values. Since DM model uses the bulk thermal conductivity along with the structure, it cannot capture the change in thermal transport due to temperature changes and phonon localization. Even though increased temperature reduces the maximum MFP and, hence, boundary size effects vanish in the structures, temperature changes, and high energy phonons, which disrupt the phonon transport, slow down the thermal transport, and lead to much higher device temperatures than anticipated by diffusive models. These differences between predictions may lead to unexpected performance loss and reliability issues in semiconductor devices. Since MD simulations observe the motion of phonons, it can model the phonon transport in these structures much more accurately.

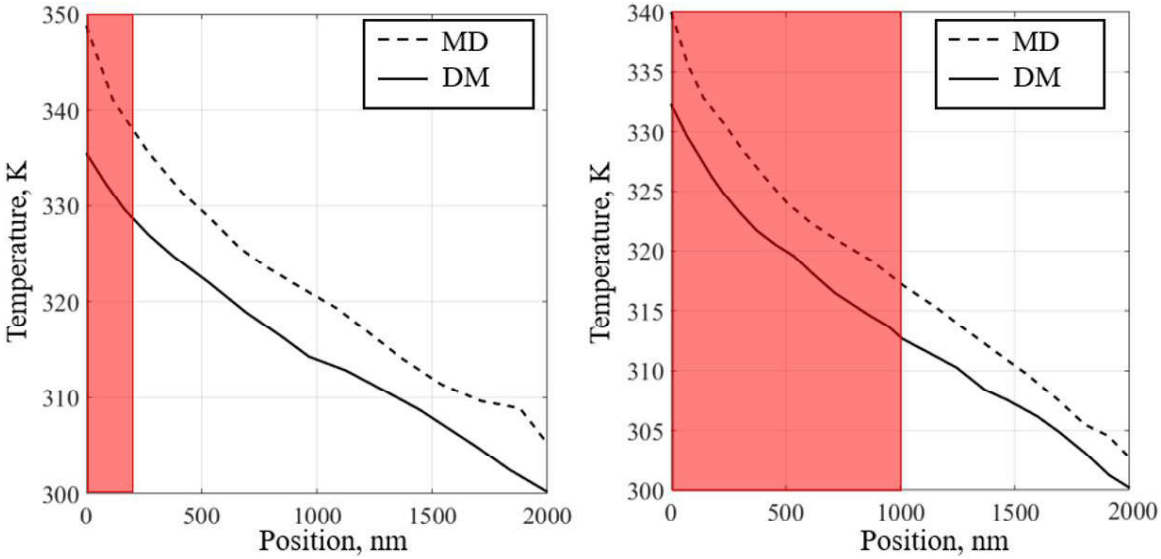



Figure 5.2. Temperature distribution along the 2000 nm-thick $GaN$ subjected to 100 nm-thick (a) and 1000 nm-thick (b) localized heating region with the power of 50 mW. Red areas marked in plots represent the localized heating.

In confined areas, heat is trapped; therefore, the localization effect becomes more dominant. It is observed that prediction is getting closer with larger regions. The difference between peak temperature estimations of DM and MD models are 16 K and 8.5 K for ,$l$, 100 nm-thick and 1000 nm-thick localized heating regions in, $L$, 2000 nm-thick film. Same trends are also observed in the local thermal conductivity of bulk structures, as shown in Figure 5.3. Both figures indicate that the effect of localized heating diminishes with moving away from the heating region. In Figure 5.3, local thermal conductivity estimations of $GaN$ structures are compared with the thermal conductivity relation obtained in Chapter 3 for $GaN$. This shows that even a model that includes the thermal conductivity change with temperature could not estimate the peak temperature accurately. Here, the difference between model stems from the effect of phonon localization. Therefore, underestimating the effect of phonon localization on thermal transport leads to performance and reliability issues and even to degradation of the device.

The localization effects in Figure 5.2 and 5.3 are the highest at the localized

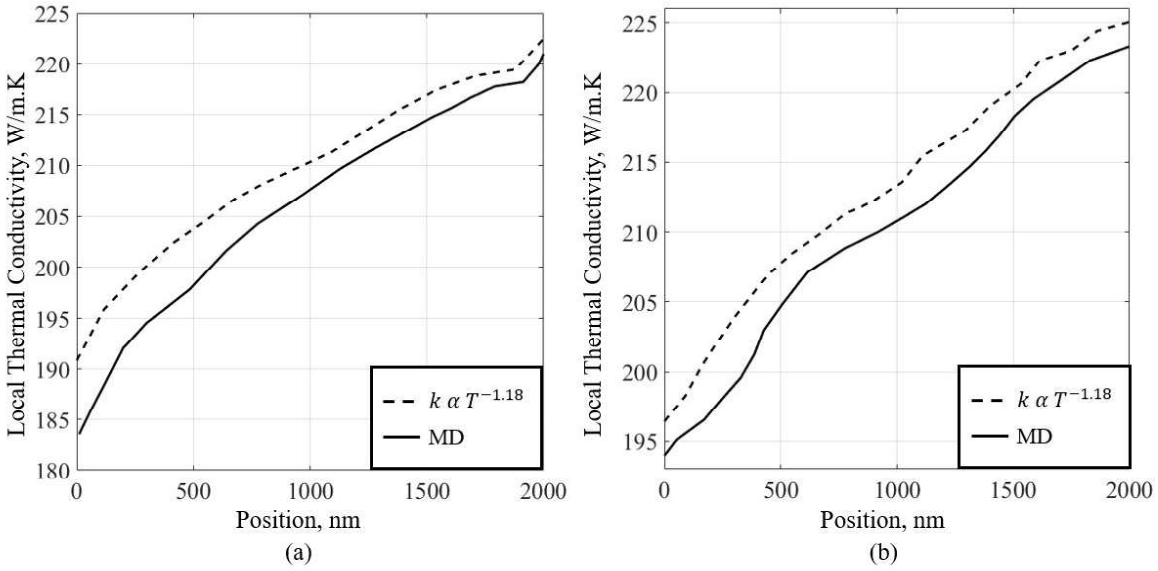



Figure 5.3. Temperature distribution along the 2000 nm-thick $GaN$ subjected to 100 nm-thick (a) and 1000 nm-thick (b) localized heating region with the power of 50 mW. Red areas marked in plots represent the localized heating.

heating area and are reducing as moving away from the localized heating, as expected. This effect becomes nearly negligible near the far-wall area. Also, when the thickness of the area is decreased, localization effects become more dominant, as seen in Figure 5.2 and 5.3. While 100 nm-thick localized heating causes a 18% reduction in thermal conductivity in the localized heating area. Even at a distance of 1000 nm, thermal conductivity is less than the bulk thermal conductivity. 1000 nm-thick hot spot causes a less significant reduction in local thermal conductivity near localized heating area. Even though there is a slight difference between models, the difference can be negligible in near-wall areas.

The effect of phonon localization and boundary size effects should be evaluated together to obtain a complete picture. Therefore, thin films with localized heating regions are also modeled in this study. In thin films, localized heating becomes an even more severe problem for the performance and reliability of the device. Increased phonon-boundary scatterings also cause a significant reduction in the thermal conductivity of materials, besides phonon localization. This additional reduction leads to

higher temperatures and more localization which causes even more reduction in thermal conductivity of materials. Therefore, accurate peak temperature prediction is vital for reliable operation of the devices include thin films.

To see how localized heating affects the phonon transport through thin films, thin films with the thickness of $200 - 2000$ nm with 50 nm or 100 nm localized heating regions are investigated. Their temperature distribution is compared with the DM model to observe the different quasi-ballistic effects on thermal transport and isolate the effect of phonon localization. Also, local thermal conductivities are calculated, and these values are compared with the improved TC-AS model.

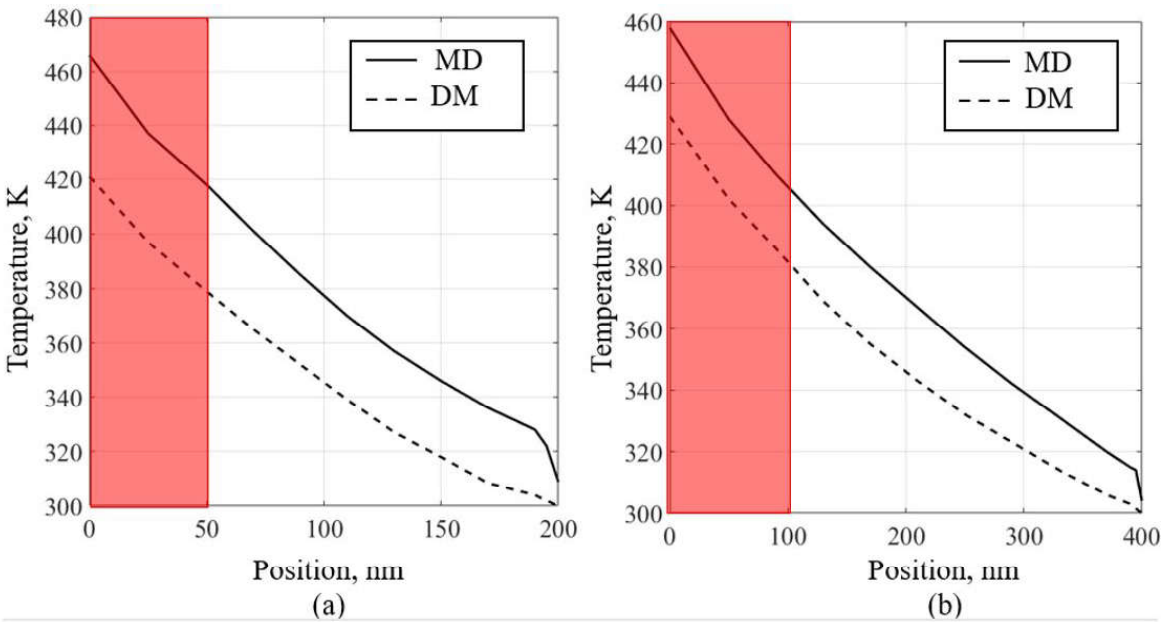



Figure 5.4. Temperature distribution along the $GaN$ thin film (with same $L/g$ ratio) subjected to 50 nm thick and 100 nm thick localized heating with the power of 50 mW.

As an example of these studies, Figure 5.4 present the temperature distribution along, $L$, 200 nm and 400 nm thick $GaN$ thin films with, $l$, 50 nm (a) and 100 nm (b) thick localized heating regions, respectively. Similar to bulk results, the local thermal conductivity of the thin film is much different near localized heating regions according to MD simulations. Despite that DM predict the peak temperature of thin films, $T_{peak}$

as 420 K and 424 K, MD simulations observed that these values as 468 K and 460 K, as shown in Figure 5.4 (a) and (b). Compared to bulk cases, peak temperature rise in thin films are much more vital. In addition to the boundary size effects that occurred in thin films, phonon localization and thermal size effects cause a significant reduction in thermal transport through thin films. Both phonon-boundary scatterings and high-energy phonons disrupt the movement of other phonons and reduce their MFPs.

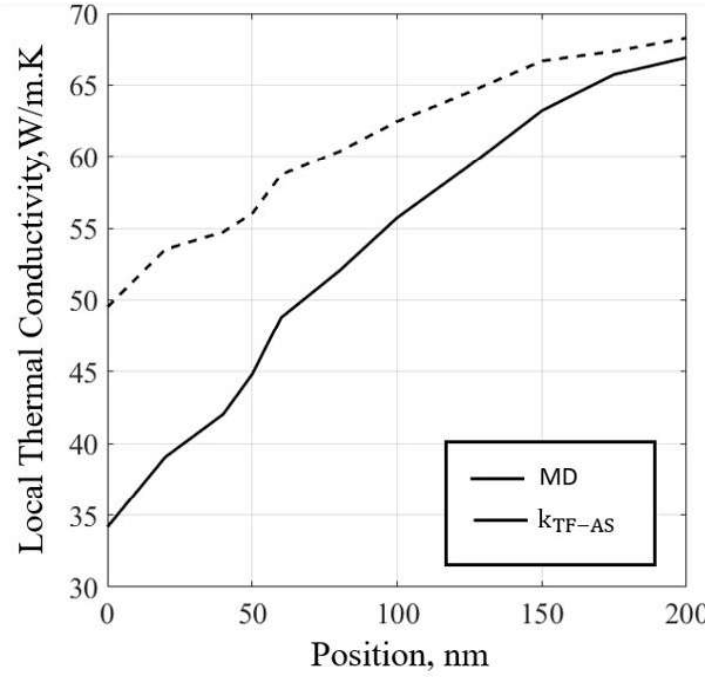



Figure 5.5. Local thermal conductivity along the 200 nm-thick GaN subjected to 50 nm-thick localized heating with 50 mW power.

Figure 5.5 also provides a comparison of local thermal conductivity estimated by NEMD simulations and improved TC-AS model, $k_(tf - AS)$. Similar to DM, the improved TC-AS model fails to predict the thermal conductivity of thin film. Due to localization effects and increased temperature, the local thermal conductivity of thin film, $k_L$, drops from 121.5 W/m.K to 34.85 W/m.K near a 50 nm thick localized heating region. Even though improved TC-AS considers the temperature change while calculating thermal conductivity, results obtained from MD simulations differ due to localization effects. Localization of phonons causes a 31.1% deviation from improved

TC-AS., as shown in Figure 5.5. Even though the improved TC-AS model can capture the effect of phonon-boundary scatterings and temperature changes very accurately, the phonon localization effect is missing. Therefore, this scheme can be expanded to cover phonon localization.

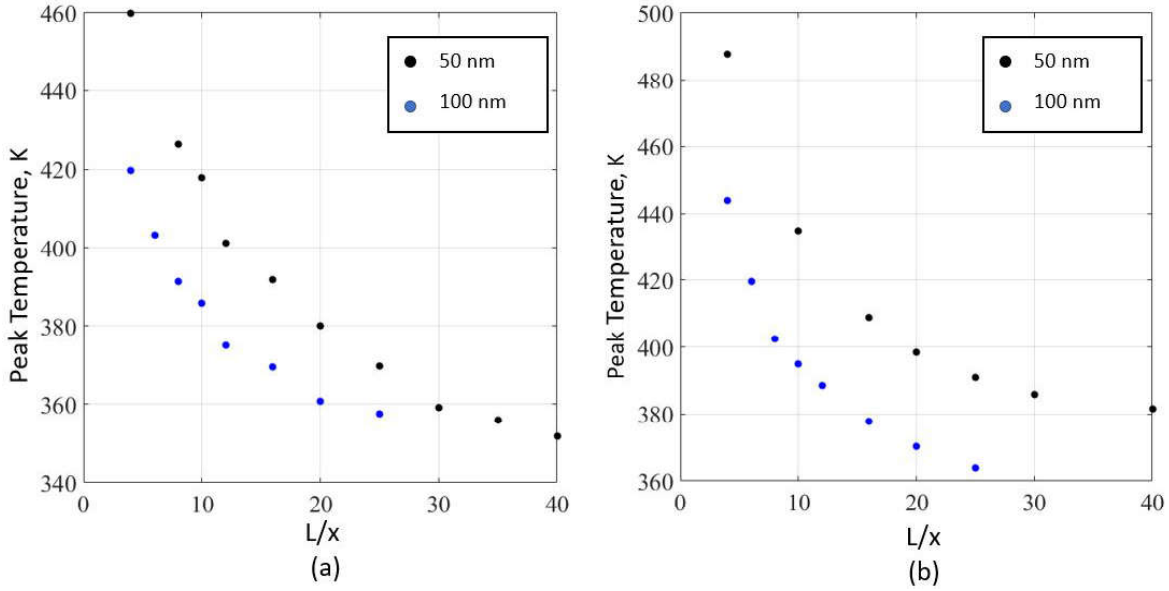



Figure 5.6. Peak temperature of structures according to different $L/g$ values when subjected to 50 nm and 100 nm thick localized heating with the power of 50 mW (a) and 100 mW (b).

Besides the size of the structure and heating area, the power of localized heating regions is essential. All peak temperature values, $T_{peak}$, obtained from MD simulations for bulk and thin films with the thickness of 200 nm – 2500 nm with respect to the $L/g$ ratio for different applied power are presented in Figure 5.6. These results indicate that the peak temperatures of the thin films increase by increasing the $L/g$ ratio and decreasing thin film thickness, $L$. Moreover, peak temperature increases with the power, $p$. With increasing thin film thicknesses, boundary size effects diminish, and the peak temperature of the thin films is reduced. Similarly, the slope of reduction in thermal conductivity line drops significantly when the thickness of the thin film becomes longer than maximum phonon MFP, $\lambda_{max}$.

Even in the largest domain, the DM model cannot accurately predict the peak

temperature value; therefore, a model consisting of temperature dependency of thermal conductivity, classical size effects, and localization is necessary for accurate simulations. Trends described above can be used to build a new model based on improved TC-AS to cover the phonon localization additional to boundary size effects and temperature. The data obtained in the scope of this research provides a guideline to build such a relation. The effect of localization becomes more dominant with increased power density; hence, increased power and/or decreased thickness of the structure or localization heating area cause much more deviation between improved TC-AS model and NEMD simulations. To increase the accuracy of DM model, a new relation is proposed. This new relation, $f$ shown as

$$f = exp(Kn^{-1.16}\theta G^{-1.05}P^{0.85}m^{1.72}BWR_{ZA}^{\theta_D/T}), \tag{5.1}$$

includes the effect of phonon localization and localized heating to improved TC-AS model obtained in Chapter 3. Here, the effect of film thickness, $L$, changes the power of $Kn$ ($=\lambda_{max}/L$) number in improved TC-AS relation. As shown in this Chapter, reducing localized heating thickness has a limiting effect on thermal conductivity and this effect is included as the parameter $G$, ($=\lambda_{max}/g$). $P$ is the dimensionless power ($=p/1$W) and indicated the effect of heat flux applied to the region. Other parameters are the same the ones used in the improved TC-AS model proposed in Chapter 3. Thermal conductivity as shown

$$k_{tf-AS}^{*} = f * k_{TC-AS}, \tag{5.2}$$

used in DM model to predict the temperature more accurately can be obtained by multiplying the function, $f(Kn, \theta, G, P$,phonon properties), with thermal conductivity estimation obtained from accumulation spectra, $k_{TC-AS}$, as shown in Equation (5.1).

Figure 5.7 shows the results obtained from the DM model using the thermal conductivity value, $k_{tf-AS}^{*}$. $T_{peak}$ value and temperature distribution in a thin film with thickness of, $L$, 200 nm and localized heating region with thickness of, $l$, 50 nm.

Despite the new model, there is 9 K difference between MD and DM model predictions with new thermal conductivity relation. For larger films and localized heating regions, where sub-continuum effects become less effective, deviation between these models become less. This deviation between models is caused by the sub-continuum effects that cannot be observed by Fourier's Law of Conduction.

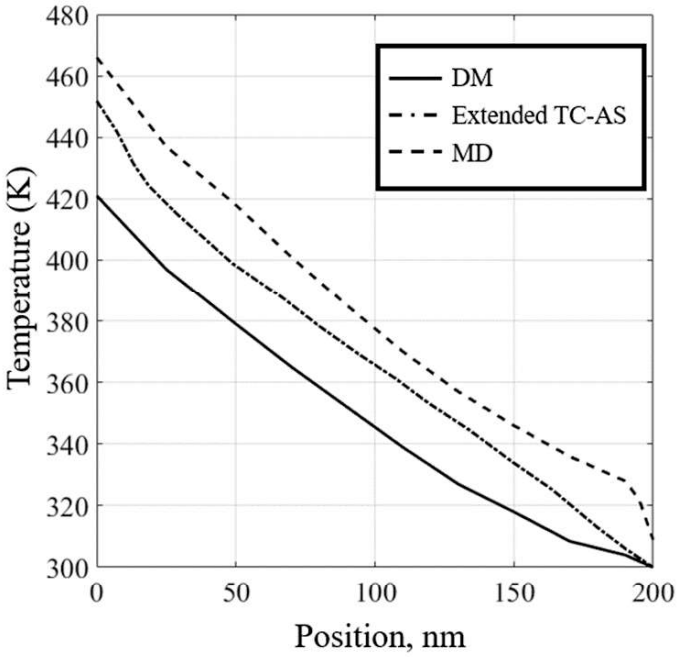



Figure 5.7. Temperature distribution along 200 nm thick thin film with 50 nm thick localized heating obtained from MD simulations, DM model with thermal conductivity calculated by improved TC-AS and extended TC-AS model.

## 5.3. Conclusion

This chapter of the thesis investigates temperature distribution, the local thermal conductivity of the $GaN$ bulk and thin films using rNEMD simulations. By comparing the temperature distribution along with bulk materials and thin films, ballistic-diffusive heat transfer trends in and near localized heating regions are investigated. In these structures, both classical and thermal size effect mechanisms are effective. Additional to the ones investigated in other chapters, in and near localized heating areas, the phonon localization effect is observed. To investigate this effect, thermal conductivity

relations obtained in Chapter 3 and the improved TC-AS model are used.

Our results show that localized heating areas in bulk materials and thin films lead to higher peak temperatures and lower thermal conductivity, leading to severe reliability and performance issues. In bulk materials, thermal transport is restricted due to temperature changes, as well as phonon localization. Since the DM model cannot observe the quasi-ballistic effects on phonon transport, the discrepancy between DM and MD models is interpreted as phonon localization and temperature changes. Due to these effects, it is observed that temperature is increased aggressively near hot spots, according to MD simulations. Moreover, temperature changes become more significant when the thickness of the localized heating region is larger, even if the $L/g$ ratio is the same. To isolate the effect of the localized heating region, the change in thermal conductivity according to temperature is calculated by the temperature – thermal conductivity relation. The deviation between the MD model and the relation is considered as the effect of the localized heating.

Similar to bulk materials, temperature distribution and local thermal conductivity along the GaN thin films are also affected by the presence of hot spots. Here, the temperature rise is caused by phonon localization and change in temperature and classical size effects. To observe the phonon localization, other effects should be calculated, as well. Improved TC-AS can observe the thermal conductivity reduction caused by classical size effects and temperature changes; this equation is used to isolate the phonon localization effect. Localization effects become more dominant near localized heating, and therefore, localized heating in thin films should be considered carefully. Thermal conductivity reduction in these structures is related to how much heat is trapped in these structures. Therefore, more confined structures cause more phonon localization, therefore decrease in size of the structure and/or localized heating region lead to much severe thermal conductivity reduction and temperature rise. Moreover, when the maximum phonon MFP of materials is lower, the impact of classical size effects diminishes but thermal size effects become more significant. Also, an increase in power leads to larger heat flux and higher device temperatures, as well as lower thermal conductivity. These observed trends in thermal transport in and near localized

heating areas can be used to build such relations to improve the accuracy of existing models. A detailed picture of thermal conductivity along this region can be used with the gray approach to solving the phonon BTE to provide a complete understanding of size effects in all domains of the semiconductor devices.

# 6. CONCLUSIONS AND IMPLICATIONS FOR FUTURE RESEARCH

As the dimension of semiconductor devices reduces, reliability and performance issues are increased. When the size of the structure becomes comparable to phonon MFP, thermal transport deviates from the continuum behavior, and quasi ballistic effects dominate the thermal transport. In the ballistic-diffusive regime, thermal transport is slowed down, and temperature may be higher than anticipated. Since continuum models cannot observe the impact of quasi-ballistic effects, this thesis investigates the heat transport regime resulting from three different cases in semiconductor devices. These cases are thermal transport through thin films, across interfaces, and near localized heating areas. In Chapter 2, methodology of the MD simulations used in this study is introduced and necessary equations for these simulations are given.

In Chapter 3, thermal transport through thin films is investigated, and a new method to estimate the thin film thermal conductivity of GaN and AlN from accumulation spectra (TC-AS) was introduced. By comparing thermal conductivity estimations from TC-AS and NEMD simulations, it was found that the TC-AS model cannot produce accurate results at short length scales and low temperatures. Its accuracy To improve the accuracy of the model, a fitting function, $f$, is proposed. After a careful examination, the function parameters were defined: temperature, $T$, and thickness of the film, $L$, Debye temperature, $\theta_D$, the bandwidth of LA phonon modes, $BWR_{LA}$ and maximum phonon MFP of materials, $\Lambda_{max}$, and mass ratio of atoms, $M$. This new model shows the thermal transport trends in thin films and provide more accurate thermal conductivity estimations for crystalline semiconductor. However, this model is only tested for AlN and GaN; more materials should be investigated to specify the function's parameters. Also, a new mass ratio relation should be considered for materials with three or more different atoms.

Chapter 4 provides insightful data regarding in-plane and cross-plane thermal

transport through heterostructures. By observing the phonon and lattice properties, TBC at 2D/3D heterostructures interfaces and in-plane thermal conductivity changes caused by these interfaces are investigated. These investigations show that the difference in phonon DOS of materials, especially ZA phonon modes, has the most significant impact on TBC. Also, materials with a high number of low-frequency phonons have higher TBC. Furthermore, lattice match and the number of material layers are also important parameters. Based on these trends and parameters, a new model is proposed to calculate the TBC of an interface with a linearly fitted equation. This function helps to predict the TBC by considering some properties of material formed the interface. Also, the study shows that the in-plane thermal conductivity of materials in heterostructures is changed. LA phonon modes of heterostructure become more similar to the 3D material; therefore, 3D material becomes more dominant in thermal conductivity changes. However, the amount of change most likely depends on the difference between the thermal conductivity of materials when they are isolated. Also, the thermal conductivity of 3D materials only changes in a tiny region next to the interface. Therefore, heat spreading or thermoelectric effects of 2D materials might be limited only to a small region. In conclusion, this chapter presents some trends in thermal transport in heterostructures and through interfaces; however, more interfaces should be investigated to build a function to determine the in-plane thermal conductivity and TBC of a heterostructure without needing any further simulation or experiments.

In the last chapter, thermal transport near localized heating regions in bulk materials and thin films is investigated. The study shows that the peak temperature of the device and local thermal conductivities cannot be obtained accurately by using a diffusive model. Instead, MD simulations are used to calculate these values by considering quasi-ballistic effects and temperature changes. By comparing the thermal conductivity-temperature relations and improved TC-AS model, the effect of phonon localization is observed. Simulations show that the peak temperature of devices depends on the size of the localized heating region and the device. With decreasing $L/x$ ratio, estimated peak temperature falls, and thermal transport becomes more similar to continuum behavior. In the end, even though thermal transport trends have been specified for localized heating regions, a new model can be developed to calculate the

local thermal conductivity by considering quasi-ballistic effects by expanding the TC-AS model. By adding the effect of power, size of the localized heating regions and structure can be used to expand the application area of improved TC-AS model to the localization effects.

# REFERENCES


1. Chen, G., *Nanoscale Energy Transport and Conversion a Parallel Treatment of Electrons, Molecules, Phonons, and Photons*, Oxford University Press, 2005.

2. Moore, A. L. and L. Shi, "Emerging challenges and materials for thermal management of electronics", *Materials Today*, Vol. 17, No. 4, pp. 163–174, 2014.

3. Cahill, D. G., P. V. Braun, G. Chen, D. R. Clarke, S. Fan, K. E. Goodson, P. Keblinski, W. P. King, G. D. Mahan, A. Majumdar, H. J. Maris, S. R. Phillpot, E. Pop and L. Shi, "Nanoscale Thermal Transport. II. 2003-2012", *Applied Physics Reviews*, Vol. 1, No. 1, pp. 1–46, 2014.

4. Chapman, J. B. J., *Improving the Functional Control of Ferroelectrics Using Insights from Atomistic Modelling*, Ph.D. Thesis, UCL (University College London), 2018.

5. Albar, I. and N. Donmezer, "Mean Free Path–Thermal Conductivity Accumulation Calculations for Wurtzite Gallium Nitride: Two Approaches", *Nanoscale and Microscale Thermophysical Engineering*, Vol. 24, No. 2, pp. 80–93, April 2020.

6. Frazer, T. D., J. L. Knobloch, K. M. Hoogeboom-Pot, D. Nardi, W. Chao, R. W. Falcone, M. M. Murnane, H. C. Kapteyn and J. N. Hernandez-Charpak, "Engineering Nanoscale Thermal Transport: Size- and Spacing-Dependent Cooling of Nanostructures", *Physical Review Applied*, Vol. 11, No. 2, pp. 1–8, 2019.

7. McGaughey, A. J., E. S. Landry, D. P. Sellan and C. H. Amon, "Size-Dependent Model for Thin Film and Nanowire Thermal Conductivity", *Applied Physics Letters*, Vol. 99, No. 13, pp. 1–3, September 2011.

8. Siemens, M. E., Q. Li, R. Yang, K. A. Nelson, E. H. Anderson, M. M. Murnane and H. C. Kapteyn, "Quasi-Ballistic Thermal Transport from Nanoscale Interfaces

Observed Using Ultrafast Coherent Soft X-Ray Beams", *Nature Materials*, Vol. 9, No. 1, pp. 26–30, 2010.

9. Cahill, D. G., W. K. Ford, K. E. Goodson, G. D. Mahan, A. Majumdar, H. J. Maris, R. Merlin and S. R. Phillpot, "Nanoscale Thermal Transport", *Journal of Applied Physics*, Vol. 93, No. 2, pp. 793–818, 2003.

10. Yang, F. and C. Dames, "Mean Free Path Spectra as a Tool to Understand Thermal Conductivity in Bulk and Nanostructures", *Physical Review B*, Vol. 87, No. 3, pp. 1–12, 2013.

11. Turney, J. E., A. J. McGaughey and C. H. Amon, "In-Plane Phonon Transport in Thin Films", *Journal of Applied Physics*, Vol. 107, No. 2, pp. 1–8, 2010.

12. Wu, R., R. Hu and X. Luo, "First-Principle Based Full-Dispersion Monte Carlo Simulation of the Anisotropic Phonon Transport in the Wurtzite GaN Thin Film", *Journal of Applied Physics*, Vol. 119, No. 14, pp. 1–9, 2016.

13. Kaiser, J., T. Feng, J. Maassen, X. Wang, X. Ruan and M. Lundstrom, "Thermal Transport at the Nanoscale: A Fourier's Law vs. Phonon Boltzmann Equation Study", *Journal of Applied Physics*, Vol. 121, No. 4, pp. 1–10, January 2017.

14. Regner, K. T., J. P. Freedman and J. A. Malen, "Advances in Studying Phonon Mean Free Path Dependent Contributions to Thermal Conductivity", *Nanoscale and Microscale Thermophysical Engineering*, Vol. 19, No. 3, pp. 183–205, 2015.

15. Freedman, J. P., J. H. Leach, E. A. Preble, Z. Sitar, R. F. Davis and J. A. Malen, "Universal Phonon Mean Free Path Spectra in Crystalline Semiconductors at High Temperature", *Scientific Reports*, Vol. 3, pp. 1–6, October 2013.

16. Beechem, T. E., A. E. McDonald, E. J. Fuller, A. A. Talin, C. M. Rost, J. P. Maria, J. T. Gaskins, P. E. Hopkins and A. A. Allerman, "Size Dictated Thermal Conductivity of GaN", *Journal of Applied Physics*, Vol. 120, No. 9, pp. 1–6, 2016.

17. Sood, A., F. Xiong, S. Chen, R. Cheaito, F. Lian, M. Asheghi, Y. Cui, D. Donadio, K. E. Goodson and E. Pop, "Quasi-Ballistic Thermal Transport Across MoS2 Thin Films", *Nano Letters*, Vol. 19, No. 4, pp. 2434–2442, 2019.

18. Albar, I. and N. Donmezer, "Phonon Mean Free Path - Thermal Conductivity Relation in AlN", *2019 18th IEEE Intersociety Conference on Thermal and Thermomechanical Phenomena in Electronic Systems (ITherm)*, Vol. 2019-May, pp. 127–130, 2019.

19. Larkin, J. M. and A. J. McGaughey, "Thermal Conductivity Accumulation in Amorphous Silica and Amorphous Silicon", *Physical Review B*, Vol. 89, No. 14, pp. 1–12, 2014.

20. Correa, G. C., C. J. Foss and Z. Aksamija, "Interface Thermal Conductance of van der Waals Monolayers on Amorphous Substrates", *Nanotechnology*, Vol. 28, No. 13, pp. 1–8, 2017.

21. Foss, C. J. and Z. Aksamija, "Quantifying Thermal Boundary Conductance of 2D-3D Interfaces", *2D Materials*, Vol. 6, No. 2, pp. 1–12, 2019.

22. Pop, E., "Energy dissipation and transport in nanoscale devices", *Nano Research*, Vol. 3, No. 3, pp. 147–169, 2010.

23. Antidormi, A., L. Colombo and S. Roche, "Emerging Properties of Non-Crystalline Phases of Graphene and Boron Nitride based materials", *Nano Materials Science*, , No. December 2020, pp. 1–8, 2021.

24. Giri, A. and P. E. Hopkins, "A Review of Experimental and Computational Advances in Thermal Boundary Conductance and Nanoscale Thermal Transport across Solid Interfaces", *Advanced Functional Materials*, Vol. 30, No. 8, pp. 1–21, 2020.

25. Kang, S., D. Lee, J. Kim, A. Capasso, H. S. Kang, J. W. Park, C. H. Lee and

G. H. Lee, "2D Semiconducting Materials for Electronic and Optoelectronic Applications: Potential and Challenge", *2D Materials*, Vol. 7, No. 2, pp. 1–22, 2020.

26. Hopkins, P. E., "Thermal Transport Across Solid Interfaces with Nanoscale Imperfections: Effects of Roughness, Disorder, Dislocations, and Bonding on Thermal Boundary Conductance", *ISRN Mechanical Engineering*, Vol. 1, No. 1, pp. 1–20, 2013.

27. Suryavanshi, S. V., A. J. Gabourie, A. Barati Farimani and E. Pop, "Thermal Boundary Conductance of Two-Dimensional MoS2 interfaces", *Journal of Applied Physics*, Vol. 126, No. 5, pp. 1–7, August 2019.

28. Yasaei, P., A. Behranginia, Z. Hemmat, A. I El-Ghandour, C. D. Foster and A. Salehi-Khojin, "Quantifying the Limits of Through-Plane Thermal Dissipation in 2D-Material-based Systems", *2D Materials*, Vol. 4, No. 3, pp. 1–8, 2017.

29. Christofferson, J., K. Maize, Y. Ezzahri, J. Shabani, X. Wang and A. Shakouri, "Microscale and Nanoscale Thermal Characterization Techniques", *Journal of Electronic Packaging*, Vol. 130, No. 4, pp. 1–6, 2008.

30. Raleva, K., E. Bury, B. Kaczer and D. Vasileska, "Uncovering the temperature of the hotspot in nanoscale devices", *2014 International Workshop on Computational Electronics*, pp. 1–3, 2014.

31. Torregiani, C., B. Vandevelde, H. Oprins, E. Beyne and I. De Wolf, "Thermal Analysis of Hot Spots in Advanced 3D-stacked structures", *2009 15th International Workshop on Thermal Investigations of ICs and Systems*, October, pp. 56–60, Leuven, Belgium, 2009.

32. Mohanty, S. K., Y. Y. Chen, P. H. Yeh and R. H. Horng, "Thermal Management of GaN-on-Si High Electron Mobility Transistor by Copper Filled Micro-Trench Structure", *Scientific Reports*, Vol. 9, No. 1, pp. 1–9, 2019.

33. Donmezer, N. and S. Graham, "The Impact of Noncontinuum Thermal Transport on the Temperature of AlGaN/GaN HFETs", *IEEE Transactions on Electron Devices*, Vol. 61, No. 6, pp. 2041–2048, 2014.

34. Dundar, C., *Modeling Localized Heating Induced Size Effects in Semiconductor Devices*, Ph.D. Thesis, Bogazici University, 2020.

35. Dundar, C. and N. Donmezer, "Thermal Characterization of Field Plated AlGaN/GaN HEMTs", *2019 18th IEEE Intersociety Conference on Thermal and Thermomechanical Phenomena in Electronic Systems (ITherm)*, pp. 755–760, 2019.

36. Shiga, T., D. Aketo, L. Feng and J. Shiomi, "Thermal Conductivity Spectrum Calculation from First-Principles-based Harmonic Phonon Theory", *Arxiv*, Vol. 201903, pp. 3–8, 2016.

37. Abstreiter, G., "Micro-Raman Spectroscopy for Characterization of Semiconductor Devices", *Applied Surface Science*, Vol. 50, No. 1-4, pp. 73–78, 1991.

38. Cahill, D. G., "Thermal Conductivity Measurement by Time-Domain Thermoreflectance", *MRS Bulletin*, Vol. 43, No. 10, pp. 782–789, 2018.

39. Jiang, P., X. Qian and R. Yang, "Tutorial: Time-Domain Thermoreflectance (TDTR) for Thermal Property Characterization of Bulk and Thin Film Materials", *Journal of Applied Physics*, Vol. 124, No. 16, pp. 1–31, 2018.

40. Yang, J., E. Ziade and A. J. Schmidt, "Uncertainty Analysis of Thermoreflectance Measurements", *Review of Scientific Instruments*, Vol. 87, No. 1, pp. 1–11, 2016.

41. Zhu, J., D. Tang, W. Wang, J. Liu, K. W. Holub and R. Yang, "Ultrafast Thermoreflectance Techniques for Measuring Thermal Conductivity and Interface Thermal Conductance of Thin Films", *Journal of Applied Physics*, Vol. 108, No. 9, pp. 1–8, 2010.

42. Cahill, D. G., "Thermal Conductivity Measurement from 30 to 750 K: The 3$\omega$ Method", *Review of Scientific Instruments*, Vol. 61, No. 2, pp. 802–808, 1990.

43. Cahill, D. G., A. Bullen and S. M. Lee, "Interface thermal conductance and the thermal conductivity of multilayer thin films", *High Temperatures - High Pressures*, Vol. 32, No. 2, pp. 135–142, 2000.

44. Dames, C., "Measuring the Thermal Conductivity of Thin Films: 3 Omega and Related Electrothermal Methods", *Annual Review of Heat Transfer*, Vol. 16, No. 1, pp. 7–49, 2013.

45. Wang, H. and M. Sen, "Analysis of the 3-omega method for thermal conductivity measurement", *International Journal of Heat and Mass Transfer*, Vol. 52, No. 7, pp. 2102–2109, 2009.

46. Fan, H., H. Wu, L. Lindsay and Y. Hu, "Ab Initio Investigation of Single-Layer High Thermal Conductivity Boron Compounds", *Physical Review B*, Vol. 100, No. 8, pp. 1–14, 2019.

47. Liu, Q., P. Jiang and H. Xiang, "Molecular Dynamics Study on Thermal Conductivity of Porous Argon Thin Films", *Chinese Journal of Computational Physics*, Vol. 25, No. 4, pp. 457–462, 2008.

48. Xu, X., J. Chen and B. Li, "Phonon Thermal Conduction in Novel 2D Materials", *Journal of Physics Condensed Matter*, Vol. 28, No. 48, pp. 1–20, 2016.

49. Zhang, W., T. S. Fisher and N. Mingo, "The Atomistic Green's Function Method: An Efficient Simulation Approach for Nanoscale Phonon Transport", *Numerical Heat Transfer, Part B: Fundamentals*, Vol. 51, No. 4, pp. 333–349, 2007.

50. Sadasivam, S., Y. Che, Z. Huang, L. Chen, S. Kumar and T. S. Fisher, "The Atomistic Green's Function Method for Interfacial Phonon Transport", *Annual Review of Heat Transfer*, Vol. 17, pp. 89–145, 2014.

51. Broido, D. A., M. Malorny, G. Birner, N. Mingo and D. A. Stewart, "Intrinsic Lattice Thermal Conductivity of Semiconductors from First Principles", *Applied Physics Letters*, Vol. 91, No. 23, pp. 19–22, 2007.

52. Lindsay, L., D. A. Broido and T. L. Reinecke, "Ab Initio Thermal Transport in Compound Semiconductors", *Physical Review B*, Vol. 87, No. 16, pp. 1–15, April 2013.

53. Lindsay, L., C. Hua, X. L. Ruan and S. Lee, "Survey of Ab Initio Phonon Thermal Transport", *Materials Today Physics*, Vol. 7, pp. 106–120, 2018.

54. Gholivand, H. and N. Donmezer, "Phonon Mean Free Path in Few Layer Graphene, Hexagonal Boron Nitride, and Composite Bilayer h-BN/Graphene", *IEEE Transactions on Nanotechnology*, Vol. 16, No. 5, pp. 752–758, 2017.

55. Chen, J., G. Zhang and L. Baowen, "Molecular Dynamics Simulations for Computing Thermal Conductivity of Nanomaterials", G. Zhang (Editor), *Nanoscale Energy Transport and Harvesting: A Computational Study*, chap. 1, pp. 1–44, Pan Stanford Publishing, Boca Raton, FL, 2015.

56. Kong, L. T., "Phonon Dispersion Measured Directly from Md molecular dynamics simulations", *Computer Physics Communications*, Vol. 182, No. 10, pp. 2201–2207, 2011.

57. Wen, M., S. N. Shirodkar, P. Plecháč, E. Kaxiras, R. S. Elliott and E. B. Tadmor, "A Force-Matching Stillinger-Weber Potential for MoS2: Parameterization and Fisher information Theory Based Sensitivity Analysis", *Journal of Applied Physics*, Vol. 122, No. 24, pp. 1–12, 2017.

58. Vaziri, S., E. Yalon, M. M. Rojo, S. V. Suryavanshi, H. Zhang, C. J. McClellan, C. S. Bailey, K. K. Smithe, A. J. Gabourie, V. Chen, S. Deshmukh, L. Bendersky, A. V. Davydov and E. Pop, "Ultrahigh Thermal Isolation across Heterogeneously Layered Two-Dimensional Materials", *Science Advances*, Vol. 5, No. 8, pp. 1–8,

2019.

59. Warzoha, R. J., A. A. Wilson, B. F. Donovan, N. Donmezer, A. Giri, P. E. Hopkins, S. Choi, D. Pahinkar, J. Shi, S. Graham *et al.*, "Applications and Impacts of Nanoscale Thermal Transport in Electronics Packaging", *Journal of Electronic Packaging*, Vol. 143, No. 2, p. 020804, 2021.

60. Yalon, E., C. J. McClellan, K. K. Smithe, M. Muñoz Rojo, R. L. Xu, S. V. Suryavanshi, A. J. Gabourie, C. M. Neumann, F. Xiong, A. B. Farimani and E. Pop, "Energy Dissipation in Monolayer MoS2 Electronics", *Nano Letters*, Vol. 17, No. 6, pp. 3429–3433, 2017.

61. Mitterhuber, L., R. Hammer, T. Dengg and J. Spitaler, "Thermal Characterization and Modelling of AlGaN-GaN Multilayer Structures for HEMT Applications", *Energies*, Vol. 13, No. 9, pp. 1–17, 2020.

62. Wang, X. and B. Huang, "Computational Study of In-Plane Phonon Transport in Si Thin Films", *Scientific Reports*, Vol. 4, No. 1, pp. 1–10, 2014.

63. Chatterjee, B., C. Dundar, T. E. Beechem, E. Heller, D. Kendig, H. Kim, N. Donmezer and S. Choi, "Nanoscale Electrothermal Interactions in AlGaN/GaN High Electron Mobility Transistors", *Journal of Applied Physics*, Vol. 127, No. 4, pp. 1–13, 2020.

64. Donmezer, F. N., M. Islam, S. Graham and D. Yoder, "Modeling the Hotspot Temperature in AlGaN/GaN High Electron Mobility Transistors Using a Non-Gray Phonon BTE Solver", *ASME International Mechanical Engineering Congress and Exposition*, Vol. 9, pp. 1175–1188, 11 2012.

65. Xu, C., S. K. Kolluri, K. Endo and K. Banerjee, "Analytical Thermal Model for Self-Heating in Advanced FinFET Devices With Implications for Design and Reliability", *IEEE Transactions on Computer-Aided Design of Integrated Circuits and Systems*, Vol. 32, No. 7, pp. 1045–1058, 2013.

66. Chen, G., "Phonon Wave Heat Conduction in Thin Films and Superlattices", *Journal of Heat Transfer*, Vol. 121, No. 4, pp. 945–953, 1999.

67. Haitao, W., X. Yibin, M. Shimono, Y. Tanaka and M. Yamazaki, "Molecular Dynamics Simulation of Thermal Conductivity of Silicon Thin film", *Materials Transactions*, Vol. 48, No. 9, pp. 2419–2421, 2007.

68. Sparavigna, A. C., "Relaxation Time Approximation-I-Theory. Mechanics", *Materials Science Engineering Journal*, , No. 3, pp. 1–13, 2016.

69. Frenkel, D. and B. Smit, *Understanding Molecular Simulation: From Algorithms to Applications*, Vol. 1, Elsevier, 2001.

70. Mobaraki, A., A. Kandemir, H. Yapicioglu, O. Gülseren and C. Sevik, "Validation of Interatomic Potential for WS2 and WSe2 Crystals through Assessment of Thermal Transport Properties", *Computational Materials Science*, Vol. 144, pp. 92–98, 2018.

71. Zhou, X. W., S. Aubry, R. E. Jones, A. Greenstein and P. K. Schelling, "Towards More Accurate Molecular Dynamics Calculation of Thermal Conductivity: Case study of GaN Bulk Crystals", *Physical Review B*, Vol. 79, No. 11, pp. 1–17, March 2009.

72. White, J. A., F. L. Román, A. González and S. Velasco, "Periodic Boundary Conditions and the Correct Molecular Dynamics Ensemble", *Physica A: Statistical Mechanics and its Applications*, Vol. 387, No. 27, pp. 6705–6711, 2008.

73. Schelling, P. K., S. R. Phillpot and P. Keblinski, "Comparison of Atomic-Level Simulation Methods for Computing Thermal conductivity", *Physical Review B*, Vol. 65, No. 14, pp. 1–12, 2002.

74. Verlet, L., "Computer "Experiments" on Classical Fluids. I. Thermodynamical Properties of Lennard-Jones Molecules", *Physical Review A*, Vol. 159, No. 1, pp.

98–103, 1967.

75. Oligschleger, C., J. C. Schön and J. C. Schö, "Simulation of Thermal Conductivity and Heat Transport in Solids", *Physical Review B*, Vol. 59, No. 6, pp. 4125–4133, 1999.

76. Li, Z., S. Xiong, C. Sievers, Y. Hu, Z. Fan, N. Wei, H. Bao, S. Chen, D. Donadio and T. Ala-Nissila, "Influence of Thermostatting on Nonequilibrium Molecular Dynamics Simulations of Heat Conduction in Solids", *Journal of Chemical Physics*, Vol. 151, No. 23, pp. 1–12, 2019.

77. Cao, B. Y., "Nonequilibrium Molecular Dynamics Calculation of the Thermal Conductivity based on an Improved Relaxation Scheme", *Journal of Chemical Physics*, Vol. 129, No. 7, pp. 1–8, 2008.

78. Sellan, D. P., E. S. Landry, J. E. Turney, A. J. McGaughey and C. H. Amon, "Size Effects in Molecular Dynamics Thermal Conductivity Predictions", *Physical Review B*, Vol. 81, No. 21, pp. 1–10, 2010.

79. Lampin, E., Q. H. Nguyen, P. A. Francioso and F. Cleri, "Thermal Boundary Resistance at Silicon-Silica Interfaces by Molecular Dynamics Simulations", *Applied Physics Letters*, Vol. 100, No. 13, pp. 1–4, 2012.

80. Melis, C., R. Dettori, S. Vandermeulen and L. Colombo, "Calculating Thermal Conductivity in a Transient Conduction Regime: Theory and Implementation", *European Physical Journal B*, Vol. 87, No. 4, pp. 1–9, 2014.

81. Zhu, W., G. Zheng, S. Cao and H. He, "Thermal Conductivity of Amorphous SiO2 Thin Film: A Molecular Dynamics Study", *Scientific Reports*, Vol. 8, No. 1, pp. 1–9, 2018.

82. Liang, Z., A. Jain, A. J. McGaughey and P. Keblinski, "Molecular Simulations and Lattice Dynamics Determination of Stillinger-Weber GaN Thermal Conduc-

tivity", *Journal of Applied Physics*, Vol. 118, No. 12, pp. 1–5, September 2015.

83. Huang, Z., Z. Tang, J. Yu and S. Bai, "Thermal Conductivity of Amorphous and Crystalline Thin Films by Molecular Dynamics Simulation", *Physica B*, Vol. 404, No. 12-13, pp. 1790–1793, 2009.

84. Stevens, R. J., L. V. Zhigilei and P. M. Norris, "Effects of Temperature and Disorder on Thermal Boundary Conductance at Solid-Solid ınterfaces: Nonequilibrium Molecular Dynamics Simulations", *International Journal of Heat and Mass Transfer*, Vol. 50, No. 19-20, pp. 3977–3989, 2007.

85. Wei, Z., Z. Yang, M. Liu, H. Wu, Y. Chen and F. Yang, "Thermal Boundary Conductance between High Thermal Conductivity Boron Arsenide and Silicon", *Journal of Applied Physics*, Vol. 127, No. 5, pp. 1–7, 2020.

86. Lampin, E., P. L. Palla, P. A. Francioso and F. Cleri, "Thermal Conductivity from Approach-to-Equilibrium Molecular Dynamics", *Journal of Applied Physics*, Vol. 114, No. 3, pp. 1–5, 2013.

87. Zaoui, H., P. L. Palla, F. Cleri and E. Lampin, "Length Dependence of Thermal Conductivity by Approach-to-Equilibrium Molecular Dynamics", *Physical Review B*, Vol. 94, No. 5, pp. 1–9, 2016.

88. Barbarino, G., C. Melis and L. Colombo, "Intrinsic Thermal Conductivity in Monolayer Graphene is Ultimately Upper Limited: A Direct Estimation by Atomistic Simulations", *Physical Review B - Condensed Matter and Materials Physics*, Vol. 91, No. 3, pp. 1–4, 2015.

89. Parlinski, K., "Lattice Dynamics: Vibrational Modes", F. Bassani, G. L. Liedl and P. Wyder (Editors), *Encyclopedia of Condensed Matter Physics*, pp. 98–102, Elsevier, Oxford, 2005.

90. Togo, A., L. Chaput and I. Tanaka, "Distributions of Phonon Lifetimes in Bril-

louin Zones", *Physical Review B - Condensed Matter and Materials Physics*, Vol. 91, No. 9, pp. 1–31, January 2015.

91. Kunc, K. and P. G. Dacosta, "Real-Space Convergence of the Force Series in the Lattice Dynamics of Germanium", *Physical Review B*, Vol. 32, No. 4, pp. 2010–2021, 1985.

92. Wei, S. and M. Y. Chou, "Ab Initio Calculation of Force Constants and Full Phonon Dispersions", *Physical Review Letters*, Vol. 69, No. 19, pp. 2799–2802, 1992.

93. Baroni, S., S. de Gironcoli and A. D. Corso, "Phonons and Related Crystal Properties from Density-Functional Perturbation Theory", *Review of Modern Physics*, Vol. 73, No. 2, pp. 515 – 562, 2001.

94. Baroni, S., P. Giannozzi and A. Testa, "Green's-Function Approach to Linear Response in Solids", *Physical Review Letters*, Vol. 58, No. 18, pp. 1861–1864, May 1987.

95. Gonze, X., "First-Principles Responses of Solids to Atomic Displacements and Homogeneous Electric Fields: Implementation of a Conjugate-Gradient Algorithm", *Physical Review B*, Vol. 55, No. 16, pp. 10337–10354, 1997.

96. Fultz, B., "Vibrational Thermodynamics of Materials", *Progress in Materials Science*, Vol. 55, No. 4, pp. 247–352, 2010.

97. Bellissima, S., M. Neumann, E. Guarini, U. Bafile and F. Barocchi, "Density of States and Dynamical Crossover in a Dense Fluid Revealed by Exponential Mode Analysis of the Velocity Autocorrelation Function", *Physical Review E*, Vol. 95, No. 1, pp. 1–14, 2017.

98. Croxton, C. A. and R. P. Ferrier, "Statistical Mechanical Calculation of Surface Properties of Simple Liquids. IV. Molecular dynamics", *Journal of Physics C:*

*Solid State Physics*, Vol. 4, No. 16, pp. 2447–2456, 1971.

99. Raymand, D., T. J. Jacobsson, K. Hermansson and T. Edvinsson, "Investigation of Vibrational Modes and Phonon Density of States in ZnO Quantum Dots", *The Journal of Physical Chemistry C*, Vol. 116, No. 12, pp. 6893–6901, March 2012.

100. in't Veld, P. J., S. Plimpton and G. S. Grest, "Accurate and Efficient Methods for Modeling Colloidal Mixtures in an Explicit Solvent using Molecular Dynamics", *Computer Physics Communications*, Vol. 179, pp. 320–329, 2008.

101. Plimpton, S., "Fast Parallel Algorithms for Short-Range Molecular Dynamics", *Journal of Computational Physics*, Vol. 117, No. 6, pp. 1–42, 1997.

102. Plimpton, S., P. Crozier and A. Thompson, "LAMMPS-Large-Scale Atomic/Molecular Massively Parallel Simulator", *Sandia National Laboratories*, Vol. 18, p. 43, 2007.

103. Campaná, C. and M. H. Müser, "Practical Green's Function Approach to the Simulation of Elastic Semi-Infinite Solids", *Physical Review B*, Vol. 74, No. 7, pp. 1–16, 2006.

104. Campañá, C., M. H. Müser, C. Denniston, Y. Qi, T. A. Perry, C. Campaná, M. H. Müser, C. Denniston, Y. Qi and T. A. Perry, "Elucidating the Contact Mechanics of Aluminum Silicon Surfaces with Green's function Molecular Dynamics", *Journal of Applied Physics*, Vol. 102, No. 11, pp. 1–11, 2007.

105. Kong, L. T., G. Bartels, C. Campañá, C. Denniston and M. H. Müser, "Implementation of Green's Function Molecular Dynamics: An Extension to LAMMPS", *Computer Physics Communications*, Vol. 180, No. 6, pp. 1004–1010, 2009.

106. Lekien, F. and J. Marsden, "Tricubic Interpolation in Three Dimensions", *International Journal for Numerical Methods in Engineering*, Vol. 63, No. 3, pp. 455–471, 2005.

107. Regner, K. T., D. P. Sellan, Z. Su, C. H. Amon, A. J. McGaughey and J. A. Malen, "Broadband Phonon Mean Free Path Contributions to Thermal Conductivity Measured using Frequency Domain Thermoreflectance", *Nature Communications*, Vol. 4, pp. 1–7, 2013.

108. Henry, A. and G. Chen, "Spectral Phonon Transport Properties of Silicon Based on Molecular Dynamics Simulations and Lattice Dynamics", *Journal of Computational and Theoretical Nanoscience*, Vol. 5, No. 1, pp. 1–12, 2008.

109. Chang, T. M., C. C. Weng and M. J. Huang, "A Nonequilibrium Molecular Dynamics Study of In-Plane Thermal Conductivity of Silicon Thin Films", *Journal of Electronic Materials*, Vol. 39, No. 9, pp. 1616–1620, 2010.

110. Stillinger, F. H. and T. A. Weber, "Computer Simulation of Local Order in Condensed Phases of Silicon", *Physical Review B*, Vol. 31, No. 8, pp. 5262–5271, 1985.

111. Béré, A. and A. Serra, "Atomic Structure of Dislocation Cores in GaN", *Physical Review B*, Vol. 65, No. 20, pp. 1–10, 2002.

112. Béré, A. and A. Serra, "On the Atomic Structures, Mobility and Interactions of Extended Defects in GaN: Dislocations, Tilt and Twin Boundaries", *Philosophical Magazine*, Vol. 86, No. 15, pp. 2159–2192, 2006.

113. Vashishta, P., R. K. Kalia, A. Nakano and J. P. Rino, "Interaction Potential for Aluminum Nitride: A Molecular Dynamics Study of Mechanical and Thermal Properties of Crystalline and Amorphous Aluminum Nitride", *Journal of Applied Physics*, Vol. 109, No. 3, pp. 1–8, 2011.

114. Liang, Z., K. Sasikumar and P. Keblinski, "Thermal Transport across a Substrate-Thin Film Interface: Effects of Film Thickness and Surface roughness", *Physical Review Letters*, Vol. 113, No. 6, pp. 1–5, 2014.

115. Hu, L., W. J. Evans and P. Keblinski, "One-Dimensional Phonon Effects in Direct Molecular Dynamics Method for Thermal Conductivity determination", *Journal of Applied Physics*, Vol. 110, No. 11, pp. 1–7, 2011.

116. Romano, G., A. Di Carlo and J. C. Grossman, "Mesoscale Modeling of Phononic Thermal Conductivity of Porous Si: Interplay Between Porosity, Morphology and Surface Roughness", *Journal of Computational Electronics*, Vol. 11, No. 1, pp. 8–13, 2012.

117. Wang, Z., X. Tian, J. Liang, J. Zhu, D. Tang and K. Xu, "Prediction and Measurement of Thermal Transport across Interfaces between Semiconductor and Adjacent Layers", *International Journal of Thermal Sciences*, Vol. 79, pp. 266–275, 2014.

118. Jezowski, A., B. A. Danilchenko, M. Boćkowski, I. Grzegory, S. Krukowski, T. Suski and T. Paszkiewicz, "Thermal Conductivity of GaN Crystals in 4.2-300 K Range", *Solid State Communications*, Vol. 128, No. 2-3, pp. 69–73, 2003.

119. Shiga, T., D. Aketo, L. Feng and J. Shiomi, "Harmonic Phonon Theory for Calculating Thermal Conductivity Spectrum from First-Principles Dispersion Relations", *Applied Physics Letters*, Vol. 108, No. 20, pp. 1–5, 2016.

120. Shulumba, N., Z. Raza, O. Hellman, E. Janzén, I. A. Abrikosov and M. Odén, "Impact of Anharmonic Effects on the Phase Stability, Thermal Transport, and Electronic Properties of AlN", *Physical Review B*, Vol. 94, No. 10, pp. 1–8, 2016.

121. Slack, G. A., L. J. Schowalter, D. Morelli and J. A. Freitas, "Some Effects of Oxygen Impurities on AlN and GaN", *Journal of Crystal Growth*, Vol. 246, pp. 287–298, December 2002.

122. Xu, R. L., M. Muñoz Rojo, S. M. Islam, A. Sood, B. Vareskic, A. Katre, N. Mingo, K. E. Goodson, H. G. Xing, D. Jena and E. Pop, "Thermal Conductivity of Crystalline AlN and the Influence of Atomic-Scale Defects", *Journal of Applied*

*Physics*, Vol. 126, No. 18, pp. 1–8, 2019.

123. Kawamura, T., Y. Kangawa and K. Kakimoto, "Investigation of Thermal Conductivity of GaN by Molecular Dynamics", *Journal of Crystal Growth*, Vol. 284, No. 1, pp. 197–202, October 2005.

124. Albar, I., *Phonon Mean Free Path and Thermal Conductivity Analysis of Wide and Ultra-Wide Bandgap Materials*, Ph.D. Thesis, Bogazici University, 2020.

125. Lindsay, L., D. A. Broido, J. Carrete, N. Mingo and T. L. Reinecke, "Anomalous Pressure Dependence of Thermal Conductivities of Large Mass Ratio compounds", *Physical Review B*, Vol. 91, No. 12, pp. 1–5, 2015.

126. McGaughey, A. J., M. I. Hussein, E. S. Landry, M. Kaviany and G. M. Hulbert, "Phonon Band Structure and Thermal Transport Correlation in a Layered Diatomic Crystal", *Physical Review B*, Vol. 74, No. 10, pp. 1–30, 2006.

127. Das, S., M. Kim, J. W. Lee and W. Choi, "Synthesis, Properties, and Applications of 2-D Materials: A Comprehensive Review", *Critical Reviews in Solid State and Materials Sciences*, Vol. 39, No. 4, pp. 231–252, 2014.

128. Izyumskaya, N., D. O. Demchenko, S. Das, Ü. Özgür, V. Avrutin and H. Morkoç, "Recent Development of Boron Nitride towards Electronic Applications", *Advanced Electronic Materials*, Vol. 3, No. 5, pp. 1–22, 2017.

129. Bao, J., K. Jeppson, M. Edwards, Y. Fu, L. Ye, X. Lu and J. Liu, "Synthesis and Applications of Two-Dimensional Hexagonal Boron Nitride in Electronics Manufacturing", *Electronic Materials Letters*, Vol. 12, No. 1, pp. 1–16, 2016.

130. Alam, M. T., M. S. Bresnehan, J. A. Robinson and M. A. Haque, "Thermal Conductivity of Ultra-Thin Chemical Vapor Deposited Hexagonal Boron Nitride Films", *Applied Physics Letters*, Vol. 104, No. 1, pp. 1–6, 2014.

131. Sheng, Y., T. Chen, Y. Lu, R. J. Chang, S. Sinha and J. H. Warner, "High-Performance WS2 Monolayer Light-Emitting Tunneling Devices Using 2D Materials Grown by Chemical Vapor Deposition", *ACS Nano*, Vol. 13, No. 4, pp. 4530–4537, 2019.

132. Hu, Y., L. Zeng, A. J. Minnich, M. S. Dresselhaus and G. Chen, "Spectral Mapping of Thermal Conductivity through Nanoscale Ballistic Transport", *Nature Nanotechnology*, Vol. 10, No. 8, pp. 701–706, 2015.

133. Schwierz, F., J. Pezoldt and R. Granzner, "Two-Dimensional Materials and Their Prospects in Transistor Electronics", *Nanoscale*, Vol. 7, No. 18, pp. 8261–8283, 2015.

134. Komarov, P. V., Y. T. Chiu, S. M. Chen, P. G. Khalatur and P. Reineker, "Highly Cross-Linked Epoxy Resins: An Atomistic Molecular Dynamics Simulation Combined with a Mapping/Reverse Mapping Procedure", *Macromolecules*, Vol. 40, No. 22, pp. 8104–8113, 2007.

135. Jiang, J. W., H. S. Park and T. Rabczuk, "Molecular Dynamics Simulations of Single-Layer Molybdenum Disulphide (MoS2): Stillinger-Weber Parametrization, Mechanical Properties, and Thermal Conductivity", *Journal of Applied Physics*, Vol. 114, No. 6, pp. 1–12, 2013.

136. Tersoff, J., "Empirical Interatomic Potential for Silicon with Improved Elastic Properties", *Physical Review B*, Vol. 38, No. 14, pp. 9902–9905, 1988.

137. Tersoff, J., "Erratum: Modeling Solid-State Chemistry: Interatomic Potentials for Multicomponent Systems [Phys. Rev. B39, 5566 (1989)", *Physical Review B*, Vol. 41, No. 5, p. 3248, 1990.

138. Nord, J., K. Albe, P. Erhart and K. Nordlund, "Modelling of Compound semiconductors: Analytical Bond-Order Potential for Gallium, Nitrogen and Gallium Nitride", *Journal of Physics Condensed Matter*, Vol. 15, No. 32, pp. 5649–5662,

2003.

139. Munetoh, S., T. Motooka, K. Moriguchi and A. Shintani, "Interatomic Potential for Si-O systems using Tersoff Parameterization", *Computational Materials Science*, Vol. 39, No. 2, pp. 334–339, 2007.

140. Los, J. H., J. M. Kroes, K. Albe, R. M. Gordillo, M. I. Katsnelson and A. Fasolino, "Extended Tersoff potential for boron nitride: Energetics and elastic properties of pristine and defective h -BN", *Physical Review B*, Vol. 96, No. 18, pp. 1–11, 2017.

141. Rappi, A. K., C. J. Casewit, K. S. Colwell, W. Goddard and W. M. Skid, "UFF, a Full Periodic Table Force Field for Molecular Mechanics and Molecular Dynamics Simulations", *Journal of the American Chemical Society*, Vol. 114, pp. 24–39, 1992.

142. Ding, Z., Q. X. Pei, J. W. Jiang and Y. W. Zhang, "Manipulating the Thermal Conductivity of Monolayer MoS2 via Lattice Defect and Strain Engineering", *Journal of Physical Chemistry C*, Vol. 119, No. 28, pp. 16358–16365, 2015.

143. Koukaras, E. N., G. Kalosakas, C. Galiotis and K. Papagelis, "Phonon Properties of Graphene Derived from Molecular Dynamics Simulations", *Scientific Reports*, Vol. 5, No. 1, pp. 1–9, 2015.

144. Molina-Sánchez, A. and L. Wirtz, "Phonons in Single-Layer and Few-Layer MoS2 and WS2", *Physical Review B - Condensed Matter and Materials Physics*, Vol. 84, No. 15, pp. 1–8, 2011.

145. Sengupta, A., A. Chanana and S. Mahapatra, "Phonon Scattering Limited Performance of Monolayer MoS2 and WSe2 n-MOSFET", *AIP Advances*, Vol. 5, No. 2, pp. 1–9, 2015.

146. Kaya, O. and N. Donmezer, "Investigation of the Thermal Conductivity of Ma-

terials in 2D/3D Heterostructures", *2021 IEEE 21st International Conference on Nanotechnology (NANO)*, pp. 374–377, Montreal, 2021.

147. Polanco, C. A. and L. Lindsay, "Phonon Thermal Conductance across GaN-AlN Interfaces from First Principles", *Physical Review B*, Vol. 99, No. 7, pp. 1–31, 2019.

148. Islam, M. S., I. Mia, S. Ahammed, C. Stampfl and J. Park, "Exceptional In-Plane and Interfacial Thermal Transport in Graphene/2D-SiC van der Waals Heterostructures", *Scientific Reports*, Vol. 10, No. 1, pp. 1–16, 2020.

149. Venkatachalam, A., W. T. James and S. Graham, "Electrothermomechanical Modeling of GaN-based HFETs and MOSHFETs", *Semiconductor Science and Technology*, Vol. 26, No. 8, pp. 1–6, 2011.

150. Donmezer, F. N., D. Singh, W. James, A. Christensen, S. Graham and J. Y. Murthy, "Lattice Boltzmann and Discrete Ordinates Methods for Phonon Transport Modeling: A Comparative Study", pp. 333–343, November 2011.

151. Nasri, F., F. Echouchene, M. F. Ben Aissa, I. Graur and H. Belmabrouk, "Investigation of Self-Heating Effects in a 10-nm SOI-MOSFET With an Insulator Region Using Electrothermal Modeling", *IEEE Transactions on Electron Devices*, Vol. 62, No. 8, pp. 2410–2415, 2015.

152. Heino, P., "Dispersion and Thermal Resistivity in Silicon Nanofilms by Molecular Dynamics", *European Physical Journal B*, Vol. 60, No. 2, pp. 171–179, 2007.

# APPENDIX A: COPYRIGHT PERMISSIONS



SPRINGER NATURE LICENSE
TERMS AND CONDITIONS

Aug 26, 2021

---

This Agreement between Mr. Onurcan Kaya ("You") and Springer Nature ("Springer Nature") consists of your license details and the terms and conditions provided by Springer Nature and Copyright Clearance Center.

| | |
|---|---|
| License Number | 5136500889973 |
| License date | Aug 26, 2021 |
| Licensed Content Publisher | Springer Nature |
| Licensed Content Publication | Nature Materials |
| Licensed Content Title | Quasi-ballistic thermal transport from nanoscale interfaces observed using ultrafast coherent soft X-ray beams |
| Licensed Content Author | Mark E. Siemens et al |
| Licensed Content Date | Nov 8, 2009 |
| Type of Use | Thesis/Dissertation |
| Requestor type | academic/university or research institute |
| Format | print and electronic |
| Portion | figures/tables/illustrations |
| Number of figures/tables/illustrations | 1 |

| | |
|---|---|
| High-res required | no |
| Will you be translating? | no |
| Circulation/distribution | 1 - 29 |
| Author of this Springer Nature content | no |
| Title | Understanding the Ballistic-Diffusive Thermal Transport Trends in Crystalline Semiconductors with Molecular Dynamics |
| Institution name | Bogazici University |
| Expected presentation date | Sep 2021 |
| Portions | Figure 1.4 |
| Requestor Location | Mr. Onurcan Kaya<br>Bogazici University South Campus Enginee<br>Bebek/Besiktas<br><br>Istanbul, Turkey 34342<br>Turkey<br>Attn: Bogazici University |
| Total | 0.00 USD |

Terms and Conditions

**Springer Nature Customer Service Centre GmbH**
**Terms and Conditions**

This agreement sets out the terms and conditions of the licence (the **Licence**) between you and **Springer Nature Customer Service Centre GmbH** (the **Licensor**). By clicking 'accept' and completing the transaction for the material (**Licensed Material**), you also confirm your acceptance of these terms and conditions.

**1. Grant of License**

**1. 1.** The Licensor grants you a personal, non-exclusive, non-transferable, world-wide licence to reproduce the Licensed Material for the purpose specified in your order only. Licences are granted for the specific use requested in the order and for no other use, subject to the conditions below.

**1. 2.** The Licensor warrants that it has, to the best of its knowledge, the rights to license reuse of the Licensed Material. However, you should ensure that the material you are requesting is original to the Licensor and does not carry the copyright of another entity (as credited in the published version).

**1. 3.** If the credit line on any part of the material you have requested indicates that it was reprinted or adapted with permission from another source, then you should also seek permission from that source to reuse the material.

**2. Scope of Licence**

**2. 1.** You may only use the Licensed Content in the manner and to the extent permitted by these Ts&Cs and any applicable laws.

**2. 2.** A separate licence may be required for any additional use of the Licensed Material, e.g. where a licence has been purchased for print only use, separate permission must be obtained for electronic re-use. Similarly, a licence is only valid in the language selected and does not apply for editions in other languages unless additional translation rights have been granted separately in the licence. Any content owned by third parties are expressly excluded from the licence.

**2. 3.** Similarly, rights for additional components such as custom editions and derivatives require additional permission and may be subject to an additional fee. Please apply to Journalpermissions@springernature.com/bookpermissions@springernature.com for these rights.

**2. 4.** Where permission has been granted **free of charge** for material in print, permission may also be granted for any electronic version of that work, provided that the material is incidental to your work as a whole and that the electronic version is essentially equivalent to, or substitutes for, the print version.

**2. 5.** An alternative scope of licence may apply to signatories of the STM Permissions Guidelines, as amended from time to time.

**3. Duration of Licence**

**3. 1.** A licence for is valid from the date of purchase ('Licence Date') at the end of the relevant period in the below table:

| **Scope of Licence** | **Duration of Licence** |
|---|---|
| Post on a website | 12 months |
| Presentations | 12 months |
| Books and journals | Lifetime of the edition in the language purchased |

**4. Acknowledgement**

**4. 1.** The Licensor's permission must be acknowledged next to the Licenced Material in print. In electronic form, this acknowledgement must be visible at the same time as the figures/tables/illustrations or abstract, and must be hyperlinked to the journal/book's homepage. Our required acknowledgement format is in the Appendix below.

**5. Restrictions on use**

**5. 1.** Use of the Licensed Material may be permitted for incidental promotional use and minor editing privileges e.g. minor adaptations of single figures, changes of format, colour and/or style where the adaptation is credited as set out in Appendix 1 below. Any other changes including but not limited to, cropping, adapting, omitting material that affect the meaning, intention or moral rights of the author are strictly prohibited.

**5. 2.** You must not use any Licensed Material as part of any design or trademark.

**5. 3.** Licensed Material may be used in Open Access Publications (OAP) before publication by Springer Nature, but any Licensed Material must be removed from OAP sites prior to final publication.

**6. Ownership of Rights**

**6. 1.** Licensed Material remains the property of either Licensor or the relevant third party and any rights not explicitly granted herein are expressly reserved.

**7. Warranty**

IN NO EVENT SHALL LICENSOR BE LIABLE TO YOU OR ANY OTHER PARTY OR ANY OTHER PERSON OR FOR ANY SPECIAL, CONSEQUENTIAL, INCIDENTAL OR INDIRECT DAMAGES, HOWEVER CAUSED, ARISING OUT OF OR IN CONNECTION WITH THE DOWNLOADING, VIEWING OR USE OF THE MATERIALS REGARDLESS OF THE FORM OF ACTION, WHETHER FOR BREACH OF CONTRACT, BREACH OF WARRANTY, TORT, NEGLIGENCE, INFRINGEMENT OR OTHERWISE (INCLUDING, WITHOUT LIMITATION, DAMAGES BASED ON LOSS OF PROFITS, DATA, FILES, USE, BUSINESS OPPORTUNITY OR CLAIMS OF THIRD PARTIES), AND
WHETHER OR NOT THE PARTY HAS BEEN ADVISED OF THE POSSIBILITY OF SUCH DAMAGES. THIS LIMITATION SHALL APPLY NOTWITHSTANDING ANY FAILURE OF ESSENTIAL PURPOSE OF ANY LIMITED REMEDY PROVIDED HEREIN.

**8. Limitations**

**8. 1.** ***BOOKS ONLY:*** Where **'reuse in a dissertation/thesis'** has been selected the following terms apply: Print rights of the final author's accepted manuscript (for clarity,

NOT the published version) for up to 100 copies, electronic rights for use only on a personal website or institutional repository as defined by the Sherpa guideline (www.sherpa.ac.uk/romeo/).

**8. 2.** For content reuse requests that qualify for permission under the STM Permissions Guidelines, which may be updated from time to time, the STM Permissions Guidelines supersede the terms and conditions contained in this licence.

**9. Termination and Cancellation**

**9. 1.** Licences will expire after the period shown in Clause 3 (above).

**9. 2.** Licensee reserves the right to terminate the Licence in the event that payment is not received in full or if there has been a breach of this agreement by you.

**Appendix 1 — Acknowledgements:**

**For Journal Content:**
Reprinted by permission from [**the Licensor**]: [**Journal Publisher** (e.g. Nature/Springer/Palgrave)] [**JOURNAL NAME**] [**REFERENCE CITATION** (Article name, Author(s) Name), [**COPYRIGHT**] (year of publication)

For **Advance Online Publication papers:**
Reprinted by permission from [**the Licensor**]: [**Journal Publisher** (e.g. Nature/Springer/Palgrave)] [**JOURNAL NAME**] [**REFERENCE CITATION** (Article name, Author(s) Name), [**COPYRIGHT**] (year of publication), advance online publication, day month year (doi: 10.1038/sj.[JOURNAL ACRONYM].)

**For Adaptations/Translations:**
Adapted/Translated by permission from [**the Licensor**]: [**Journal Publisher** (e.g. Nature/Springer/Palgrave)] [**JOURNAL NAME**] [**REFERENCE CITATION** (Article name, Author(s) Name), [**COPYRIGHT**] (year of publication)

**Note: For any republication from the British Journal of Cancer, the following credit line style applies:**

Reprinted/adapted/translated by permission from [**the Licensor**]: on behalf of Cancer Research UK: : [**Journal Publisher** (e.g. Nature/Springer/Palgrave)] [**JOURNAL NAME**] [**REFERENCE CITATION** (Article name, Author(s) Name), [**COPYRIGHT**] (year of publication)

For **Advance Online Publication** papers:
Reprinted by permission from The [**the Licensor**]: on behalf of Cancer Research UK: [**Journal Publisher** (e.g. Nature/Springer/Palgrave)] [**JOURNAL NAME**] [**REFERENCE CITATION** (Article name, Author(s) Name), [**COPYRIGHT**] (year of publication), advance online publication, day month year (doi: 10.1038/sj.[JOURNAL ACRONYM])

**For Book content:**
Reprinted/adapted by permission from [**the Licensor**]: [**Book Publisher** (e.g.

Palgrave Macmillan, Springer etc) [**Book Title**] by [**Book author**(s)]
[**COPYRIGHT**] (year of publication)

**Other Conditions**:

Version 1.3

**Questions? customercare@copyright.com or +1-855-239-3415 (toll free in the US) or +1-978-646-2777.**

SPRINGER NATURE LICENSE
TERMS AND CONDITIONS

Aug 26, 2021

---

This Agreement between Mr. Onurcan Kaya ("You") and Springer Nature ("Springer Nature") consists of your license details and the terms and conditions provided by Springer Nature and Copyright Clearance Center.

| | |
|---|---|
| License Number | 5136550279497 |
| License date | Aug 26, 2021 |
| Licensed Content Publisher | Springer Nature |
| Licensed Content Publication | Nature Materials |
| Licensed Content Title | Quasi-ballistic thermal transport from nanoscale interfaces observed using ultrafast coherent soft X-ray beams |
| Licensed Content Author | Mark E. Siemens et al |
| Licensed Content Date | Nov 8, 2009 |
| Type of Use | Thesis/Dissertation |
| Requestor type | academic/university or research institute |
| Format | print and electronic |
| Portion | figures/tables/illustrations |
| Number of figures/tables/illustrations | 1 |

| | |
|---|---|
| High-res required | no |
| Will you be translating? | no |
| Circulation/distribution | 1 - 29 |
| Author of this Springer Nature content | no |
| Title | Understanding the Ballistic-Diffusive Thermal Transport Trends in Crystalline Semiconductors with Molecular Dynamics |
| Institution name | Bogazici University |
| Expected presentation date | Sep 2021 |
| Portions | Figure 1.7 |
| Requestor Location | Mr. Onurcan Kaya<br>Bogazici University South Campus Enginee<br>Bebek/Besiktas<br><br>Istanbul, Turkey 34342<br>Turkey<br>Attn: Bogazici University |
| Total | 0.00 USD |

Terms and Conditions

**Springer Nature Customer Service Centre GmbH**
**Terms and Conditions**

This agreement sets out the terms and conditions of the licence (the **Licence**) between you and **Springer Nature Customer Service Centre GmbH** (the **Licensor**). By clicking 'accept' and completing the transaction for the material (**Licensed Material**), you also confirm your acceptance of these terms and conditions.

**1. Grant of License**

**1. 1.** The Licensor grants you a personal, non-exclusive, non-transferable, world-wide licence to reproduce the Licensed Material for the purpose specified in your order only. Licences are granted for the specific use requested in the order and for no other use, subject to the conditions below.

**1. 2.** The Licensor warrants that it has, to the best of its knowledge, the rights to license reuse of the Licensed Material. However, you should ensure that the material you are requesting is original to the Licensor and does not carry the copyright of another entity (as credited in the published version).

**1. 3.** If the credit line on any part of the material you have requested indicates that it was reprinted or adapted with permission from another source, then you should also seek permission from that source to reuse the material.

**2. Scope of Licence**

**2. 1.** You may only use the Licensed Content in the manner and to the extent permitted by these Ts&Cs and any applicable laws.

**2. 2.** A separate licence may be required for any additional use of the Licensed Material, e.g. where a licence has been purchased for print only use, separate permission must be obtained for electronic re-use. Similarly, a licence is only valid in the language selected and does not apply for editions in other languages unless additional translation rights have been granted separately in the licence. Any content owned by third parties are expressly excluded from the licence.

**2. 3.** Similarly, rights for additional components such as custom editions and derivatives require additional permission and may be subject to an additional fee. Please apply to Journalpermissions@springernature.com/bookpermissions@springernature.com for these rights.

**2. 4.** Where permission has been granted **free of charge** for material in print, permission may also be granted for any electronic version of that work, provided that the material is incidental to your work as a whole and that the electronic version is essentially equivalent to, or substitutes for, the print version.

**2. 5.** An alternative scope of licence may apply to signatories of the STM Permissions Guidelines, as amended from time to time.

**3. Duration of Licence**

**3. 1.** A licence for is valid from the date of purchase ('Licence Date') at the end of the relevant period in the below table:

| **Scope of Licence** | **Duration of Licence** |
|---|---|
| Post on a website | 12 months |
| Presentations | 12 months |
| Books and journals | Lifetime of the edition in the language purchased |

**4. Acknowledgement**

**4. 1.** The Licensor's permission must be acknowledged next to the Licenced Material in print. In electronic form, this acknowledgement must be visible at the same time as the figures/tables/illustrations or abstract, and must be hyperlinked to the journal/book's homepage. Our required acknowledgement format is in the Appendix below.

**5. Restrictions on use**

**5. 1.** Use of the Licensed Material may be permitted for incidental promotional use and minor editing privileges e.g. minor adaptations of single figures, changes of format, colour and/or style where the adaptation is credited as set out in Appendix 1 below. Any other changes including but not limited to, cropping, adapting, omitting material that affect the meaning, intention or moral rights of the author are strictly prohibited.

**5. 2.** You must not use any Licensed Material as part of any design or trademark.

**5. 3.** Licensed Material may be used in Open Access Publications (OAP) before publication by Springer Nature, but any Licensed Material must be removed from OAP sites prior to final publication.

**6. Ownership of Rights**

**6. 1.** Licensed Material remains the property of either Licensor or the relevant third party and any rights not explicitly granted herein are expressly reserved.

**7. Warranty**

IN NO EVENT SHALL LICENSOR BE LIABLE TO YOU OR ANY OTHER PARTY OR ANY OTHER PERSON OR FOR ANY SPECIAL, CONSEQUENTIAL, INCIDENTAL OR INDIRECT DAMAGES, HOWEVER CAUSED, ARISING OUT OF OR IN CONNECTION WITH THE DOWNLOADING, VIEWING OR USE OF THE MATERIALS REGARDLESS OF THE FORM OF ACTION, WHETHER FOR BREACH OF CONTRACT, BREACH OF WARRANTY, TORT, NEGLIGENCE, INFRINGEMENT OR OTHERWISE (INCLUDING, WITHOUT LIMITATION, DAMAGES BASED ON LOSS OF PROFITS, DATA, FILES, USE, BUSINESS OPPORTUNITY OR CLAIMS OF THIRD PARTIES), AND
WHETHER OR NOT THE PARTY HAS BEEN ADVISED OF THE POSSIBILITY OF SUCH DAMAGES. THIS LIMITATION SHALL APPLY NOTWITHSTANDING ANY FAILURE OF ESSENTIAL PURPOSE OF ANY LIMITED REMEDY PROVIDED HEREIN.

**8. Limitations**

**8. 1.** ***BOOKS ONLY:*** Where **'reuse in a dissertation/thesis'** has been selected the following terms apply: Print rights of the final author's accepted manuscript (for clarity,

NOT the published version) for up to 100 copies, electronic rights for use only on a personal website or institutional repository as defined by the Sherpa guideline (www.sherpa.ac.uk/romeo/).

**8. 2.** For content reuse requests that qualify for permission under the STM Permissions Guidelines, which may be updated from time to time, the STM Permissions Guidelines supersede the terms and conditions contained in this licence.

**9. Termination and Cancellation**

**9. 1.** Licences will expire after the period shown in Clause 3 (above).

**9. 2.** Licensee reserves the right to terminate the Licence in the event that payment is not received in full or if there has been a breach of this agreement by you.

**Appendix 1 — Acknowledgements:**

**For Journal Content:**
Reprinted by permission from [**the Licensor**]: [**Journal Publisher** (e.g. Nature/Springer/Palgrave)] [**JOURNAL NAME**] [**REFERENCE CITATION** (Article name, Author(s) Name), [**COPYRIGHT**] (year of publication)

For **Advance Online Publication papers:**
Reprinted by permission from [**the Licensor**]: [**Journal Publisher** (e.g. Nature/Springer/Palgrave)] [**JOURNAL NAME**] [**REFERENCE CITATION** (Article name, Author(s) Name), [**COPYRIGHT**] (year of publication), advance online publication, day month year (doi: 10.1038/sj.[JOURNAL ACRONYM].)

**For Adaptations/Translations:**
Adapted/Translated by permission from [**the Licensor**]: [**Journal Publisher** (e.g. Nature/Springer/Palgrave)] [**JOURNAL NAME**] [**REFERENCE CITATION** (Article name, Author(s) Name), [**COPYRIGHT**] (year of publication)

**Note: For any republication from the British Journal of Cancer, the following credit line style applies:**

Reprinted/adapted/translated by permission from [**the Licensor**]: on behalf of Cancer Research UK: : [**Journal Publisher** (e.g. Nature/Springer/Palgrave)] [**JOURNAL NAME**] [**REFERENCE CITATION** (Article name, Author(s) Name), [**COPYRIGHT**] (year of publication)

For **Advance Online Publication** papers:
Reprinted by permission from The [**the Licensor**]: on behalf of Cancer Research UK: [**Journal Publisher** (e.g. Nature/Springer/Palgrave)] [**JOURNAL NAME**] [**REFERENCE CITATION** (Article name, Author(s) Name), [**COPYRIGHT**] (year of publication), advance online publication, day month year (doi: 10.1038/sj.[JOURNAL ACRONYM])

**For Book content:**
Reprinted/adapted by permission from [**the Licensor**]: [**Book Publisher** (e.g.

Palgrave Macmillan, Springer etc) [**Book Title**] by [**Book author**(s)]
[**COPYRIGHT**] (year of publication)

**Other Conditions**:

Version 1.3

**Questions? customercare@copyright.com or +1-855-239-3415 (toll free in the US) or +1-978-646-2777.**

AIP PUBLISHING LICENSE
TERMS AND CONDITIONS

Sep 03, 2021

---

This Agreement between Mr. Onurcan Kaya ("You") and AIP Publishing ("AIP Publishing") consists of your license details and the terms and conditions provided by AIP Publishing and Copyright Clearance Center.

| | |
|---|---|
| License Number | 5141560372746 |
| License date | Sep 03, 2021 |
| Licensed Content Publisher | AIP Publishing |
| Licensed Content Publication | Journal of Applied Physics |
| Licensed Content Title | Size dictated thermal conductivity of GaN |
| Licensed Content Author | Thomas E. Beechem, Anthony E. McDonald, Elliot J. Fuller, et al |
| Licensed Content Date | Sep 7, 2016 |
| Licensed Content Volumc | 120 |
| Licensed Content Issue | 9 |
| Type of Use | Thesis/Dissertation |
| Requestor type | Student |

| | |
|---|---|
| Format | Print and electronic |
| Portion | Figure/Table |
| Number of figures/tables | 1 |
| Will you be translating? | No |
| Title | Understanding the Ballistic-Diffusive Thermal Transport Trends in Crystalline Semiconductors with Molecular Dynamics |
| Institution name | Bogazici University |
| Expected presentation date | Sep 2021 |
| Portions | Figure 3.1 |
| Requestor Location | Mr. Onurcan Kaya<br>Bogazici University South Campus Enginee<br>Bebek/Besiktas<br><br>Istanbul, Turkey 34342<br>Turkey<br>Attn: Bogazici University |
| Total | 0.00 USD |

Terms and Conditions

AIP Publishing -- Terms and Conditions: Permissions Uses

AIP Publishing hereby grants to you the non-exclusive right and license to use and/or distribute the Material according to the use specified in your order, on a one-time basis, for the specified term, with a maximum distribution equal to the number that you have ordered. Any links or other content accompanying the Material are not the subject of this license.

1. You agree to include the following copyright and permission notice with the reproduction of the Material:"Reprinted from [FULL CITATION], with the permission of AIP Publishing." For an article, the credit line and permission notice must be

printed on the first page of the article or book chapter. For photographs, covers, or tables, the notice may appear with the Material, in a footnote, or in the reference list.

2. If you have licensed reuse of a figure, photograph, cover, or table, it is your responsibility to ensure that the material is original to AIP Publishing and does not contain the copyright of another entity, and that the copyright notice of the figure, photograph, cover, or table does not indicate that it was reprinted by AIP Publishing, with permission, from another source. Under no circumstances does AIP Publishing purport or intend to grant permission to reuse material to which it does not hold appropriate rights.
   You may not alter or modify the Material in any manner. You may translate the Material into another language only if you have licensed translation rights. You may not use the Material for promotional purposes.
3. The foregoing license shall not take effect unless and until AIP Publishing or its agent, Copyright Clearance Center, receives the Payment in accordance with Copyright Clearance Center Billing and Payment Terms and Conditions, which are incorporated herein by reference.
4. AIP Publishing or Copyright Clearance Center may, within two business days of granting this license, revoke the license for any reason whatsoever, with a full refund payable to you. Should you violate the terms of this license at any time, AIP Publishing, or Copyright Clearance Center may revoke the license with no refund to you. Notice of such revocation will be made using the contact information provided by you. Failure to receive such notice will not nullify the revocation.
5. AIP Publishing makes no representations or warranties with respect to the Material. You agree to indemnify and hold harmless AIP Publishing, and their officers, directors, employees or agents from and against any and all claims arising out of your use of the Material other than as specifically authorized herein.
6. The permission granted herein is personal to you and is not transferable or assignable without the prior written permission of AIP Publishing. This license may not be amended except in a writing signed by the party to be charged.
7. If purchase orders, acknowledgments or check endorsements are issued on any forms containing terms and conditions which are inconsistent with these provisions, such inconsistent terms and conditions shall be of no force and effect. This document, including the CCC Billing and Payment Terms and Conditions, shall be the entire agreement between the parties relating to the subject matter hereof.

This Agreement shall be governed by and construed in accordance with the laws of the State of New York. Both parties hereby submit to the jurisdiction of the courts of New York County for purposes of resolving any disputes that may arise hereunder.

V1.2

**Questions? customercare@copyright.com or +1-855-239-3415 (toll free in the US) or +1-978-646-2777.**